The TUDelft Global GRACE(-FO) Level-3 equivalent water height uncertainty product

Michal Cuadrat-Grzybowski[1], Pieter N. A. M. Visser[1], and João de Teixeira da Encarnação[1]

[1]Delft University of Technology, Faculty of Aerospace Engineering, Space Engineering Department, Kluyverweg 1, 2629 HS Delft, The Netherlands

Correspondence: Michal Cuadrat-Grzybowski (M.Cuadrat-Grzybowski-1@tudelft.nl)

Abstract. We present TUD-L3-EWH_UNC-GRACE, a globally gridded Level-3 GRACE(-FO) equivalent water height (EWH) data product providing an extensive characterisation of uncertainty for direct use in Earth system research. Unlike conventional approaches that either require propagation of full variance-covariance matrices or rely on empirical assumptions regarding temporal and spatial correlations, the dataset combines ensemble statistics from independently processed Level-2 solutions to quantify uncertainties associated with ocean tide models, parametrisation strategies, and Atmosphere and Ocean De-aliasing products. Post-processing uncertainties related to filtering effects and Glacial Isostatic Adjustment (GIA) model variability are quantified using a known-pair approach and an ensemble of 56 GIA models, respectively. Uncertainty fields are provided for multiple anisotropic filtering strategies (DDK2–DDK7), enabling assessment of filtering strength, leakage effects, and processing-choice impacts on total uncertainty. In addition to the standard Level-3 configuration, the ancillary TUD-L3-EWH_UNC_noSLR-GRACE product, in which low-degree coefficients ($\bar{C}_{2,0}$ and $\bar{C}_{3,0}$) are not replaced by Satellite Laser Ranging estimates, allows users to isolate uncertainties associated with low-degree coefficient treatment. TUD-L3-EWH_UNC is the first Level-3 EWH dataset to provide end-to-end gridded uncertainty fields, supporting applications in hydrology, glaciology, solid-Earth, and oceanographic studies. Ancillary tidal corrections and climatological fits are distributed separately through the TUD-L3-EWH_CLIM-GRACE product suite. The dataset is available at DOI: 10.4121/4fc748e8-01c7-4f06-87da-653937b078f7.

Keywords

GRACE, uncertainty, equivalent water height, space geodesy and gravimetry, Global, Level-3.

Preprint version accepted for publication on September 14 2026, in the Big Earth Data journal (Taylor & Francis).

https://doi.org/10.1080/20964471.2026.2750689 (preliminary and approximate publication in November/December 2026).

1 Introduction

The Gravity Recovery and Climate Experiment (GRACE) and its successor GRACE-FO (GFO) (Landerer et al., 2020; Tapley et al., 2004) provide continuous observations of Earth's time-variable gravity field, enabling monitoring of mass change and redistribution. The mission data are organised into several levels. Level-1(A/B) contains raw and calibrated satellite measurements, respectively, including inter-satellite range and range rate from the microwave system, accelerometer observations, GPS orbits, attitude data, and, for GRACE-FO, laser ranging measurements (Case et al., 2010). Level-2 comprises monthly spherical harmonic coefficients (SHCs) that represent the gravity field recovered by numerous processing centres. At this stage, the solutions reflect the outcome of the gravity inversion but do not yet include standard post-processing steps such as mean field removal, spatial filtering, geocentre restoration, replacement of low-degree coefficients, or mitigation of tidal aliasing. An alternative representation of GRACE and GRACE-FO gravity fields is provided by mass concentration (mascon) solutions, which estimate regional mass variations directly on a predefined grid. Several mascon products are available, including solutions from the Center for Space Research (CSR) (Save et al., 2016), the Jet Propulsion Laboratory (JPL) (Wiese et al., 2016), and the Goddard Space Flight Center (GSFC) (Loomis et al., 2019). Compared to spherical harmonic solutions, mascon products apply spatial constraints during the inversion and directly provide gridded mass change estimates.

Level-2B remains in the spherical harmonic coefficient domain and therefore does not itself correspond to gridded products. Instead, Level-2B provides processed and corrected SHC solutions that can subsequently be synthesised into gridded Equivalent Water Height (EWH) grids and converted into anomalies by removing the long-term mean. Standard GRACE(-FO) post-processing is typically applied at this stage (Dahle et al., 2025), including the addition of degree-1 geocentre motion (Swenson et al., 2008), replacement of $\bar{C}_{2,0}$ and $\bar{C}_{3,0}$ (GFO) (Loomis & Rachlin, 2023), glacial isostatic adjustment (GIA) correction, filtering, and mitigation of tidal aliasing effects (e.g., the 161-day S_2 tide). Synthesised or gridded SHC therefore provide consistent and ready-to-use EWH fields while remaining closely linked to the underlying SHC solutions, allowing users to apply their own spatial averaging strategies and uncertainty treatments compared with higher-level products. Level-3 represents application-specific mass anomaly data, for example, terrestrial or groundwater storage (TWS/GWS), ice-mass change, or ocean bottom pressure (OBP). These products build upon Level-2B-derived fields but require additional transformations, such as conversion from EWH to pressure units for ocean applications and, in some cases, re-addition of background model components such as GAA (non-tidal atmospheric component), GAB (oceanic component), or GAC (combined atmosphere-ocean component) (Dobslaw et al., 2018). Within this hierarchy, synthesised or gridded SHC serve as a practical intermediate step between SHC-based Level-2/2B solutions and fully analysis-ready Level-3 products, enabling researchers to tailor filtering and correction strategies for hydrology, glaciology, solid-Earth, or oceanographic applications.

Despite the extensive use of these datasets, uncertainty quantification remains a major challenge, particularly in assimilation frameworks that require independent observational error information (Blazquez et al., 2018; Retegui-Schiettekatte et al., 2025; Velicogna et al., 2014; Wu et al., 2022; Yang et al., 2025). Full covariance matrices are generally not distributed with GRACE(-FO) Level-2 products (except for GFZ and ITSG), are difficult to reconstruct independently (Zhang et al., 2024), and often are unclear regarding the numerous and diverse underlying assumptions. Furthermore, gridded uncertainty fields suitable for

end-user applications are largely unavailable, presenting an additional challenge for researchers to perform robust hydrological, glaciological, or solid-Earth analyses.

As a result, most practical uncertainty characterisations rely on approximate or empirically derived approaches (Boergens, 2021; Boergens et al., 2022). For instance, the Global Gravity-based Groundwater Product (G3P) project (Güntner et al., 2024) adopts empirical models based on monthly GRACE(-FO) fields. Comparisons with uncertainties derived from full covariance propagation show that empirical estimates often overestimate absolute error magnitudes, while their spatial correlations, when aggregated over major river basins, typically remain below 0.75 (Boergens et al., 2022). Other statistical methods require collapsing either the temporal or spatial dimensions, thus reducing the information content of the original solutions (J. Chen et al., 2021; Gao et al., 2023). For example, J. Chen et al. (2021) apply a three-cornered-hat (TCH) method to CSR, GFZ, and JPL SHC solutions, providing uncertainties resolved only in space, while Gao et al. (2023) extend this approach to mascon products using Bayesian fusion, which also yields spatially resolved uncertainties without capturing temporal variability. Although this yields a spatial representation of the error, the temporal component is effectively eliminated, and the reliance on three independent solutions introduces sensitivity to inter-centre differences and filtering strategies. To address this, You et al. (2025) combine multiple GRACE monthly solutions in the spatial domain using several weighting strategies. In particular, they introduce an "oceanic accuracy" weighting scheme derived from residuals over the open ocean, which reduces noise and demonstrates that accounting for spatially varying signal-to-noise characteristics improves GRACE estimates of mass changes, which they validated over the Caspian Sea.

A further key element of the GRACE(-FO) error budget is uncertainty associated with GIA, a process essential when interpreting long-term variability in EWH, geoid, or other gravity-derived quantities. The ICE6G-D model (Peltier et al., 2018) is widely used, but more than 50 GIA models exist (Bagge et al., 2023), each with spatial frequency-distinct signal characteristics. These differences can strongly influence geophysical trends, particularly in hydrology, and may even lead to contradictory interpretations of groundwater evolution (Caron et al., 2018; Eicker et al., 2024). Although GIA uncertainty is often considered in glaciological studies (Blazquez et al., 2018; Groh & Horwath, 2021; Velicogna et al., 2014), it is still frequently neglected in hydrological applications, despite its influence in high-latitude regions (e.g., North America) (Eicker et al., 2024).

Ensemble-based and regional analyses further demonstrate that methodological choices made by different processing centres govern substantial parts of the GRACE(-FO) error budget. Blazquez et al. (2018) created an ensemble of 1500 post-processed gravity fields, generated by combining five GRACE solutions from different centres with multiple geocentre treatments, filtering approaches, leakage corrections, and GIA models. This analysis showed that choices in geocentre treatment, GIA modelling, filtering, leakage correction, and data centre-specific conventions dominate uncertainties in global water- and sea-level trends. Regional analyses reinforce these findings: Velicogna et al. (2014) demonstrated that leakage, filtering, and background models substantially affect mass-balance estimates in Greenland and Antarctica, while Groh and Horwath (2021) showed similar impacts in Antarctica across multiple solutions. Complementary basin-scale and sea-level comparisons (Ablain et al., 2019; Boergens et al., 2022) further illustrate the consequences of differing processing conventions.

Another major source of uncertainty arises from the Atmosphere–Ocean De-Aliasing (AOD1B) and Ocean tidal (OT) background models. The AOD1B RL06 product is routinely removed prior to gravity field estimation (Dobslaw et al., 2017).

Recent work by Shihora et al. (2024) provides a quantification of residual AOD1B RL07 errors via the AOe07 time series, constructed from ensemble simulations using different models of atmospheric and oceanic mass variability. They further provide a full spatio-temporal covariance matrix for these errors up to degree/order 40. Including AOD model uncertainties in gravity inversion has been shown to significantly reduce aliasing artefacts: Kvas and Mayer-Gürr (2019) demonstrated RMS noise reductions of $\sim 25\%$ over the oceans by including AOD errors, while Zhou et al. (2023) reported 26–65% reductions in simulations. These results underscore the importance of including AOD1B uncertainty in data assimilation and other geophysical applications. Part of the uncertainty in GRACE and GRACE-FO gravity field solutions is also implicitly represented by differences in the background models adopted by the individual processing centres. In particular, various ocean tide models have been used, including GOT4.8 (Ray, 2013), FES2014 (Carrère et al., 2016), FES2014b (Lyard et al., 2021), and EOT11a (Savcenko & Bosch, 2012), while upcoming newer solutions are expected to employ more recent models such as GOT5.6 (Ray, 2025), FES2022 (Carrere et al., 2022), and EOT20 (Hart-Davis et al., 2021).

In this study, we present TUD-L3-EWH_UNC, a transparent Level-3 mass anomaly product derived from monthly GRACE and GRACE-FO SHC solutions. The product preserves the geophysical content of the Level-2 data while applying only the minimal required processing steps, namely spherical harmonic truncation, noise filtering, and mean field removal. Here, "processing" refers to the sequence of modelling and correction steps applied before and after the Level-2 stage. Pre-processing includes the modelling choices made during gravity field recovery from Level-1B observations, such as the use of the AOD1B model and the parametrisation of gravitational and non-gravitational forces. Post-processing refers to the transformations commonly applied to Level-2 SHC solutions in order to derive gridded mass anomalies, including filtering, replacement of low-degree coefficients using Satellite Laser Ranging (SLR), inclusion of degree-1 (geocenter) variations, and corrections for GIA or tidal aliasing. Unlike standard Level-2B or Level-3 products, TUD-L3-EWH_UNC provides both GIA-corrected and uncorrected fields, with GIA, geocentre motion, and tidal aliasing corrections distributed as separate components, allowing users to apply them selectively. A central innovation is a structured, layered uncertainty product in which contributions from individual pre- and post-processing stages are provided alongside the combined Level-3 grids. This directly addresses several limitations identified in the literature: gridded, spatio-temporally resolved uncertainty fields are provided rather than collapsed spatial or temporal estimates; AOD1B uncertainty is included as a traceable, separable layer based on the AOe07 characterisation (Shihora et al., 2024); GIA uncertainty is explicitly quantified and provided separately, supporting applications beyond glaciology; and the layered structure exposes individual processing choices transparently, rather than absorbing them into a single product.

This paper is organised as follows. Section 2 presents the data used in this study. Section 3 describes the methodology, including the ensemble uncertainty estimation and post-processing treatment. Section 4 provides a description of the data product, while Section 5 presents the technical validation. Lastly, Section 6 presents the main results, including verification and selected geophysical applications.

2 Data sources

2.1 GRACE(-FO) Level-2 solutions

To construct the GRACE(-FO) uncertainty from Level-2 SHC products (S. Bettadpur, 2018a), we use monthly gravity field solutions from several processing centres. The combined solution is obtained as a weighted ensemble mean of all individual solutions after conversion to EWH (see Section 3.3.1). These solutions are summarised in Table 1 and were obtained from the ICGEM repository (Ince et al., 2019). The maximum spherical harmonic degree listed in Table 1 corresponds to the degree used in this study. Although several processing centres (e.g., CSR, GFZ, JPL, ITSG, Tongji, and HUST) provide solutions to higher degrees (e.g., degree 96 or 120, depending on the centre), all solutions are consistently truncated to degree 60 for the generation of the uncertainty product (see Section 3.1). The GRACE data span April 2002 to June 2017. GRACE-FO covers the period from 2018 to the present. For consistency with the temporal coverage of the uncertainty product developed in this study, the GRACE-FO record is truncated to December 2020.

To quantify the variability among monthly solutions, each field is reduced by subtracting the monthly COST-G RL02.1 solution (Jäggi et al., 2022), which serves as the ensemble reference. The resulting spread across solutions is used as a measure of the inter-centre or ensemble uncertainty, as described in Section 3.3.1.

Table 1. Monthly GRACE and GRACE-FO Level-2 spherical harmonic solutions used in this study. All solutions were downloaded from the ICGEM repository (https://icgem.gfz-potsdam.de). The COST-G RL02.1 solution is used as the ensemble reference. The APM-SYSU solution is included from ICGEM; however, no corresponding reference publication is currently available.

Institute	Model name	Version	Max degree	Reference
ITSG	ITSG-Grace2018(_op)	–	60	Mayer-Gürr et al. (2018)
CSR	CSR	RL06 (06.3)	60	S. Bettadpur (2018b)
JPL	JPL	RL06 (06.3)	60	Yuan (2018)
GFZ	GFZ	RL06 (06.3)	60	Dahle et al. (2019)
HUST	HUST-Grace2024	–	60	Zhou et al. (2024)
LUH	LUH-Grace(-FO)-2020	–	96	Koch et al. (2021)
CNES	CNES CHOL	RL05	90	Lemoine & Bourgogne (2020)
AIUB	AIUB G3P	–	90	Darbeheshti et al. (2023)
AIUB	AIUB-GRACE-FO	RL02_op	90	Lasser et al. (2023)
APM-SYSU	APM-SYSU	–	90	N.A.
Tongji	Tongji-Grace2022	–	60	Q. Chen et al. (2023)
AIUB	COST-G	RL02.1	90	Jäggi et al. (2022)

2.2 Additional input data

Additional datasets include the Atmosphere and Ocean De-aliasing (AOD1B) error residuals product (AOe07), available for the period 2002–2020 (Shihora et al., 2024), and a set of 56 global GIA models compiled by Bagge et al. (2023). These datasets are incorporated to quantify contributions from background model uncertainties and post-processing effects.

Low-degree spherical harmonic coefficients are treated using external SLR and geocentre solutions. Specifically, the "oblateness" and d/o (3,0) coefficients, $\bar{C}_{2,0}$ and $\bar{C}_{3,0}$, are replaced using the official GRACE(-FO) Technical Note (TN-14.v3) time series derived from SLR observations (Loomis & Rachlin, 2023). Degree-1 (geocentre) coefficients ($\bar{C}_{1,0}$, $\bar{C}_{1,1}$, $\bar{S}_{1,1}$) are taken from the TN-13 CSR RL06(.3) geocentre solution, which is based on the methodology described in Sun et al. (2016).

3 Methodology

3.1 From Level-2 to gridded Level-3 products

All Level-2 SH solutions used in this study (see Section 2.1) are considered up to degree and order (d/o) 60. Following Jean et al. (2018), all solutions are additionally harmonised in terms of the scaling according to IERS 2010 Conventions (Petit & Luzum, 2010), including the product of the gravitational constant and mean Earth mass (GM), the Earth mean radius (R), and the tide system (converted from zero-tide to tide-free). In addition, the mean pole tide convention of the APM-SYSU and Tongji-Grace2022 solutions is harmonised with the linear mean-pole model adopted in the newest version of the IERS 2010 Conventions (February 2018 update). Further details on this harmonisation process can be found in Appendix A. For solutions originally provided at higher resolution (e.g., d/o 90 or 96), hard truncation is applied above d/o 60, ensuring that higher-degree terms do not contribute to the analysis.

The choice of truncating to degree 60 reflects the fact that GRACE(-FO) solutions become increasingly noise-dominated at higher degrees (typically above 30–50), even before truncation. In addition, the subsequent application of DDK filtering (see below) further suppresses the contribution of higher-degree coefficients, limiting their effective impact on the analysed signal. A systematic sensitivity analysis with respect to the choice of maximum degree is considered beyond the scope of this study.

To remove the long-term static component and isolate the time-variable signal, we subtract a static gravity field from each monthly solution. We adopt CSR's GGM05C (Ries et al., 2016), truncated at d/o 60, with a reference epoch of January 2008. A different choice would only shift the reference epoch, leaving the relative time-variable anomalies unchanged. Furthermore, the choice of static field does not affect the uncertainty characterisation, since all contemporary static gravity models are of equivalent quality up to d/o 60 (Ghobadi-Far et al., 2022). Subsequently, DDK filtering (Kusche et al., 2009) of varying strengths (DDK2–DDK7) is applied to mitigate noise and leakage effects.

Before removing the long-term static component and DDK-filtering, certain low-degree coefficients require special treatment due to their importance for geophysical interpretation:

- The $\bar{C}_{2,0}$ (for both GRACE and GRACE-FO) and $\bar{C}_{3,0}$ (for GRACE from March 2012 onward, and for all of GRACE-FO) coefficients are replaced by SLR-based estimates from TN-14.v3 (Loomis & Rachlin, 2023; Loomis et al., 2020).

This is done because these low-degree zonal terms are poorly constrained by GRACE/GRACE-FO observations alone and have a strong impact on large-scale mass redistribution signals, including polar ice sheets, ocean mass changes, and high-latitude hydrology.

– The geocenter motion (degree-1) component is provided using TN-13 CSR's RL06(.3) (Sun et al., 2016), and is provided as a separate variable which can be optionally added by the user to the gridded solutions. This term is essential for capturing mass variations relative to the Earth's centre of mass, which are most critical for oceanography and hydrological, glaciological, and solid Earth studies, focused on total error budgets.

Finally, the truncated and filtered SH coefficients differences are then synthesised to the spatial domain to obtain EWH, δh, on a regular grid. For a degree-truncated solution at $n_{\max}$, the EWH at latitude ϕ and longitude λ is computed as (Ditmar, 2018):

$$\delta h(r,\lambda,\phi) = \frac{M_E}{4\pi R^2 \rho_w} \sum_{n=1}^{n_{\max}} \sum_{m=0}^{n} \left(\frac{R}{r}\right)^{n+2} \frac{(2n+1)}{(1+k_n)} \left(\Delta\bar{C}_{n,m}\cos m\lambda + \Delta\bar{S}_{n,m}\sin m\lambda\right) \bar{P}_{n,m}(\sin\phi), \tag{1}$$

where M_E is the Earth's mass, R is the mean Earth radius, r is the radial distance to the evaluation point on the reference ellipsoid, ρ_w is the density of water, k_n are the load Love numbers, $\Delta\bar{C}_{n,m}$ and $\Delta\bar{S}_{n,m}$ are the fully-normalised SH coefficient anomalies (w.r.t a static or long-term mean), and $\bar{P}_{n,m}$ are fully-normalised associated Legendre functions. This formulation accounts explicitly for the ellipsoidal shape of the Earth and is consistent with modern EWH computations from SH coefficients.

3.2 Treatment of persistent aliasing tides for Level-3

In addition to the standard 161-day S_2 tidal aliasing correction typically applied in Level-2 products (Dahle et al., 2025), we provide two additional persistent aliased tidal constituents, S_1 and P_1, as well as the non-modelled radiational tide R_3 (Koch et al., 2024) (see Table 2). The inclusion of S_1 and P_1 is supported by previous GRACE studies showing that these aliases can remain observable in monthly gravity solutions (Tourian, 2013; Tourian et al., 2022, 2018), including in the latest RL06 solutions, where S_2 and P_1 aliasing were found to be particularly pronounced at high latitudes (Li et al., 2022; Seo et al., 2008). The relevance of tidal aliasing for polar applications is further demonstrated by Moore and King (2008), who showed its impact on Antarctic mass-balance estimates, while Li et al. (2022) found strong S_2 aliasing over West Antarctica and P_1 aliasing over South Greenland. Consistent with this evidence, the SAGEA toolbox provides S_1, S_2, and P_1 as optional tidal de-aliasing corrections (S. Liu et al., 2025). To account for the different orbital-plane orientations between the GRACE and GRACE-FO missions, a phase shift of 100° is applied when estimating these nuisance signals, following the S_2-specific treatment of Dahle et al. (2025) and Landerer et al. (2020). Ideally, the phase shift should be estimated independently for each tidal constituent; however, such an empirical estimation constitutes a non-linear problem and is beyond the scope of this study. We therefore apply the 100° phase shift to all considered signals at tidal aliasing frequencies as a common approximation. These corrections

target low-frequency aliasing signals arising from residual modelling errors of the corresponding high-frequency tides, rather than the original tidal constituents themselves, but the fitted signals may also contain contributions from other sources.

Regarding the aliased $\mathrm{K_1}$ signal, it has a period of approximately 7 years and an amplitude of ∼3–5 cm. In this study, however, we do not estimate $\mathrm{K_1}$ because its long alias period leads to strong collinearity with polynomial trend terms over the ∼19-year record, making its separation from secular and interannual variability unstable. The aliased $\mathrm{K_2}$ constituent is likewise not estimated, but for a different reason: its aliasing period strongly overlaps with genuine low-frequency geophysical variability, such that fitting and removing it risks absorbing significant hydrological and other climate-related mass variations into the tidal correction (Kvas et al., 2019). The $\mathrm{R_3}$ component has substantially less support as an ocean-tide correction, but is retained because Koch et al. (2024) identified it as a non-modelled tide capable of producing a significant aliased signal.

The applicability of these corrections is spatially and application-dependent. Han et al. (2010) showed that the GRACE sampling of diurnal tides leads to substantial cancellation between ascending and descending tracks, particularly away from polar regions. We therefore provide $\mathrm{S_1}$, $\mathrm{P_1}$, and $\mathrm{R_3}$ as separately available components rather than universally applicable corrections, allowing users to assess their relevance for their specific region and application. In particular, applications in polar and high-latitude regions may benefit from considering these components, whereas lower-latitude and equatorial applications should apply them with greater caution. The resulting fitted signals should not be interpreted as pure ocean-tide errors, but may contain both tidal aliasing errors and contributions from other sources, including genuine geophysical variability.

The tidal signals are removed from the EWH grids by co-estimating their amplitudes simultaneously with a climatological model that includes a bias (A), linear trend (B), quadratic trend (C), annual (D and E), and semi-annual components (F and G):

$$\delta h^{\mathrm{clim}}(t) = A + Bt' + \frac{1}{2}Ct'^2 + D\sin(\omega_{\mathrm{clim}}t') + E\cos(\omega_{\mathrm{clim}}t') + F\sin(2\omega_{\mathrm{clim}}t') + G\cos(2\omega_{\mathrm{clim}}t') + \sum_{k=1}^{N_k} S_k\sin(\omega_k t') + C_k\cos(\omega_k t'). \tag{2}$$

where t is in years, $t' = t - t_{\mathrm{ref}}$ with $t_{\mathrm{ref}} = 2008.0$, $\omega_{\mathrm{clim}} = 2\pi$ rad yr^{-1}, and S_k and C_k are the coefficients of the k^{th} tide with aliasing frequency ω_k (see Table 2). The resulting sine and cosine coefficients, S_k and C_k respectively, for each tide are stored separately (with the climatological coefficients), allowing users to inspect or reintegrate the tidal contribution if needed. For completeness, the amplitudes of these persistent tidal constituents are briefly analysed in Appendix C4.

Table 2. Persistent tides (tidal periods and aliasing periods) to be removed from EWH. Values of the tidal periods are directly retrieved from Koch et al. (2024), with GRACE and GRACE-FO nodal rate $\dot{\Omega} = -0.134\ ^{\circ}\mathrm{day}^{-1}$ (see Appendix C), and Earth's sidereal rotation $\omega = 360.9856\ ^{\circ}\mathrm{day}^{-1}$.

Tide	Period [day]	Aliasing Period [day]
S_2	$0.500000 \pm 7.968 \times 10^{-6}$	160.8
P_1	$1.002751 \pm 2.320 \times 10^{-5}$	170.9
S_1	$1.000021 \pm 3.625 \times 10^{-8}$	319.5
R_3	$1.003542 \pm 3.838 \times 10^{-5}$	150.6

3.3 Ensemble-based and processing-related uncertainties

3.3.1 Ensemble-based uncertainty from multiple GRACE(-FO) centres

Ensemble statistics across multiple gridded Level-2 solutions are used to estimate pre-processing uncertainties, where the differences mostly lie in the use of parametrisation strategies and ocean tide background models (see Table 3).

Here, we use the monthly COST-G RL02.1 product (Jäggi et al., 2022) as the reference benchmark, as it represents a combined solution derived from multiple processing centres and is therefore less susceptible to centre-specific noise than any individual solution. We estimate the inter-solution uncertainty as the unbiased weighted ensemble variance of the solutions for each month (l-level DDK filtered),

$$\sigma^2_{\delta h_l,\mathrm{sols}} = \frac{1}{1-\sum_{i=1}^{N} \bar{w}^2_{l,i}} \sum_{i=1}^{N} \bar{w}_{l,i} \left(\delta h_{l,i} - \overline{\delta h_l}\right)^2, \tag{3}$$

where $\delta h_{l,i}$ denotes the monthly equivalent water height filtered value (with DDKl) for the i^{th} solution, $\overline{\delta h_l}$ is the weighted ensemble mean of the monthly solutions, N is the number of data centres (see Section 2.1), and lastly $\bar{w}_{l,i}$ are the normalised weights computed using the square inverse of the monthly RMS over the oceans ($RMS_{\mathrm{oc},i}$) of the residuals with respect to the full COST-G signal (i.e., without prior removal of the climatology):

$$\bar{w}_{l,i} = \frac{1/RMS^2_{\mathrm{oc},i}}{\sum_i^N 1/RMS^2_{\mathrm{oc},i}}. \tag{4}$$

The use of the (weighted) ensemble standard deviation as an uncertainty estimator is supported by the statistical properties of the EWH residual distributions. As shown in Appendix B, residuals of all solutions with respect to the ensemble mean exhibit near-zero medians (of order 10^{-2} cm) and comparable distribution widths, indicating the absence of systematic offsets between data centres. It is important to note that $RMS_{\mathrm{oc},i}$ is evaluated over oceanic regions that are expected to contain minimal geophysical signal. To ensure this, a 500-km buffer is applied to exclude land and coastal influences, and the Argentine Basin is additionally masked to suppress residual variability associated with the oceanic gyre.

Not all solutions presented in Section 2.1 exhibit comparable noise characteristics, and a selection is therefore required to avoid contaminating both the combined ensemble mean and its associated uncertainty with solutions that display persistently

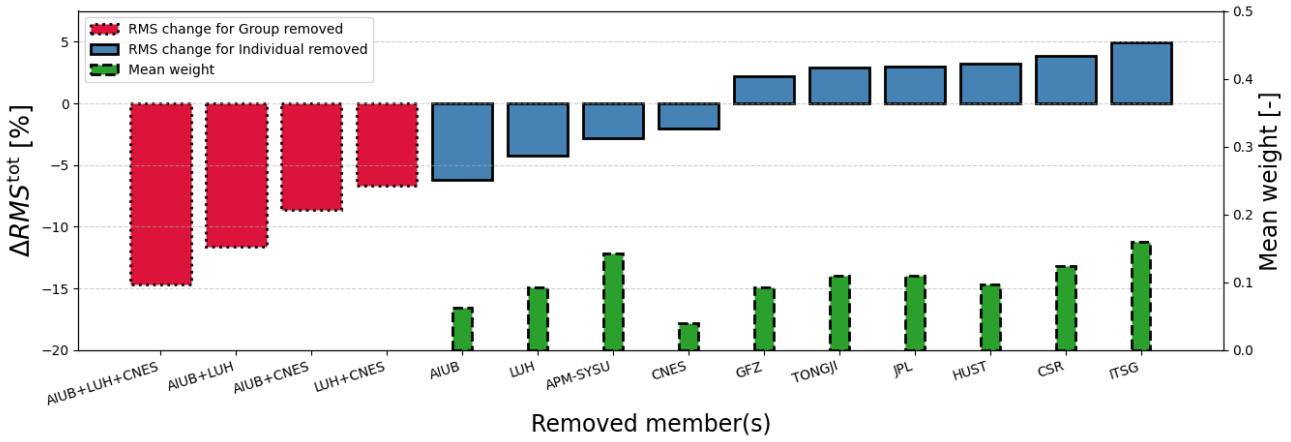


Figure 1. Relative difference in the total (spatio-temporal) root-mean-square, $\Delta RMS^{\mathrm{tot}}$, of the standard deviation for all Level-2 GRACE/GRACE-FO solutions (filtered using DDK4), computed when solutions are excluded relative to the case including all solutions. The COST-G RL02.1 solution is used as the benchmark to remove the monthly geophysical signal. The corresponding mean weights, calculated as the normalised inverse of the open ocean RMS, are also shown.

elevated noise levels or outlier behaviour. To this end, we adopt as a selection metric the temporal and spatial (i.e. total) RMS of $\sigma_{\delta h_4,\mathrm{sols}}$ (Eq. 3), denoted as $\Delta RMS^{\mathrm{tot}}$, computed using a DDK4 filter. This filter level represents a compromise between limiting signal attenuation and retaining sufficient sensitivity to noise (Qian et al., 2022), thereby allowing the metric to predominantly reflect solution noise rather than filtering artefacts. Furthermore, to avoid issues related to permanent tide system conventions and associated constant offsets (see Appendix A), we replace $\bar{C}_{2,0}$ using the SLR-based estimate before computing ensemble statistics, ensuring that it does not introduce a systematic bias into the weighting scheme. Figure 1 shows the relative change in the average RMS for scenarios in which a single or multiple solutions are excluded, compared to the nominal case where all solutions are retained. A negative relative $\Delta RMS^{\mathrm{tot}}$ indicates an improvement upon removal of the corresponding solution(s), whereas a positive value signifies a deterioration. The time-averaged weights for each solution are also shown. Furthermore, Figure 2 shows the time and spatial ΔRMS for specific solutions, being APM-SYSU (Figure 2a), the AIUB, LUH and CNES combination (Figure 2b), ITSG (Figure 2c) and CSR (Figure 2d). Note that APM-SYSU only provides monthly solutions for the GRACE mission.

The most pronounced degradation is observed when removing the ITSG solution, which results in the largest positive change in total RMS, with $\Delta RMS^{\mathrm{tot}}$ raising to $+4.99\%$. This increase indicates a clear deterioration of the ensemble mean noise and highlights the contribution of ITSG within the combined product. This behaviour is corroborated by the spatial patterns shown in Figure 2c, where the relative RMS difference is predominantly positive, ranging from approximately $+2.5\%$ to $+12.5\%$ over most regions. Only during the final phase of the GRACE mission (from 11/2016 to 06/2017) do isolated negative values of about -1.5% to -3.0% emerge. The overall dominance of positive spatial anomalies confirms that the removal of ITSG leads to a widespread increase in noise rather than isolated regional effects.

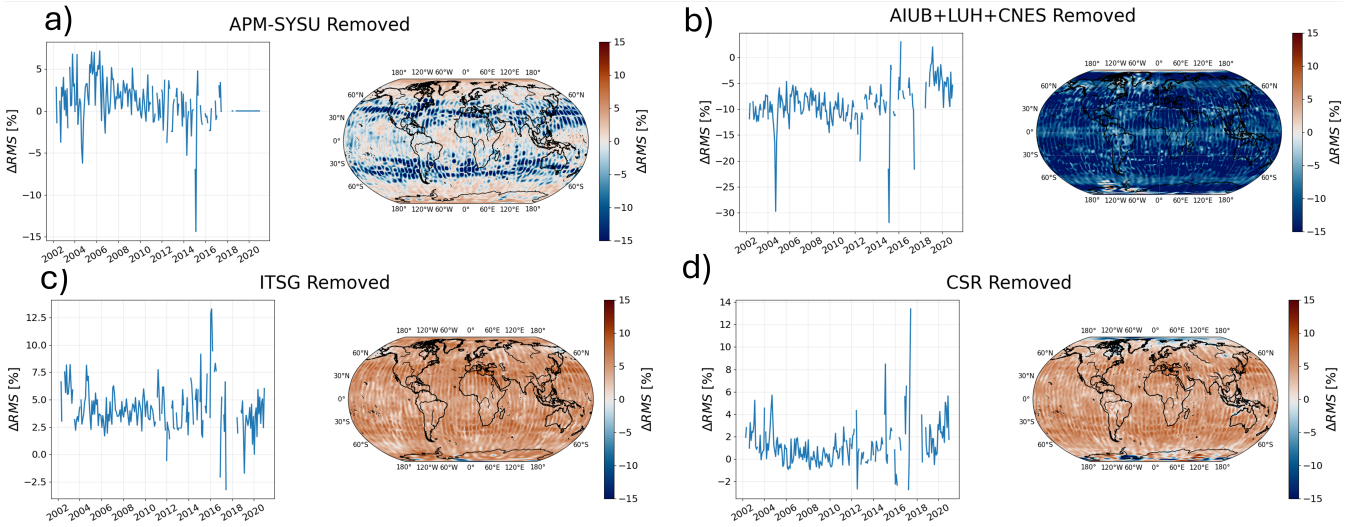


Figure 2. Relative difference in the time-dependent (left) and spatially distributed (right) RMS of the standard deviation for specific gridded Level-2 GRACE/GRACE-FO solutions (filtered using DDK4), computed when one or more solutions are excluded relative to the case including all solutions. These removed solutions are: (a) APM-SYSU, (b) AIUB+LUH+CNES, (c) ITSG, and (d) CSR. The COST-G RL02.1 solution is used as the benchmark to remove the monthly geophysical signal.

A qualitatively similar, though more nuanced, behaviour is observed for CSR, as shown in Figure 2d. In this case, the temporal evolution exhibits predominantly positive $\Delta RMS^{\mathrm{tot}}$ during non-nominal periods, which include near-repeat orbital cycles associated with orbit resonance effects (see peaks on 09/2004 and 02/2015) as well as mission intervals affected by instrument anomalies (e.g., the accelerometer shutdown at the end of 2016 and the subsequent gradual satellite altitude loss). During periods without such anomalies, CSR provides more minor improvements of $0.5 - 2.5\%$, with occasional negative excursions. This indicates that CSR performs very well in terms of noise handling during repeat patterns, data-limited, and other non-nominal intervals (with improvements ranging from 2.5% to 14%), while contributing more moderately during nominal conditions. The spatial distribution in Figure 2d further supports this interpretation, revealing distinct regional structures, most prominently in the Weddell Sea (approx. -12%) and in the vicinity of Greenland and Iceland. These coherent spatial patterns are characteristic of ocean tide model deficiencies and point to the ocean tide background model employed by CSR as the dominant source of its residual inconsistency. Consequently, the limitations associated with CSR are primarily linked to ocean tide modelling, while its overall performance during non-nominal mission phases remains excellent.

A particularly interesting case is the APM-SYSU solution. Despite having the second largest ensemble weight of approximately 0.142, whereas ITSG and CSR have mean weights of 0.160 and 0.123, its removal results in a negative $\Delta RMS^{\mathrm{tot}}$ of about -2.90%. This apparent contradiction is attributed to the temporal behaviour of APM-SYSU (see Figure 2a), which exhibits very low noise levels during nominal mission phases but significantly elevated noise during orbit repeat periods (see -6.5% and -15% on the 09/2004, and 02/2015) and months with reduced observational coverage (in 2003). A similar, albeit

more pronounced, behaviour is observed for the LUH solution (not shown). Based on these considerations, we retain the APM-SYSU solution in the final ensemble, as its overall contribution remains beneficial ($+2.5\%$ to even $+7\%$ in $\Delta RMS^{\mathrm{tot}}$) during nominal conditions despite episodic degradation. Conversely, the AIUB, CNES, and LUH solutions are excluded from the combined product, as their removal leads to a substantial and robust reduction in ensemble noise.

In contrast, the removal of the AIUB solution yields the largest negative $\Delta RMS^{\mathrm{tot}}$ (approximately -6.12%), since it leads to the largest increase in ensemble noise over the oceans. Similarly, the LUH and CNES solutions also exhibit negative $\Delta RMS^{\mathrm{tot}}$ values when removed individually, indicating a net improvement in ensemble consistency. Motivated by these results, all possible combinations of two and all of these solutions were evaluated. The simultaneous removal of AIUB, CNES, and LUH leads to a pronounced reduction in $\Delta RMS^{\mathrm{tot}}$ of approximately -14.4%, representing the largest overall improvement among all tested combinations. This behaviour is clearly reflected in the temporal evolution shown in Figure 2b, where the relative RMS difference remains consistently negative throughout the mission. In particular, pronounced minima of approximately -30%, -20%, and -32% are observed during the orbit near-repeat and resonance periods around 09/2004, 06/2012, and 02/2015, respectively, with a similarly strong reduction of about -21% during the final month of the GRACE mission (06/2017). The spatial component exhibits a comparable behaviour, with predominantly negative values across the globe. On average, the spatial reduction amounts to approximately -15%, while locally enhanced reductions of up to -20% are observed during the same orbit repeat periods. Further combinations involving AIUB paired individually with CNES or LUH yield larger open ocean noise magnitude compared to the "LUH+CNES" case. These findings are consistent with the derived ensemble weights. Both AIUB and CNES exhibit relatively small weights below 0.065, reflecting their comparatively high noise levels, whereas LUH attains a larger weight of approximately 0.093, comparable in magnitude to JPL and HUST. Notably, the latter two solutions display positive $\Delta RMS^{\mathrm{tot}}$ values when removed, further supporting their retention in the ensemble.

3.3.2 Background model pre-processing uncertainties

For the atmosphere–ocean background model contribution, we restrict our analysis to uncertainties arising from the AOD1B product. We do not explicitly model uncertainties from the ocean tide background model; instead, we assume that these are implicitly represented in the ensemble uncertainty (see Section 3.3.1) of the monthly GRACE/GRACE-FO solutions, as different processing centres rely on different ocean tide models (Table 3). Please note that at the moment of writing, we are unaware of any public documentation about the APM-SYSU GRACE solutions.

For the AOD1B component, we derive uncertainty fields from the AOe07 residual spherical harmonic coefficients of Shihora et al. (2024). These 6-hourly fields are converted into equivalent water height, and the error estimate is the monthly temporal root-mean-square as a spatially resolved (i.e. gridded) uncertainty estimate. The resulting EWH uncertainty fields are then propagated from Level-2 to Level-3 by applying the same filtering operators (DDK2–DDK7) used for the gravity solutions.

The choice of AOe07 is motivated by the limited availability and applicability of earlier AOD1B error product (AOerr). The AOerr dataset is primarily associated with AOD1B RL05 and is not representative of the substantially improved AOD1B RL06 model used by most GRACE/GRACE-FO processing centres (Dobslaw et al., 2017). In addition, AOerr is only available up

Table 3. Ocean tide models used in GRACE/GRACE-FO Level-2 processing across the selected analysis centres (see Section2.1). d/o refers to degree/order. (*) Additional co-estimation of residual ocean tide components (up to d/o 50) performed by TU Graz.

Analysis Centre	Ocean Tide Model	Max d/o	Reference
GFZ	FES2014	100	Carrère et al. (2016)
CSR	GOT4.8	180	Ray (2013)
JPL	FES2014b	180	Lyard et al. (2021)
TU Graz	FES2014b (*)	180	Lyard et al. (2021)
Tongji	EOT11a	100	Savcenko & Bosch (2012)
HUST	EOT11a	120	Savcenko & Bosch (2012)
APM-SYSU	Unknown	Unknown	N.A.

to 2006 (Dobslaw et al., 2016), which precludes its use for the full temporal span of the GRACE and GRACE-FO record considered in this study. Although AOe07 is formally more closely related to RL07 developments, it is currently the only globally available residual-based product with sufficient temporal coverage (2002–2020) and consistency to serve as a practical proxy for AOD1B uncertainty over the full mission period (with a likely tendency to underestimate the AOD1B RL06 uncertainty).

Lastly, although full Level-1B (L1B) to L2 error propagation would, in principle, require applying the AOD1B residuals through the satellite equations of motion and the L1B normal equations of each processing centre, this is not feasible within our framework. The normal matrices available for some centres (e.g., GFZ and ITSG) describe the L2 covariance of estimated parameters but do not capture the correlated impact of orbit-level AOD1B residuals on the observations. A rigorous propagation would require the full design matrix linking L1B observables to the estimated gravity field, which is unavailable for most centres (e.g., LUH, COST-G, HUST, Tongji, and APM-SYSU). Since our analysis is performed at the gridded Level-3 stage (in EWH), a consistent propagation across all centres is not possible. We therefore follow the pragmatic approach to assume that additional amplification of AOD1B uncertainties during L1B to L2 processing is small compared with the dominant uncertainty sources represented in AOe07.

3.4 Post-processing uncertainties

Post-processing uncertainty in the GRACE(-FO) mass change estimates is dominated by three contributions: (i) propagated formal errors including the inserted degree-1 geocenter and the replacement of low-degree coefficients $\bar{C}_{2,0}$ and $\bar{C}_{3,0}$, (ii) uncertainty in the correction for GIA, and (iii) uncertainty associated with the spatial leakage correction. These components are treated as independent, as they originate from distinct physical processes and separate data sources.

3.4.1 Propagated formal errors of low-degree replacements

The formal errors associated with the SLR-based low-degree coefficient solutions are propagated into equivalent water height following Boergens et al. (2022). This is performed through linear uncertainty propagation of Eq. 1. Denoting the formal

uncertainties of the fully normalized coefficients as $\sigma_{\bar{C}_{nm}}$ and $\sigma_{\bar{S}_{nm}}$, and assuming linear error propagation without cross-covariances, the variance contribution of each harmonic term is given by

$$\sigma^2_{h_{n,m}} = \left(\frac{M_E}{4\pi R^2 \rho_w}\right)^2 \left(\frac{R}{r}\right)^{2(n+2)} \left(\frac{2n+1}{1+k_n}\right)^2 \bar{P}^2_{n,m}(\sin\phi) \left[\sigma^2_{\bar{C}_{n,m}} \cos^2(m\lambda) + \sigma^2_{\bar{S}_{n,m}} \sin^2(m\lambda)\right]. \quad (5)$$

The formal error propagation includes (i) the formal errors of the coefficients $\bar{C}_{2,0}$ and $\bar{C}_{3,0}$ provided by the GRACE(-FO) Technical Note TN-14.v3 SLR time series (Loomis & Rachlin, 2023), and (ii) the formal errors of the degree-1 geocentre coefficients $(\bar{C}_{1,0}, \bar{C}_{1,1}, \bar{S}_{1,1})$ derived from the CSR RL06.3 geocentre solution following Technical Note TN-13 (Sun et al., 2016; Swenson et al., 2008). For the geocentre contribution (degree-1), the total propagated formal error EWH grid is obtained by summing the variance contributions (Eq. 5) over all contributing orders, i.e. $m = 0, 1$.

While an ensemble-based treatment of low-degree coefficients could in principle provide an alternative uncertainty estimate, this is not pursued here. For degree-1, coefficients could be estimated for the other gravity-field solutions following Sun et al. (2016); however, this would require additional processing beyond the scope of this study, whose objective is to provide uncertainty estimates for the available gravity-field products. Moreover, only three consistently processed degree-1 solutions from CSR, GFZ, and JPL are available, which provides a limited population for a statistically robust ensemble-based uncertainty estimate. Together with the limitations of SLR-based approaches for resolving the long-term trend of degree-1 coefficients discussed by Nie et al. (2025), and the relatively small contribution of degree-1 uncertainty to the overall uncertainty budget (Section 6.2), this motivates our choice to retain the propagated formal errors of the CSR degree-1 solution. Lastly, regarding $\bar{C}_{2,0}$ and $\bar{C}_{3,0}$, the number of established SLR-based replacement solutions is similarly limited. For $\bar{C}_{2,0}$, the main available solutions comprise the CSR TN-11E solution (Cheng & Ries, 2023), the TN-14.v3 solution, and the GFZ $\bar{C}_{2,0}$-only solution (König et al., 2019). The more recent IGG-UPWr solution provides an additional alternative (Gałdyn & Sośnica, 2024). However, it is not yet as widely used by the GRACE community as the established technical-note solutions. For $\bar{C}_{3,0}$, only the two technical-note solutions and the IGG solution are currently available. A known $\bar{C}_{2,0}-$trend discrepancy between TN-11E and TN-14.v3 is acknowledged (Cheng & Ries, 2023; Mei et al., 2025). Thus, excluding the IGG solution, the available solutions comprise approximately three $\bar{C}_{2,0}$ and two $\bar{C}_{3,0}$ solutions, respectively, which we consider insufficiently robust for deriving an uncertainty from ensemble statistics. We therefore use the formal errors associated with the adopted technical-note corrections to characterise the uncertainty of the applied SLR replacements, with TN-14.v3 providing a well-established basis given its widespread use and adoption in the GravIS and, consequently, Copernicus TWS products (Copernicus Climate Change Service, 2026; Dahle et al., 2025).

3.4.2 GIA trend uncertainty propagation

Uncertainty related to GIA corrections is treated separately. GIA trend uncertainty is quantified using ensemble statistics from 56 global GIA models compiled by Bagge et al. (2023), following the approach of Eicker et al. (2024). The ensemble mean and standard deviation represent the current spread arising from uncertainties in Earth rheology and ice-history reconstructions. Since EWH fields are defined as temporal anomalies with respect to a reference epoch (t_{ref}), removal of a linear GIA trend

introduces a time-dependent uncertainty into the anomaly time series. To ensure applicability across different geophysical use cases, the GIA trend uncertainty is provided in units of cm yr^{-1}, allowing users to propagate this uncertainty consistently for their specific choice of reference epoch.

3.4.3 Leakage correction uncertainty

Spatial filtering, while necessary to suppress noise in GRACE(-FO) solutions, inevitably attenuates true geophysical signals and introduces spectral leakage: energy from signals outside a region of interest bleeds into the estimate, and vice versa. To obtain the corrected signal, a leakage correction is applied, most commonly over regions with strong spatial contrasts such as coastlines or ice-sheet margins. However, the correction itself introduces uncertainty, since it depends on the assumed spatial distribution of the signal being recovered. We asses filtering-related uncertainty using the leakage-pair methodology introduced by Dobslaw et al. (2020) and applied to decorrelation filters of the DDK family (Kusche et al., 2009). For a given filter level l, the partial leakage signal is defined as the difference between neighbouring filter strengths,

$$\lambda_l = \delta h_{l+1} - \delta h_{l-1}, \tag{6}$$

where δh_l denotes the equivalent water height field filtered with DDKl. The total leakage estimate is then obtained by scaling the partial leakage with a filter-specific coefficient,

$$\Lambda_l = c_l \, \lambda_l, \tag{7}$$

where the scale factor c_l accounts for the attenuation characteristics of the DDK filter and is determined empirically (Dobslaw et al., 2020). The values for c_l used in this study are taken directly from Dobslaw et al. (2020) and are listed in Table 4.

Table 4. Scaling coefficients c_l used for leakage estimation following Dobslaw et al. (2020).

Filter	DDK2	DDK3	DDK4	DDK5	DDK6	DDK7
c_l	2.9	3.9	4.5	4.0	4.5	4.4

Uncertainty in the leakage estimate arises from three sources: the ensemble solution spread across processing centres, the covariance between neighbouring filter strengths, and uncertainty in the scaling coefficient c_l. Using ensemble statistics across the multiple Level-2 solutions (Section 3.3.1), the variance of the partial leakage is given by

$$\sigma^2_{\lambda_l} = \sigma^2_{l+1} + \sigma^2_{l-1} - 2\,\mathrm{Cov}(\delta h_{l+1}, \delta h_{l-1}), \tag{8}$$

where σ^2_l denotes the ensemble variance of the DDKl-filtered solution. The covariance term is essential, as neighbouring DDK filters share a large fraction of their retained noise.

The variance of the total leakage estimate Λ_n is then obtained by standard error propagation of Eq. 7,

$$\sigma^2_{\Lambda_l} = c_l^2 \, \sigma^2_{\lambda_l} + \lambda_l^2 \, \sigma^2_{c_l}, \tag{9}$$

where $\sigma^2_{c_l}$ represents the uncertainty of the scaling coefficient itself. The first term reflects uncertainty due to ensemble solution variability and correlated filter responses. In contrast, the second term captures the sensitivity of the leakage estimate to imperfect knowledge of the filter attenuation characteristics. In the present study, c_l is taken as a fixed constant across ensemble members, times, and grid cells. Ideally, the uncertainty associated with c_l would also be propagated. However, only limited information on the uncertainty of these leakage coefficients is currently available. For example, Dobslaw et al. (2020) report DDK3-specific values for only four processing centres (GFZ, CSR, JPL, and ITSG), namely 3.9, 4.2, 4.4, and 3.9, respectively, corresponding to a standard deviation of approximately 0.27. No comparable estimates are available for other DDK filter levels or for the additional gravity field solutions considered in this study. For DDK3, using the available scaling-factor statistics, the neglected second term corresponds to an RMS ratio (i.e., the ratio between its RMS variance contribution and that of the first term) of approximately 17.6%. Consequently, the total leakage variance is effectively given by the first term alone in Eq. 9, as

$$\sigma^2_{\Lambda_l} \approx c_l^2 \, \sigma^2_{\lambda_l} \tag{10}$$

3.4.4 Total uncertainty

The total Level-3 1σ-uncertainty of the GRACE and GRACE-FO EWH products (subscript δh omitted for brevity) combines the individual components as

$$\sigma^2_{\mathrm{GFO}}(t) = \sigma^2_{\mathrm{sols}}(t) + \sigma^2_{\mathrm{AOD1B}}(t) + \sigma^2_{\mathrm{geoc}}(t) + \sigma^2_{h_{2,0}}(t) + \sigma^2_{h_{3,0}}(t), \tag{11}$$

where, we assume that all components are statistically independent.

Here, $\sigma^2_{\mathrm{sols}}(t)$ represents the ensemble solution variability of the Level-2 gravity field solutions and captures uncertainties related to processing choices and background modelling across analysis centres. The term $\sigma^2_{\mathrm{AOD1B}}(t)$ accounts for residual errors in the atmosphere–ocean de-aliasing corrections applied during Level-1B to Level-2 processing. The contributions σ^2_{geoc}, $\sigma^2_{h_{2,0}}$, and $\sigma^2_{h_{3,0}}$ correspond to the propagated formal errors (Eq. 5) associated with the inserted degree-1 geocenter and the replaced low-degree coefficients, respectively. The SLR contributions are removed when using the "noSLR" ancillary product.

If the user applies leakage correction, the associated uncertainty $\sigma^2_{\Lambda_l}(t)$ should be added to account for filtering-induced effects. Lastly, when correcting for GIA, the user should add the GIA trend uncertainty to the trend of the corrected signal. The propagation of this uncertainty after GIA correction follows $\sigma_{\mathrm{GIA,trend}}|t - t_{\mathrm{ref}}|$, where t_{ref} is the reference epoch for climatological studies (see Section 3.2).

3.5 Regions of interest

Within this study, uncertainties are illustrated using three major river basins that span a representative range of climatic and hydrological regimes: the Amazon, the Ganges–Brahmaputra, and the Mississippi–Missouri basins. In addition, cryospheric uncertainty characteristics are demonstrated for the two largest ice sheets, Greenland and Antarctica. Finally, for oceanic mass variability, the Zapiola Rise is included as a representative region dominated by barotropic ocean dynamics. These regions can be found shaded in Figure 3.

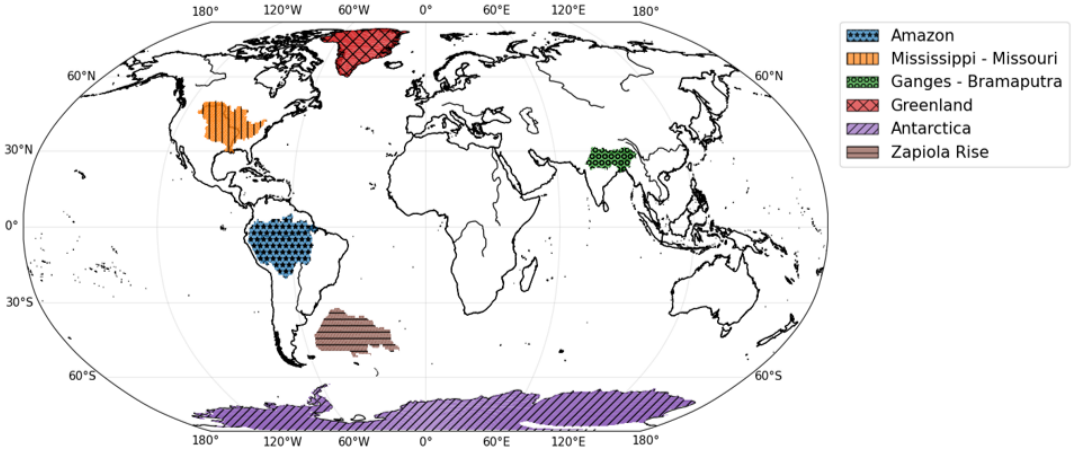


Figure 3. Geographic extent of the regions used to illustrate GRACE(-FO) uncertainty characteristics. Regional geometries follow Dahle et al. (2025).

4 Data product description

4.1 File formats and access

The dataset is distributed in NetCDF format, following the Climate and Forecast (CF) metadata conventions, which standardise variable names, units, coordinate systems, and attributes to ensure that files are self-describing and interoperable across software tools and disciplines. Separate files are provided for different DDK decorrelation filter strengths (DDK2–DDK7), allowing users to select an appropriate balance between noise reduction and spatial resolution.

The main data product follows the naming convention:

`TUD-L3-EWH_UNC-GRACEv6.2-DDK{i}-2002_2020-0.5x0.5.nc,`

where i denotes the applied DDK filter level. Complementary to the main data product, an alternative set of files is provided in which low-degree spherical harmonic coefficients are not replaced by SLR estimates. These files contain the ensemble solution uncertainty derived purely from the original GRACE(-FO) solutions and can be used by users to assess the impact of low-degree coefficient replacement. The corresponding files follow the naming convention:

`TUD-L3-EWH_UNC_noSLR-GRACEv6.2-DDK{i}-2002_2020-0.5x0.5.nc.`

In addition, three ancillary climatological products (see Section 3.2) are provided:

`TUD-L3-EWH_CLIM-GRACEv6.2-DDK{i}-2002_2020-0.5x0.5.nc,`

`TUD-L3-EWH_CLIM_CORR-GRACEv6.2-DDK{i}-2002_2020-0.5x0.5.nc,`

and

TUD-L3-EWH_CLIM_LEAKAGE-GRACEv6.2-DDK{i}-2002_2020-0.5x0.5.nc.

These files contain fitted climatological parameters, including bias, trend, acceleration, seasonal terms, and aliasing tidal coefficients, as described in Section 3.2. These parameters allow users to reconstruct climatological full or leaked signals and optionally remove dominant tidal aliasing contributions (e.g. S_2, and P_1), and other secondary contributors (i.e. S_1, and R_3), in post-processing.

Uncertainty components can be combined to form a total monthly GRACE(-FO) uncertainty using Eq. 11, while GIA corrections and their associated uncertainties can be applied separately, depending on the intended application. Comprehensive variable definitions, units, and usage examples are provided in the online README documentation accompanying the dataset. Both the dataset and documentation are publicly available at the TUD GRACE-Cube portal (https://grace-cube.lr.tudelft.nl/L2B_UNC/v6.2/) and the 4TU.ResearchData repository (Cuadrat-Grzybowski et al., 2026).

4.2 Grid and variables

The dataset is provided on a global $0.5^\circ \times 0.5^\circ$ latitude–longitude grid, with dimensions $(\mathrm{time}, \mathrm{lat}, \mathrm{lon})$, and spans the period from April 2002 to December 2020. The current temporal coverage is limited by the availability of the AOe07 residual AOD1B uncertainty product (Shihora et al., 2024), which is provided up to December 2020. The dataset will be extended beyond this period once an updated AOe07 release becomes available. The primary geophysical variable is the equivalent water height, denoted as ewh_mean.

For each DDK filter strength, the product contains an ensemble weighted-mean EWH signal derived from multiple GRACE and GRACE-FO Level-2 solutions. A summary of the available data products, including their variables, descriptions, units, and dimensions, is provided in Appendix D1.

4.2.1 Main GRACE(-FO) product

The main variables included in the TUD-L3-EWH_UNC-GRACE product are:

- ewh_mean: ensemble weighted-mean EWH signal [cm],
- ewh_mean_corr: ewh_mean corrected for GIA (reference epoch: 2008.0), geocenter motion, and aliasing tides [cm],
- ewh_mean_leakage: ensemble weighted-mean leakage correction (Λ_l, see Eq. 7) [cm],
- ewh_degree1: degree-1 (geocenter) EWH contribution [cm],
- ewh_unc_sols: ensemble solution uncertainty ($\sigma_{\delta h_l,\mathrm{sols}}$, see Eq. 3) [cm],
- ewh_unc_aod1b: atmosphere–ocean background model uncertainty [cm],
- ewh_unc_leakage: total leakage correction uncertainty (σ_{Λ_l}, see Eq. 10) [cm],
- ewh_unc_degree1: propagated degree-1 uncertainty [cm],

- ewh_unc_degree20: propagated $\bar{C}_{2,0}$ uncertainty [cm],
- ewh_unc_degree30: propagated $\bar{C}_{3,0}$ uncertainty [cm],
- ewh_gia_mean: ensemble mean GIA trend [cm yr^{-1}],
- ewh_gia_unc: GIA trend uncertainty [cm yr^{-1}],
- weights: normalised, time-dependent ensemble weights ($\bar{w}_{l,i}$, see Eq. 4) used to compute the weighted ensemble mean and associated uncertainties, provided for each contributing solution with dimensions $(\mathrm{time}, \mathrm{member})$.

All EWH grids contain time-variable gravity signals represented by spherical harmonic degrees 2 to 60. Degree-1 (geocenter) contributions are provided separately in the variable ewh_degree1 and may be added by the user if required. For clarity, Appendix D2 (Table D6) summarises which geophysical components (degree-1, $\bar{C}_{2,0}$, $\bar{C}_{3,0}$, and higher degrees) are represented in each variable. We also provide the ensemble weights (see Eq. 4) explicitly as part of the data product. The member dimension corresponds to the string identifier of each contributing Level-2 solution (i.e. the originating data centre), allowing users to reconstruct (using Eq. 3) the ensemble mean and uncertainty estimates exactly.

4.2.2 NoSLR ancillary product

An ancillary product is provided for analyses requiring SLR-free ensemble statistics. The TUD-L3-EWH_UNC_noSLR-GRACE files contain:

- ewh_mean: ensemble weighted-mean EWH signal with no SLR replacement [cm],
- ewh_unc_sols: ensemble solution uncertainty with no SLR replacement [cm],
- weights: normalized, time-dependent ensemble weights with dimensions $(\mathrm{time}, \mathrm{member})$.

This product is intentionally small, containing only variables needed to perform SLR-free analyses while reproducing the weighted ensemble mean and uncertainty estimates (using Eq. 3). The geophysical content of this ancillary product is summarised in Appendix D2 (Table D7).

4.2.3 Climatology products

In addition to the EWH gridded product, two CLIM ancillary products are provided to enable climatological reconstruction of the EWH signal. The two main climatological products, TUD-L3-EWH_CLIM-GRACE and TUD-L3-EWH_CLIM_CORR-GRACE, share an identical variable structure. Throughout this section, the prefix var appearing in variable names refers to ewh_mean in the uncorrected product (TUD-L3-EWH_CLIM-GRACE) and to ewh_mean_corr in the fully post-processed product (TUD-L3-EWH_CLIM_CORR-GRACE); for example, var_clim corresponds to ewh_mean_clim or ewh_mean_corr_clim, respectively.

Both products contain the following variables:

- Individual regression parameter variables (e.g., var_bias, var_trend, and var_acc) are additionally provided to facilitate direct access and use by data product users. These variables describe the long-term, seasonal, and tidal variability of the EWH signal (see Eq. 2) and include:
  - var_bias: constant offset term [cm],
  - var_trend: linear trend coefficient [cm yr^{-1}],
  - var_acc: quadratic (acceleration) term [cm yr^{-2}],
  - var_annual_cos, var_annual_sin: annual harmonic terms [cm],
  - var_semiannual_cos, var_semiannual_sin: semiannual harmonic terms [cm],
  - var_{tide}_cos, var_{tide}_sin: cosine and sine coefficients [cm] associated with selected tidal constituents (S_2, P_1, S_1, and R_3).
- t_clim: numeric time variable compatible with the regression model, expressed in fractional years and centred at 2008.0.
- var_clim: climatological fit ($\delta h_l^{\mathrm{clim}}$) of the ensemble weighted-mean EWH signal [cm], with dimensions $(\mathrm{time}, \mathrm{lat}, \mathrm{lon})$.
- var_tides: climatological tidal aliasing fit of the ensemble weighted-mean EWH signal [cm], with dimensions $(\mathrm{time}, \mathrm{lat}, \mathrm{lon})$.
- residuals: difference between the ensemble mean and climatological fit $\left(\overline{\delta h_l}(t) - \delta h_l^{\mathrm{clim}}(t)\right)$ [cm], with dimensions $(\mathrm{time}, \mathrm{lat}, \mathrm{lon})$.
- var_beta: gridded climatological regression coefficients with dimensions $(\mathrm{lat}, \mathrm{lon}, \mathrm{coeff})$, retained for compatibility and reproducibility with the previous product version (v5).
- var_beta_std: unbiased standard deviation of the post-fit residuals between the ensemble-mean EWH time series and its fitted climatological model, i.e., the square root of the unbiased variance of $\left(\overline{\delta h_l}(t) - \delta h_l^{\mathrm{clim}}(t)\right)$.

Together, the regression parameter variables and t_clim allow users to reconstruct the climatological EWH signal using Eq. 2, consistently with the time dimension of the main product. The time variable t_clim can also be used to remove the fitted climatological contribution from the GRACE(-FO) signal (i.e., var). The same variable naming convention is applied to the leakage climatological ancillary product TUD-L3-EWH_CLIM_LEAKAGE-GRACE, allowing users to evaluate the effect of leakage on the climatological fit by adding the leakage contribution to the main climatological fit.

5 Technical validation

To verify our combined methodology, we compute the spatial RMS of each solution over the open oceans for each DDK filter level. Prior to this calculation, deterministic signals are removed by fitting and subtracting a climatological model individually

for each solution, comprising a bias, linear trend, quadratic term, annual and semi-annual components, and the dominant tidal aliases. The open ocean is then used as a noise proxy, on the assumption that once these systematic contributions are accounted for, any remaining signal reflects noise rather than true geophysical variability.

The RMS is computed over ocean regions with minimal geophysical signal, applying the same 500 km coastal buffer and Argentine Basin mask as described in Section 3.3.1. The remaining oceanic signals are therefore assumed to empirically represent the intrinsic solution noise as a function of time, as seen in Figure 4. For reference, the individual solutions from CSR, JPL, GFZ, and ITSG, as well as the COST-G combination, are included in the figure alongside the TUD ensemble mean. Furthermore, a sensitivity analysis is performed on the influence of DDK filter level, where for each filter strength the open ocean RMS is averaged over the full temporal record of each data centre solution and visualised in Figure 5.

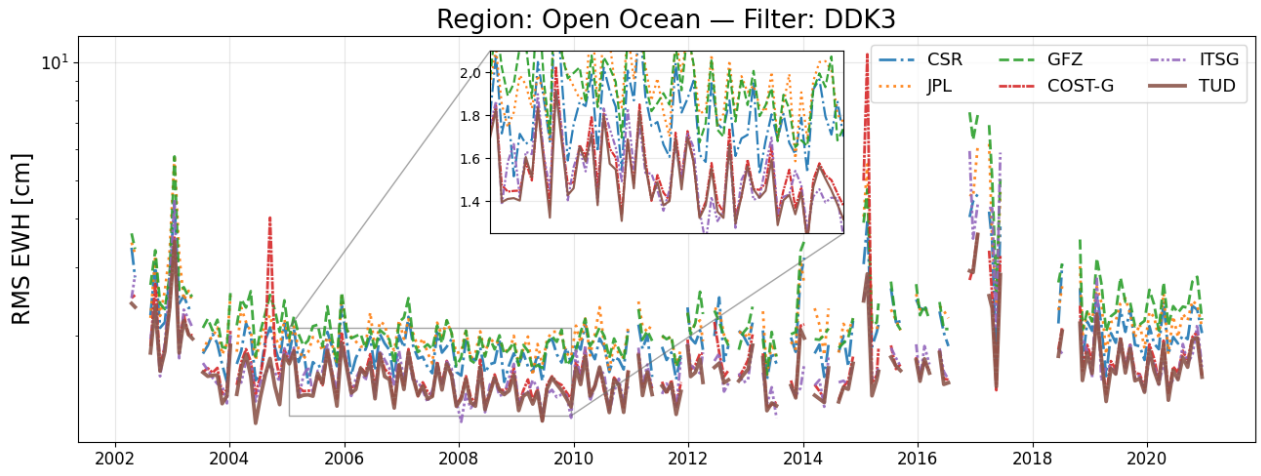


Figure 4. Spatial RMS over the open oceans for the five most recent Level-2 GRACE/GRACE-FO solutions (CSR, JPL, GFZ, ITSG, and the combined COST-G), compared against the TUD ensemble mean. A DDK3 filter is applied, together with a 500 km coastal buffer and an additional mask over the Argentine ocean basin.

From Figure 4, we observe that for the widely used DDK3 filter (Kusche et al., 2009; Qian et al., 2022; Werth et al., 2009), the TUD ensemble mean exhibits the lowest average open-ocean RMS of 1.66 cm. Comparable performance is obtained by ITSG-Grace2018 and COST-G (~ 1.78), followed by CSR (~ 2.06 cm), JPL (~ 2.25 cm), and finally GFZ (~ 2.35 cm). This ranking is further corroborated by Figure 5, which summarizes the temporal mean RMS as a function of DDK filter level.

A notable feature is that the combined COST-G (RL02.1) solution exhibits elevated noise levels above 4 cm during orbit repeat periods (notably around 09/2004 and 02/2015, with RMS values of 4 and 10 cm, respectively), exceeding those of all other solutions by a factor of two. We hypothesise that this behaviour is primarily related to the inclusion of the APM-SYSU solutions in the COST-G ensemble. While APM-SYSU demonstrates low noise levels during nominal periods (with a ΔRMS^{tot} from 5 to 10%), it exhibits some of the highest RMS values during orbit repeat patterns (see Section 3.3). In contrast, the TUD ensemble mean maintains low RMS levels during these repeat periods. This behaviour is largely consistent across

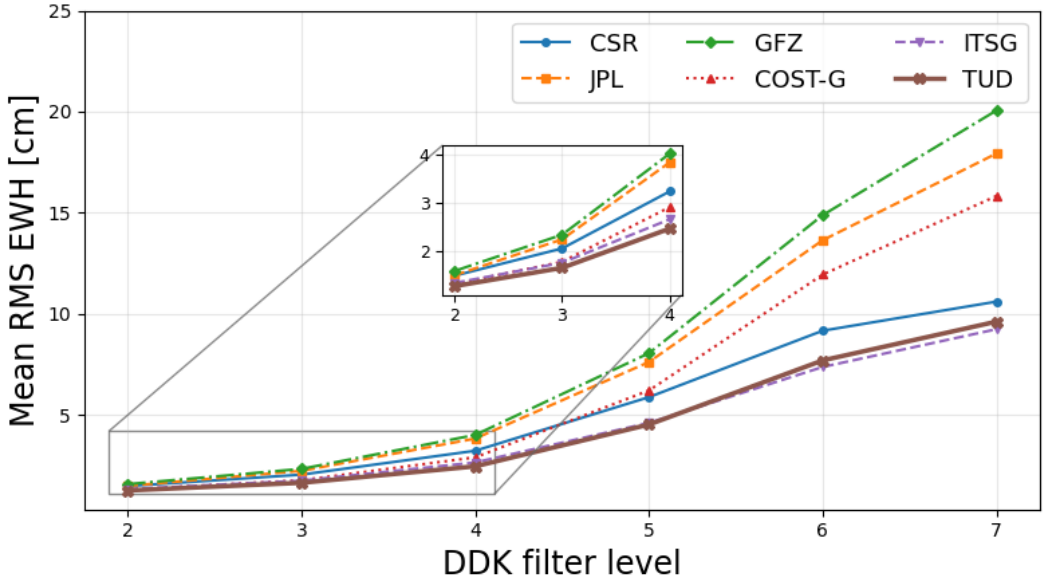


Figure 5. Temporal mean of the open-ocean spatial RMS as a function of DDK filter level for the five most recent Level-2 GRACE(-FO) solutions (CSR, JPL, GFZ, ITSG, and the combined COST-G), compared with the TUD ensemble mean product.

DDK filter levels. For DDK levels 2 to 5, the TUD ensemble mean exhibits the lowest mean EWH RMS among all solutions (Figure 5). The ITSG solution follows closely, with a constant difference ranging of approximately 0.1 cm at DDK2,4,5 with a maximum of 0.2 cm at DDK3. As expected, COST-G exhibits RMS values of 1.32 and 1.78 cm for DDK2–3, respectively, similar to ITSG. From DDK4 onward, however, COST-G shows a systematic 1 cm increase in RMS, most likely driven by enhanced noise during orbit repeat periods, and reaches values comparable to CSR ($\sim$ 6 cm) at DDK5. For the weakest filtering levels (DDK6–7), COST-G displays a pronounced RMS increase relative to DDK5, becoming the third noisiest solution, with RMS values reaching up to 11.9–15.9 cm.

For the weaker filtering levels (DDK6–DDK7), ITSG achieves the lowest RMS, with the TUD ensemble mean following closely behind by only approximately 0.3 cm. While COST-G maintains comparatively low noise levels across all filter strengths, CSR exhibits lower RMS values than COST-G for DDK5–DDK7, with the difference increasing from approximately 0.3 cm at DDK5 to about 5.1 cm at DDK7. In contrast, GFZ and JPL display the highest RMS values, reaching approximately $\sim$ 7.7 cm at DDK5 and increasing to $\sim$ 18.0 cm (JPL) and $\sim$ 20 cm (GFZ) at DDK7. This behaviour reflects the differing noise characteristics of the individual solutions under reduced filtering strength, where high-frequency noise becomes increasingly pronounced. Furthermore, the same analysis has been performed over the Sahara and Arabian deserts, two geophysically quiet regions (not shown here), confirming the robustness of these relative performance patterns. Overall, the results indicate that the ensemble mean provides a stable solution across DDK filter strengths and supports its use as a representative combined product in this study.

6 Results

6.1 Uncertainty results

6.1.1 AOD1B uncertainty

As previously mentioned, the uncertainty associated with the AOD1B de-aliasing product is defined as the temporal RMS within each month of the 6-hourly AOe07 model fields. This approach provides an estimate of the residual atmosphere–ocean variability that is not removed during the de-aliasing step. In the following, we analyse the temporal RMS of the monthly AOD1B uncertainties over the period 2002–2020.

Figure 6 shows the spatial distribution of the temporal RMS of the AOD1B uncertainties for the case of DDK3-filtered solutions. Although the dataset provides equivalent estimates for the full range of DDK filters (DDK2–DDK7), the DDK3 case is shown here as a representative example commonly used in geophysical applications.

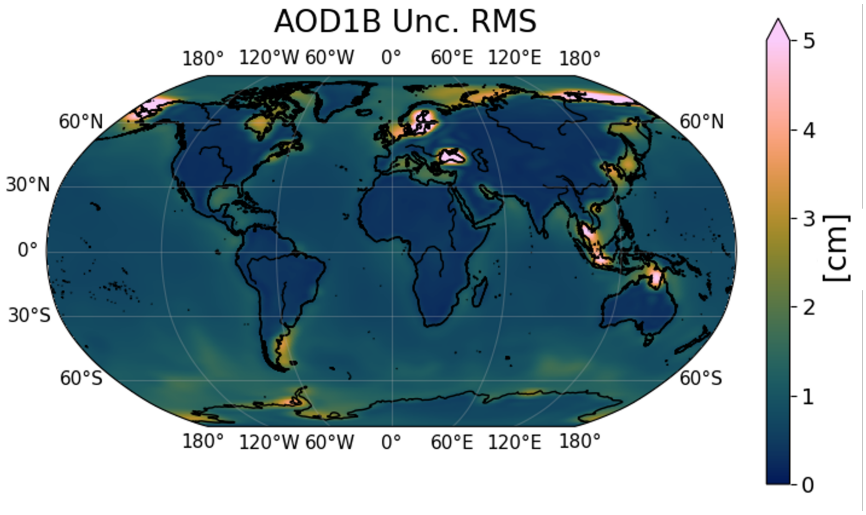


Figure 6. Spatial distribution of AOD1B uncertainty computed from the AOe07 spherical harmonic coefficients propagated to EWH and filtered with DDK3 (degree and order 2–60). The global mean RMS over 2002–2020 is 1.04 cm EWH.

The resulting AOD1B uncertainty field exhibits a global mean RMS of approximately 1.04 cm EWH, confirming that it represents a secondary but non-negligible contribution to the overall uncertainty budget. However, the spatial distribution is strongly inhomogeneous. Elevated values are predominantly observed along coastal zones and marginal seas. In these regions, RMS values locally reach 3–5 cm. In contrast, uncertainties over continental interiors are substantially smaller and typically remain below 0.5 cm, reflecting the reduced influence of oceanic mass variability and the greater stability of the atmospheric component over land.

6.1.2 GIA ensemble statistics

GIA uncertainty is quantified using an ensemble of 56 global GIA model realisations compiled by Bagge et al. (2023), following the same methodology as in Eicker et al. (2024). The ensemble spans a range of Earth rheology and ice-history assumptions and provides an estimate of the variability associated with these GIA model configurations. For each grid point, we compute the ensemble mean GIA signal, the standard deviation (1σ), as well as the minimum and maximum deviations relative to the ensemble mean. The ensemble mean is used as the best-estimate GIA correction, while the ensemble standard deviation reflects the uncertainty arising from differences in the underlying priors within the ensemble. The minimum and maximum deviations are included to capture the range of model outcomes and highlight regions where GIA predictions diverge most strongly. We note that this uncertainty estimate represents the spread within the selected ensemble and does not encompass the full uncertainty associated with all possible GIA modelling frameworks and assumptions.

The uncertainty estimation is performed consistently for multiple decorrelation filter settings (DDK2–DDK7), allowing users to apply the corresponding GIA uncertainty fields together with the associated DDK-filtered TUD ensemble means or with any other GRACE(-FO) solution processed using the same filter. Figure 7 shows an example of the resulting ensemble statistics for the DDK3-filtered GIA fields, illustrating the spatial distribution of the ensemble mean (Figure 7a), standard deviation (Figure 7b), and extreme deviations (Figure 7c,d). Regions of particularly large GIA uncertainty coincide with formerly glaciated areas, such as North America, Northern Europe (Fennoscandia), and polar regions such as Southern Greenland, and Antarctica, whereas low-latitude regions exhibit comparatively small ensemble spread. Typical standard deviations (Figure 7b) are approximately 1.2–$2\ \mathrm{cm\ yr^{-1}}$ in North America, 0.5–$0.9\ \mathrm{cm\ yr^{-1}}$ in Northern Europe, 1.5–$2\ \mathrm{cm\ yr^{-1}}$ in Southern Greenland, and around $0.5\ \mathrm{cm\ yr^{-1}}$ in Antarctica, with localized regions reaching $0.6\ \mathrm{cm\ yr^{-1}}$.

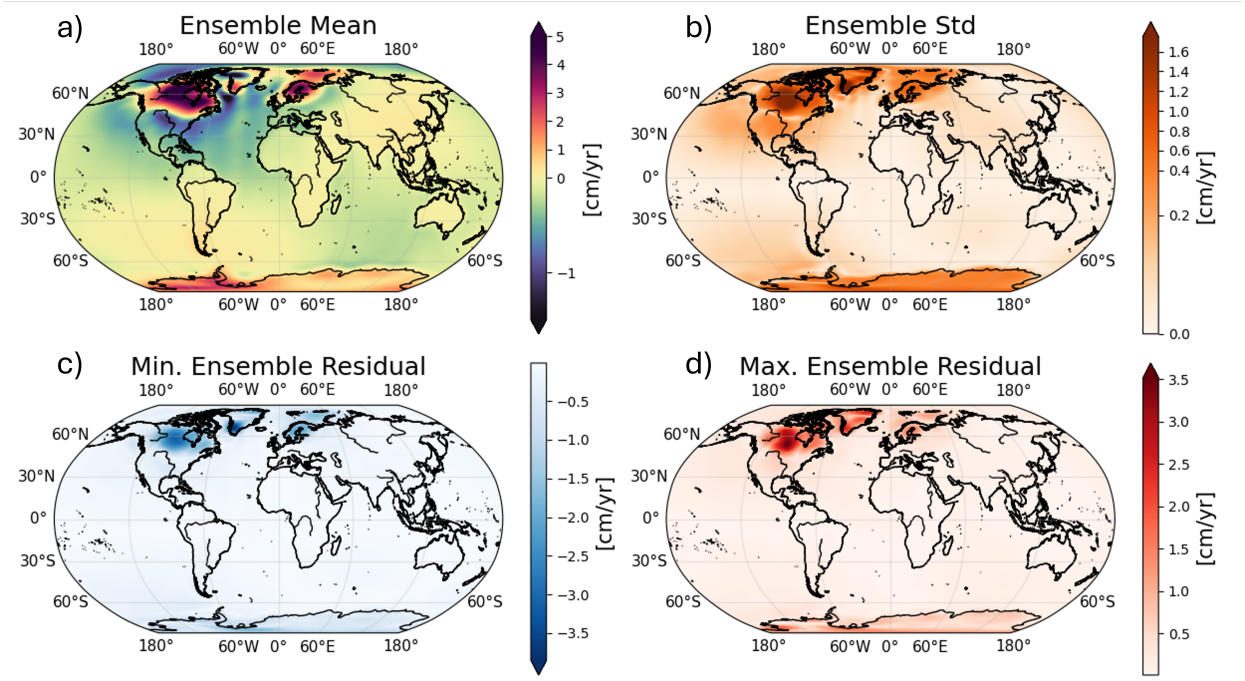


Figure 7. Ensemble statistics of GIA derived from 56 global GIA models (Bagge et al., 2023) (filtered using DDK3). Shown are the ensemble mean (a), standard deviation (b), and the minimum and maximum deviations relative to the ensemble mean (c,d).

6.1.3 Hydrology applications

Hydrological mass variations in many regions are characterised by large-amplitude seasonal signals, often accompanied by pronounced interannual variability. To assess the performance of the ensemble approach in this context, time series of EWH are analysed for three major river basins: the Amazon, the Ganges–Brahmaputra, and the Mississippi–Missouri (see Figure 3). All solutions have been corrected for the ensemble-mean GIA signal and for aliased tidal constituents, while the degree-1 geocentre signal has been added, and the low-degree SLR coefficients have been updated to replace the corresponding components in the original solutions.

For each basin, averaged EWH time series are extracted from selected Level-2 solutions and compared with the TUD ensemble mean. Uncertainty envelopes shown in Figure 8 represent $\pm 2\sigma$ (approximately 95% confidence) contributions from three components: ensemble solution uncertainty, AOD1B uncertainty, and the combined low-degree replacement uncertainty (degree-1 and SLR-derived $\bar{C}_{2,0}$ and $\bar{C}_{3,0}$). The basin-scale uncertainties are obtained by propagating the variance of the corresponding gridded uncertainty fields, assuming independent grid-cell contributions. Each uncertainty component is shown separately to illustrate its relative contribution to the total uncertainty. The $\pm 2\sigma$ interval is adopted here as a representative visualisation; all uncertainty components are provided in the data product as standard deviations, allowing users to construct

application-specific confidence levels. The ensemble mean is shown together with five solutions (CSR, JPL, GFZ, ITSG, and COST-G). Basin-mean EWH characteristics and GIA trend statistics are summarised in Table 5.

Table 5. Basin-averaged characteristics of EWH variability and GIA correction (DDK3 filtered, degree/order 1–60). Shown are the annual amplitude and linear trend estimated from the GRACE(-FO) EWH (GIA-uncorrected) time series, together with the ensemble-mean GIA trend and its associated uncertainty derived from 56 global GIA models (Bagge et al., 2023).

Basin	Annual Amplitude [cm]	Trend [cm yr^{-1}]	GIA [cm yr^{-1}]	GIA uncertainty [cm yr^{-1}]
Amazon	20.02	0.28	0.01	0.02
Mississippi–Missouri	6.08	−0.14	−0.70	0.33
Ganges–Brahmaputra	13.06	−1.19	0.20	0.08

For the Amazon and Ganges–Brahmaputra basins, both the ensemble-mean GIA trend and its associated uncertainty are small, remaining below 0.1 cm yr^{-1}. Even when accumulated over a decade, the corresponding GIA uncertainty remains below ~ 1 cm and is negligible compared to the seasonal amplitudes of approximately 20 cm and 13 cm, respectively. In addition, the ensemble-mean GIA trends (0.01 and 0.20 cm yr^{-1}) are small relative to the observed EWH trends, indicating that GIA corrections play a minor role in the interpretation of long-term hydrological variability in these basins. In contrast, the Mississippi–Missouri basin exhibits a substantially larger ensemble-mean GIA trend (-0.70 cm yr^{-1}) and associated uncertainty (0.33 cm yr^{-1}). Over a decadal timescale, this uncertainty accumulates to approximately 3 cm, which is comparable to the basin's seasonal amplitude (6 cm) and exceeds the uncorrected EWH trend (-0.14 cm yr^{-1}). As a result, GIA-related uncertainty becomes a non-negligible contributor to trend interpretation in this basin. A similar behaviour is observed for the Mackenzie River basin (not shown), which is located closer to the centre of the GIA signal in northern North America. There, the ensemble-mean GIA trend amounts to 2.86 ± 1.14 cm yr^{-1}, compared to an annual amplitude of 4.58 cm and an observed EWH trend of 0.98 cm yr^{-1}. In this case, both the magnitude and uncertainty of the GIA correction are comparable to, or exceed, the hydrological trend itself.

Considering the remaining uncertainty components, ensemble solution uncertainty constitutes the dominant contribution in all three basins. When expressed at the $\pm 2\sigma$ level, it reaches approximately 2.5–3.5 cm, reflecting differences among processing centres, background models, and noise characteristics. AOD1B uncertainty and the combined low-degree replacement uncertainty are smaller but comparable in magnitude, each contributing approximately 0.6–0.8 cm at the $\pm 2\sigma$ level.

Detailed basin-averaged statistics of ensemble solution uncertainty, AOD1B uncertainty, and combined low-degree replacement uncertainty are provided in Appendix E1 (Table E1). These statistics confirm that ensemble uncertainty dominates the uncertainty budget for large river basins, while AOD1B and low-degree uncertainties form secondary but non-negligible contributions. Overall, the results demonstrate that, although GIA uncertainty is negligible for most low-latitude hydrological basins, robust interpretation of seasonal and interannual variability requires explicit consideration of ensemble uncertainty together with background-model-related uncertainties.

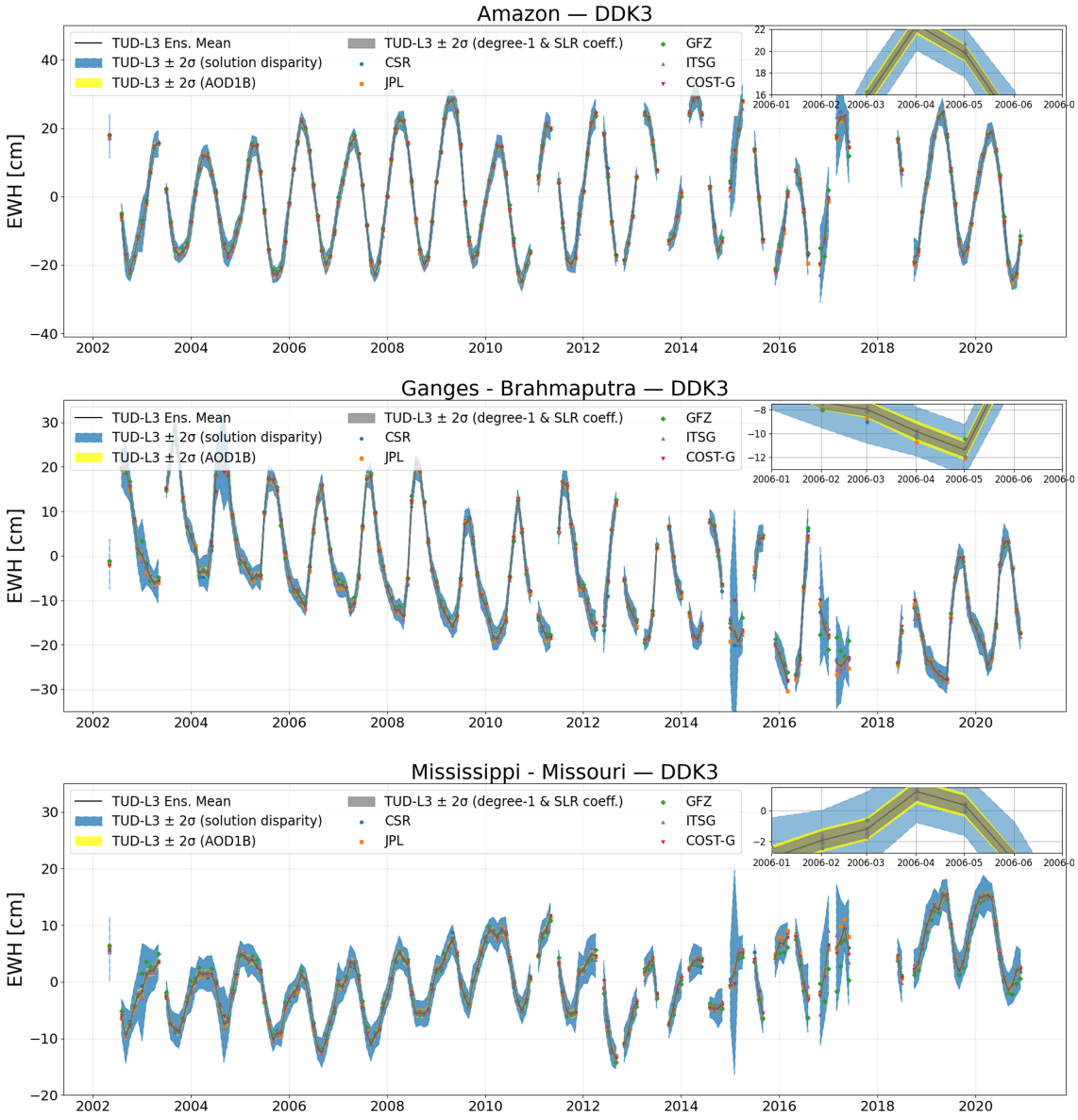


Figure 8. Basin-averaged EWH time series for three major river basins: the Amazon, Ganges–Brahmaputra, and Mississippi-Misouri, derived from selected individual Level-2 GRACE/GRACE-FO DDK3-filtered-solutions (CSR, JPL, GFZ, ITSG, and COST-G) and compared with the TUD ensemble mean (for degree/order 1 to 60). Shaded envelopes indicate the ensemble uncertainty, representing the spread among contributing solutions, quantified by the 2σ standard deviation, and uncertainties related to AOD1B, and the low-degree coefficients (degree-1 and SLR) combined uncertainty.

6.1.4 Glaciology applications

Glaciological mass-change signals are often dominated by long-term trends, although seasonal variability can be significant in regions with strong accumulation–ablation cycles or dynamic ice-flow processes. This places strong requirements on the treatment and propagation of low-frequency errors. We therefore focus on the two largest ice sheets, Antarctica and Greenland, to assess the performance of the ensemble approach for cryospheric mass-balance applications. Using the same methodology as in the previous sections, spatially averaged mass-change time series are derived from each Level-2 solution and compared with the TUD ensemble mean. Figure 9 shows the resulting time series together with their associated $\pm 2\sigma$ (95%) uncertainty envelopes, explicitly illustrating the relative contributions of ensemble solution uncertainty, AOD1B uncertainty, and the combined low-degree (degree-1 and SLR) uncertainty. Region-averaged GIA trend statistics are reported separately in Table 6.

Table 6. Region-averaged characteristics of EWH variability and GIA correction (DDK3 filtered, degree and order 2–60) for Greenland and Antarctica. Shown are the annual amplitude, absolute minimum–maximum range, and linear trend estimated from the GRACE(-FO) EWH (GIA-uncorrected) time series, together with the ensemble-mean GIA trend and its associated uncertainty derived from 56 global GIA models (Bagge et al., 2023).

Region	Ann. Amplitude [cm]	|Min–Max| [cm]	Trend [cm yr^{-1}]	GIA trend [cm yr^{-1}]	GIA uncertainty [cm yr^{-1}]
Greenland	4.09	138.19	-7.61	0.29	1.11
Antarctica	1.09	7.26	-0.14	0.98	0.41

For Antarctica (Figure 9a), the ensemble uncertainty represents the dominant uncertainty contribution, with 95% confidence levels reaching approximately 1.4–4.0 cm. AOD1B uncertainty forms the second largest component, contributing at the level of approximately 2–4 cm. The combined low-degree uncertainty associated with degree-1 and SLR coefficients is substantially smaller, with a typical 95% confidence magnitude of about 1.0–1.2 cm.

A similar hierarchy is observed for Greenland (Figure 9b). Here, ensemble uncertainty again dominates, with 95% confidence levels of approximately 2.0–5.0 cm, followed closely by AOD1B uncertainty at roughly 1.6–3.0 cm. The combined degree-1 and SLR uncertainty remains the smallest contribution, with magnitudes comparable to those found for Antarctica (approximately 1.0–1.2 cm).

Comparing these uncertainties to the magnitude of the observed mass-change signals highlights their relevance for glaciological applications. For Antarctica, where the basin-averaged signal range is relatively small ($|\text{min–max}| = 7.61$ cm), the ensemble uncertainty and AOD1B uncertainties already constitute a substantial fraction ($\sim 22\%$) of the total signal variability. In addition, the ensemble-derived GIA trend uncertainty of 0.41 cm yr^{-1} (Table 6) propagates into several centimetres over decadal time scales, becoming comparable to the dominant Level-3 uncertainty contributions. In Greenland, although the absolute mass-change signal is much larger ($|\text{min–max}| \approx 140$ cm), ensemble uncertainty and AOD1B uncertainties remain non-negligible ($\sim 1\%$) and must be accounted for in trend analyses. Here, the larger GIA trend uncertainty of 1.11 cm yr^{-1} similarly accumulates over time and directly impacts (by $\sim 8\%$) long-term mass-balance estimates. In contrast, the combined

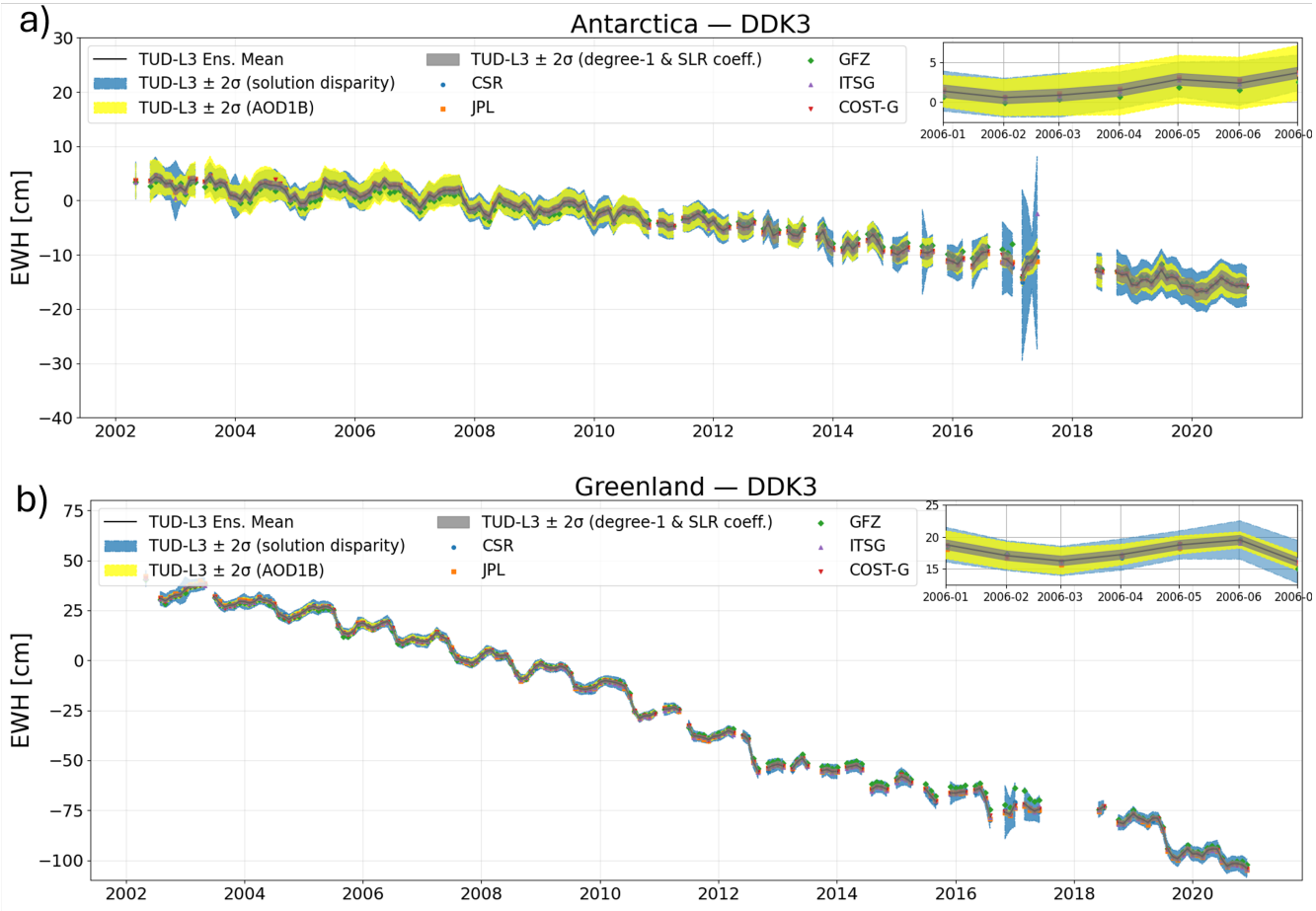


Figure 9. Land-averaged EWH time series for (a) Antarctica and (b) Greenland, derived from selected individual Level-2 GRACE/GRACE-FO DDK3-filtered solutions (CSR, JPL, GFZ, ITSG, and COST-G) and compared with the TUD ensemble mean (degree and order 2–60). Shaded envelopes indicate $\pm 2\sigma$ (95%) uncertainty contributions associated with ensemble uncertainty, AOD1B de-aliasing, and the combined low-degree (degree-1 and SLR) uncertainty.

low-degree uncertainty consistently represents the smallest contribution (~ 0.43–8%) for both ice sheets. Temporal statistics of these uncertainty components, summarised in Appendix E2 (Table E3).

6.1.5 Ocean circulation studies

Oceanic mass variability exhibits low signal-to-noise ratios (compared to hydrological and glaciological signals) and is strongly influenced by background model errors, particularly in ocean tide and de-aliasing corrections. As a representative case study for ocean circulation processes, we examine mass variability in the Argentine Basin, with a focus on the Zapiola Rise (Figure 3).

This region is well known in the context of the GRACE(-FO) mission for its sensitivity to temporally varying ocean circulation (Cuadrat-Grzybowski et al., 2025; Ghobadi-Far et al., 2022; Yu et al., 2018).

Area-averaged time series from Level-2 solutions are compared to the TUD ensemble mean (with all applied post-processing corrections) in Figure 10a, together with all considered uncertainty components expressed as $\pm 2\sigma$ (95%) intervals. The temporal Root-Median-Square (RMedS) of the ensemble mean signal (Figure 10b) and of the individual uncertainty contributions (Figure 10c–e) provides a complementary spatial perspective on the oceanic signal-to-noise characteristics.

The characteristic dipole mass variability associated with the Zapiola Rise is clearly identifiable in both the temporal and spatial diagnostics. In the basin-averaged time series (Figure 10a), the signal exhibits a cyclical behaviour with an amplitude of approximately 1.4 cm EWH. The corresponding spatial signature is evident in the RMedS of the ensemble mean signal (Figure 10b), which reveals a well-defined dipolar structure centred on the Zapiola Rise, with local magnitudes reaching approximately 3–5 cm.

In terms of uncertainty contributions, the ensemble uncertainty constitutes the largest component in this region. As shown by the time series envelopes and the RMedS distribution (Figure 10d), the 95% ensemble uncertainty reaches typical magnitudes of approximately 2.4–3.1 cm. This component primarily reflects residual noise and differences in background modelling choices, including ocean tide representations, among the contributing solutions. The AOD1B-related uncertainty is of comparable magnitude and forms the second largest contribution, with 95% confidence levels of approximately 1.4–2.2 cm (Figure 10c). These uncertainties are spatially concentrated near coastal regions and leak into the Zapiola Rise area, underscoring the sensitivity of oceanic mass estimates to imperfect de-aliasing of high-frequency atmosphere–ocean variability.

The combined uncertainty associated with SLR-based low-degree coefficients and degree-1 (geocentre) corrections is substantially smaller. As shown in Figure 10e, this contribution has a basin-averaged 95% uncertainty level with a temporal mean of approximately 0.6 cm, making it the least significant uncertainty source in this region.

6.1.6 Leakage correction uncertainties

Leakage induced by spatial filtering is particularly pronounced in regions characterised by large signal amplitudes and large spatial gradients. While decorrelation filtering substantially reduces north-south striping noise in GRACE(-FO) solutions, it also attenuates true geophysical signals and redistributes signal power across basin boundaries. The DDK3 filter is widely used in hydrological applications as a compromise between noise reduction and spatial resolution. For this reason, the following analysis focuses on the leakage correction and its associated uncertainty for DDK3 filtered solutions, although leakage corrections for the full range of DDK filters (DDK2–DDK7) are also provided in the dataset.

The spatial characteristics of the leakage correction are first examined using climatological model fits, following the approach of Section 3.4.3 (Dobslaw et al., 2020). Figure 11 shows the climatological leakage correction expressed in terms of its linear trend, bias, and acceleration (Figure 11a–c), as well as its seasonal components. The annual leakage signal is represented by the cosine, sine, and amplitude terms (Figure 11d–f, respectively), while the semiannual leakage signal is shown analogously in Figure 11g–i respectively. The seasonal leakage amplitudes are spatially highly localised, with elevated values concentrated along regions of strong hydrological variability. In addition, pronounced leakage patterns are observed along

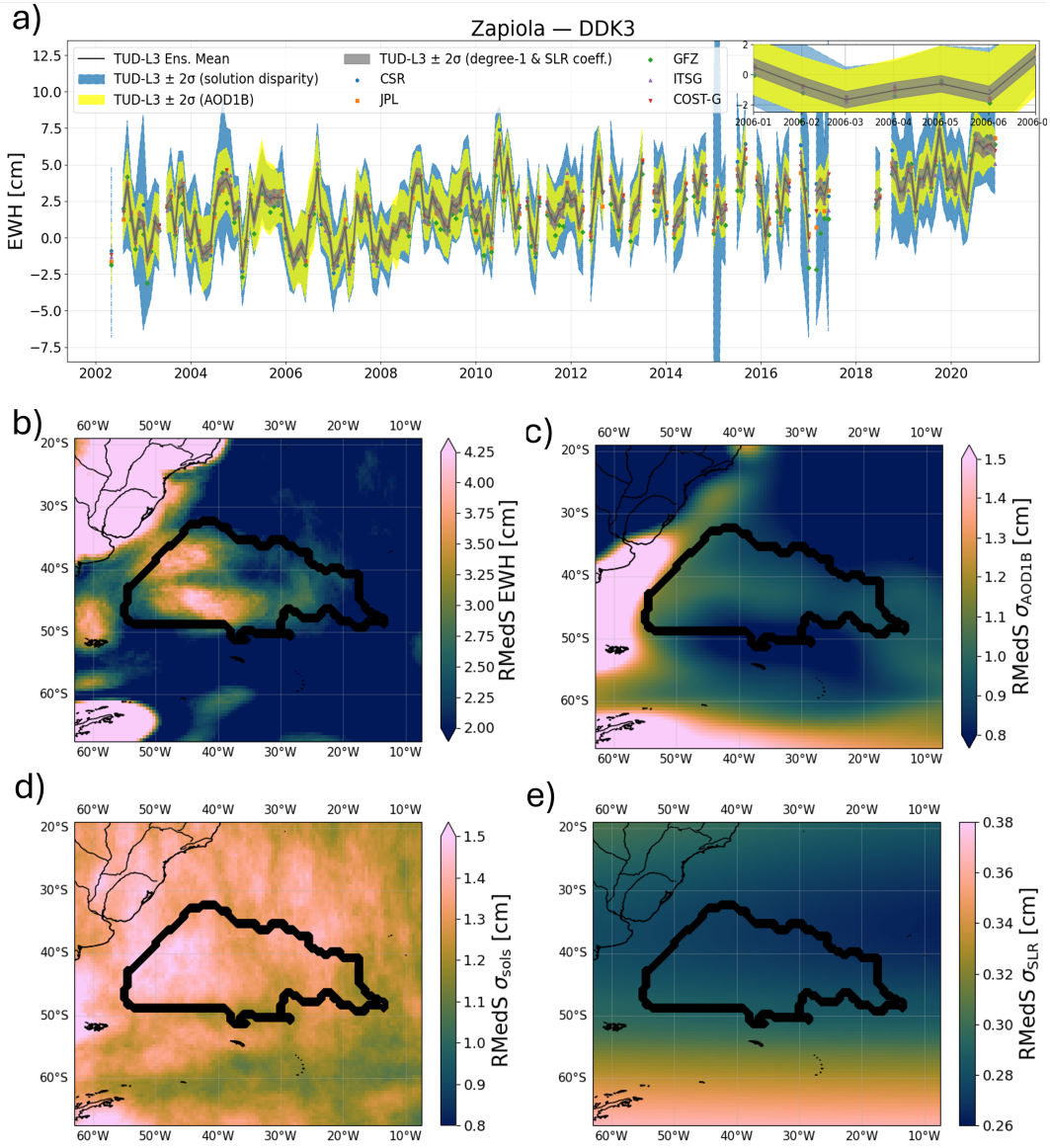


Figure 10. EWH results for the Argentine Basin (DDK3 filtered, degree/order 2–60). (a) Basin-averaged EWH time series derived from selected Level-2 GRACE/GRACE-FO solutions (CSR, JPL, GFZ, ITSG, and COST-G), shown together with the TUD ensemble mean. Shaded envelopes denote $\pm 2\sigma$ (95%) uncertainty contributions associated with ensemble solution uncertainty, AOD1B de-aliasing, and combined SLR and degree-1 corrections. The temporal Root-Median-Square (RMedS) of 1σ fields of (b) the corrected TUD ensemble mean EWH signal (~ 3 cm), (c) the AOD1B uncertainty component (~ 0.7 cm), (d) the ensemble uncertainty (~ 1.35 cm), and (e) the low-degree SLR and degree-1 combined uncertainty (~ 0.26 cm) are also shown. Values in parentheses denote the regional averages.

coastal zones, reflecting land–ocean signal leakage in regions with strong land–sea mass contrasts. In the polar regions, these effects are most evident in the trend and acceleration terms, consistent with the patterns reported by Dobslaw et al. (2020). In contrast, the seasonal leakage signals are concentrated along the coastlines of mid-latitude Africa, and much of the South American continent, with elevated amplitudes also observed along western North America, particularly in the sine components (Figure 11e and h) of the annual and semiannual terms. The bias term in particular largely reflects scaled noise introduced by the DDK4-filtered solution used in the leakage pair construction, which is evident from the pronounced north–south striping visible in Figure 11b.

The basin-scale impact of leakage correction is illustrated in Figure 12, showing basin-averaged leakage correction and uncertainty (see Section 3.4.3) time series for the Ganges–Brahmaputra, Mississippi–Missouri, and Amazon basins. We use a $\pm 1\sigma$ range for visual clarity, as the corresponding $\pm 2\sigma$ envelope would obscure the leakage correction time series. For the Ganges–Brahmaputra basin, the leakage correction exhibits a clear seasonal signal with a basin-mean amplitude of approximately 3.39 cm and a linear trend of about -0.60 cm yr^{-1} (Figure 12b). However, this signal is accompanied by a large mean leakage uncertainty of approximately 10.6 cm, which substantially exceeds both the seasonal amplitude and the long-term trend. A similar behaviour is observed for the Mississippi–Missouri basin, where a localised leakage correction trend of approximately -0.18 cm yr^{-1} is present in the basin-averaged time series (Figure 12c), while the associated mean leakage uncertainty remains high at about 9.13 cm. The basin-averaged behaviour discussed above is supported by the temporal statistics of the leakage correction uncertainty summarised in Appendix E1.2. These statistics confirm that, for all three hydrological basins, leakage uncertainty substantially exceeds the magnitude of the basin-mean leakage correction itself, despite strong spatial cancellation in the averaged signal. For completeness, analogous leakage uncertainty statistics for the polar regions are provided in Appendix E2.2. For the Amazon basin, the leakage climatological signal shows substantially larger annual and semiannual amplitudes within the basin, reaching approximately 20 cm and 4 cm, respectively, as evident from the spatial amplitude maps in Figure 11f and i. These amplitudes are highly localised and appear as spatially adjacent positive and negative leakage-induced mass anomalies across the basin (see Amazon, central Africa and Ganges-Brahmaputra river basins in Figure 11d–e for the annual component and Figure 11g–h for the semi-annual component). When averaged over the full basin area, these opposing contributions largely cancel, resulting in a basin-mean leakage correction that remains bounded within approximately ± 2 cm in the time series (Figure 12a). Despite this small basin-mean leakage correction for the Amazon, the basin-averaged leakage uncertainty inferred from the time series has a temporal mean of approximately 10.75 cm. This indicates that strong spatial averaging substantially reduces the apparent magnitude of the leakage correction while leaving the associated uncertainty largely unaffected. Consequently, basin-averaged leakage corrections may appear small even in the presence of pronounced local leakage signals visible in the spatial climatologies, and their interpretation therefore requires caution in basin-scale analyses, particularly when sub-basin or regional processes are of interest.

6.2 Global spatial distribution of signal and uncertainties

To complement the application-specific analyses, we compute the temporal RMS of the DDK3-filtered Level-3 solutions at each grid cell and present the global results in Figure 13. Panels (a) and (b) show the RMS of the ensemble-mean EWH signal

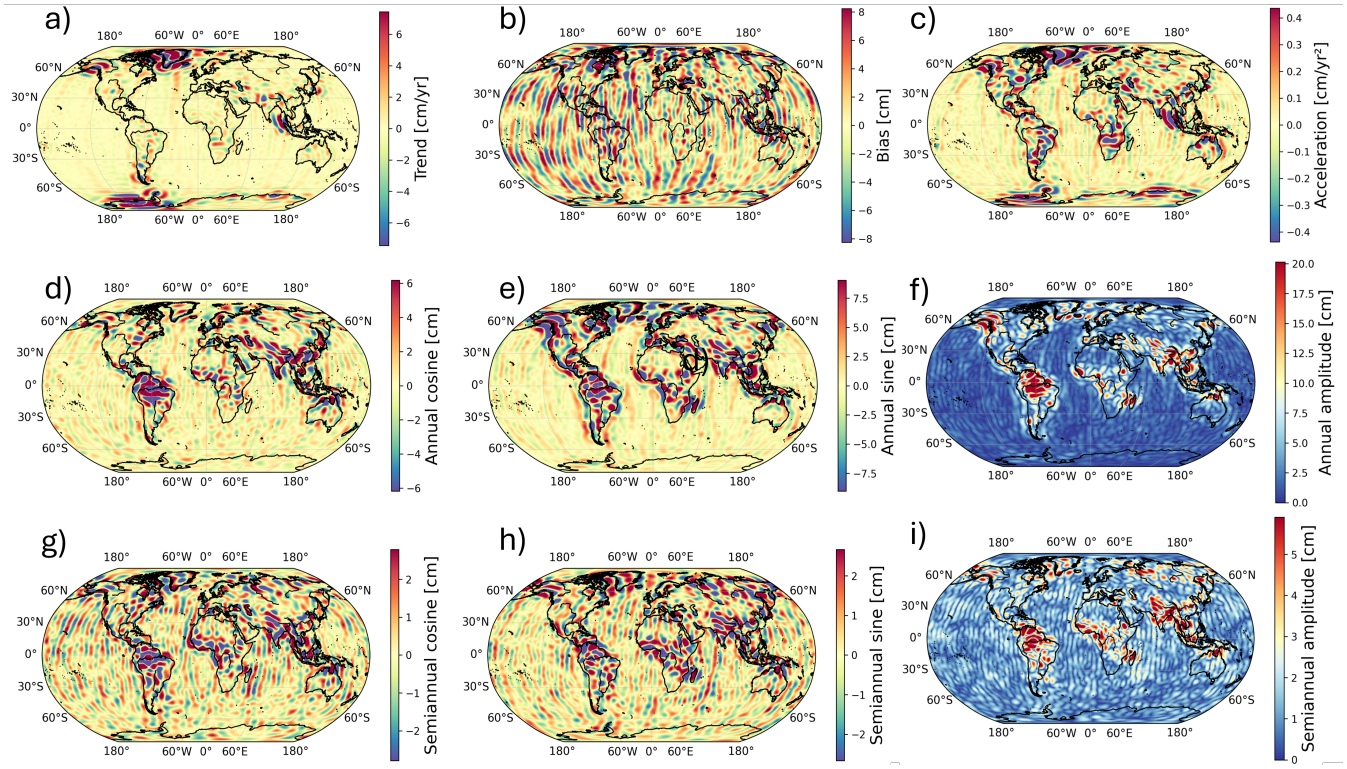


Figure 11. Climatological fitted parameters (referenced to epoch 2008.0) of the leakage correction derived following the method of Dobslaw et al. (2020), based on DDK3 filtered Level-2 solutions (degree and order 2–60). Shown are (a) linear trend, (b) bias, and (c) acceleration of the leakage correction model. The annual leakage signal is represented by (d) cosine, (e) sine, and (f) amplitude term, while the semiannual leakage signal is shown by (g) cosine, (h) sine, and (i) amplitude term.

and the ensemble solution uncertainty, respectively. Panels (c) and (d) display the RMS of the climatologically reconstructed signal and its residuals, noting that the reconstruction does not include aliasing tidal constituents (S2, P1, S1, and R3). Panels (e) and (f) illustrate the combined SLR-derived and degree-1 contribution and its associated uncertainty, while panels (g) and (h) present the leakage correction and its associated uncertainty.

The ensemble mean signal RMS (Figure 13a) has a global mean of 6.35 cm, representing the magnitude of temporal mass variability resolved by GRACE and GRACE FO. The climatologically reconstructed signal (Figure 13c) shows a slightly smaller global mean RMS of 5.68 cm. This confirms that the fitted climatological model captures most ($\sim 89\%$) of the temporal variability. The remaining difference reflects contributions not represented by the climatology, including noise, particularly visible over the oceans in Figure 13a, as well as episodic or extreme events that deviate from the assumed climatological function. For reference, when the aliasing tidal constituent S2 and the signals at aliasing frequencies related to P1, S1, and R3 (see Appendix C4) are included in the reconstruction, the global mean temporal RMS amounts to 5.71 cm (90%). This implies that unresolved tidal aliasing accounts for approximately 0.08 cm (or $1-2\%$) of the total RMS difference between the ensemble

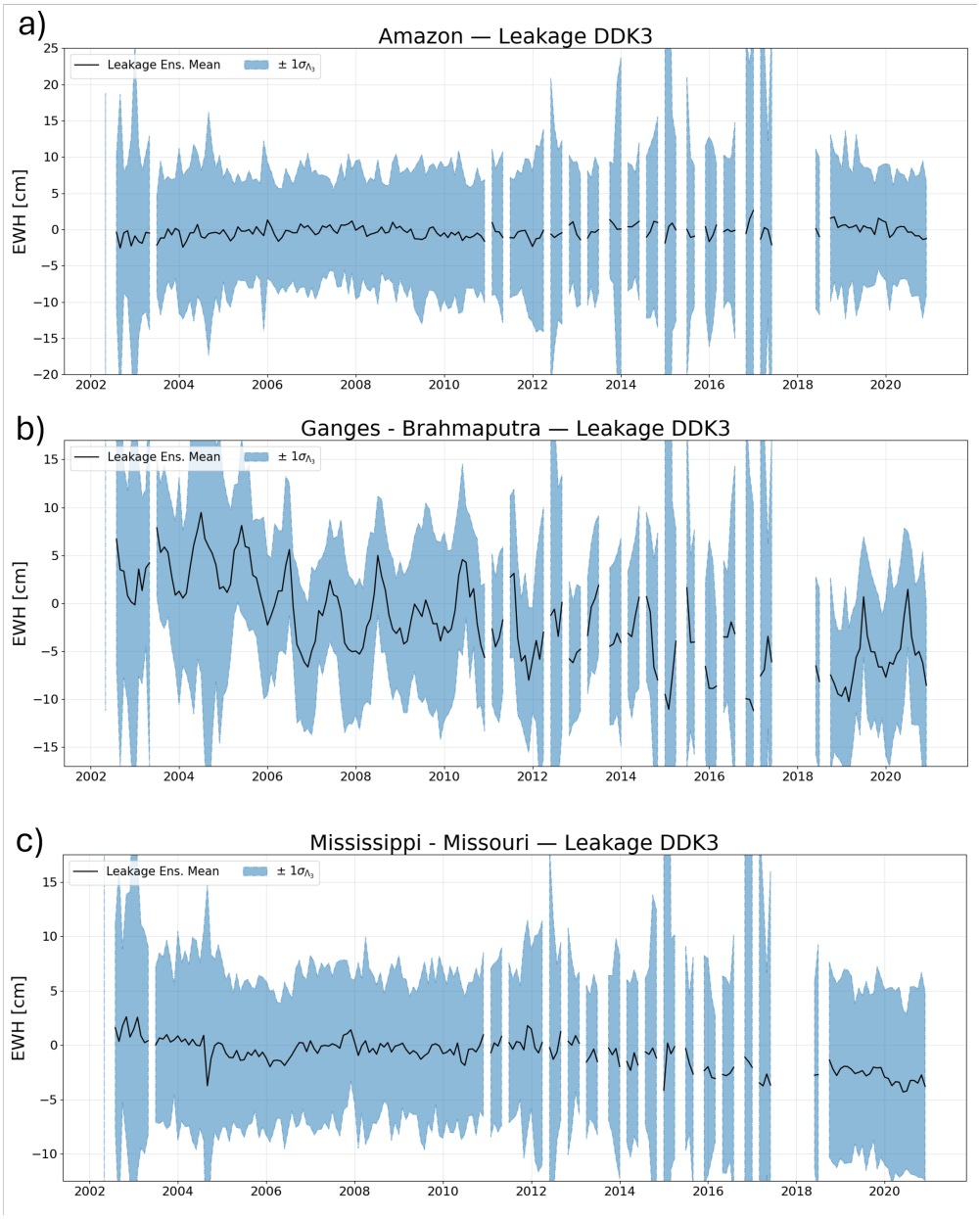


Figure 12. Basin averaged leakage correction using the method by Dobslaw et al. (2020) time series for major river basins based on DDK3 filtered Level-2 solutions (degree and order 2–60): (a) Amazon, (b) Ganges–Brahmaputra, and (c) Mississippi–Missouri. Shown are the basin mean leakage correction signals together with their associated uncertainty envelopes as $\pm 1\sigma$. A 1σ representation is used here for visual clarity, as the corresponding 2σ envelopes would obscure the leakage correction signal.

mean signal and the climatological reconstruction. The remaining discrepancy is therefore primarily attributable to residual noise and non-climatological variability, which can be observed in Figure 13d. This discrepancy is therefore primarily attributable to residual noise and non-climatological variability, as illustrated in Figure 13d, which shows a global mean RMS of 2.31 cm. Elevated values are observed in regions of strong hydrological variability, such as the Amazon, central Africa, Mississippi, and Ganges–Brahmaputra basins, as well as over Greenland and Antarctica, where they are associated with pronounced melt events (e.g. the summer of 2012; Velicogna et al. (2014)).

Among the uncertainty components, the ensemble uncertainty RMS (Figure 13b) reaches a global mean of 1.70 cm, representing the dominant global uncertainty source in this comparison. Spatially, remnants of north–south striping are still visible, with local magnitudes exceeding 3 cm. Elevated values are also apparent in regions where background ocean tide models differ more strongly between processing centres, for example along the western coast of Antarctica (up to ~ 3 cm) and along the western and northern coasts of Australia (~ 2 cm). Away from these regions, ensemble uncertainty values tend to be closer to the global mean.

The combined SLR-derived and degree-1 contribution (Figure 13e) exhibits a global mean RMS of 2.04 cm. Spatially, the signal is predominantly concentrated in the Northern Hemisphere, where local RMS values reach approximately 5 cm, but notable contributions are also present in the Southern Hemisphere, with amplitudes of around 2.5 cm. The uncertainty associated with this combined component (Figure 13f) is comparatively small, with a global mean RMS of only 0.38 cm. As expected, higher uncertainties are observed in both polar regions ($\sim$0.4–0.6 cm), while faint zonal (latitude-aligned) stripes reflect residual low-degree structure from the former $\bar{C}_{2,0}$ and $\bar{C}_{3,0}$ coefficients, with local uncertainties ranging from approximately 0.2 cm in the low-uncertainty bands to 0.4 cm between them.

The leakage correction (Figure 13g) exhibits a global mean RMS of 16.26 cm, highlighting its substantial magnitude relative to the DDK3-filtered signal (approximately 2.5–3 times larger). Highly localised signals, with amplitudes ranging from 15 cm to over 25 cm, are observed in regions of strong variability, including land hydrology hotspots, the central Greenland ice sheet (see the central leakage anomaly), and coastal regions worldwide.

The associated uncertainty of the leakage correction (Figure 13h) is also significant, with a global mean RMS of 11.01 cm. Spatially, it resembles the ensemble solution uncertainty (Figure 13b), exhibiting pronounced north–south stripes with values of 7–15 cm, but it also shows elevated uncertainty in the western Antarctic coast (10–15 cm) and the interior of Greenland (approximately 10–12 cm). The magnitude and spatial patterns of both the leakage correction and its uncertainty underline the need for caution when interpreting these fields in quantitative analyses.

Overall, the global RMS diagnostics confirm that, at the global scale, the ensemble uncertainty constitutes the largest uncertainty component, followed by AOD1B (see Figure 6 in Section 6.1.1), and the combined SLR-based and degree-1 uncertainties contribute at the sub-centimetre level.

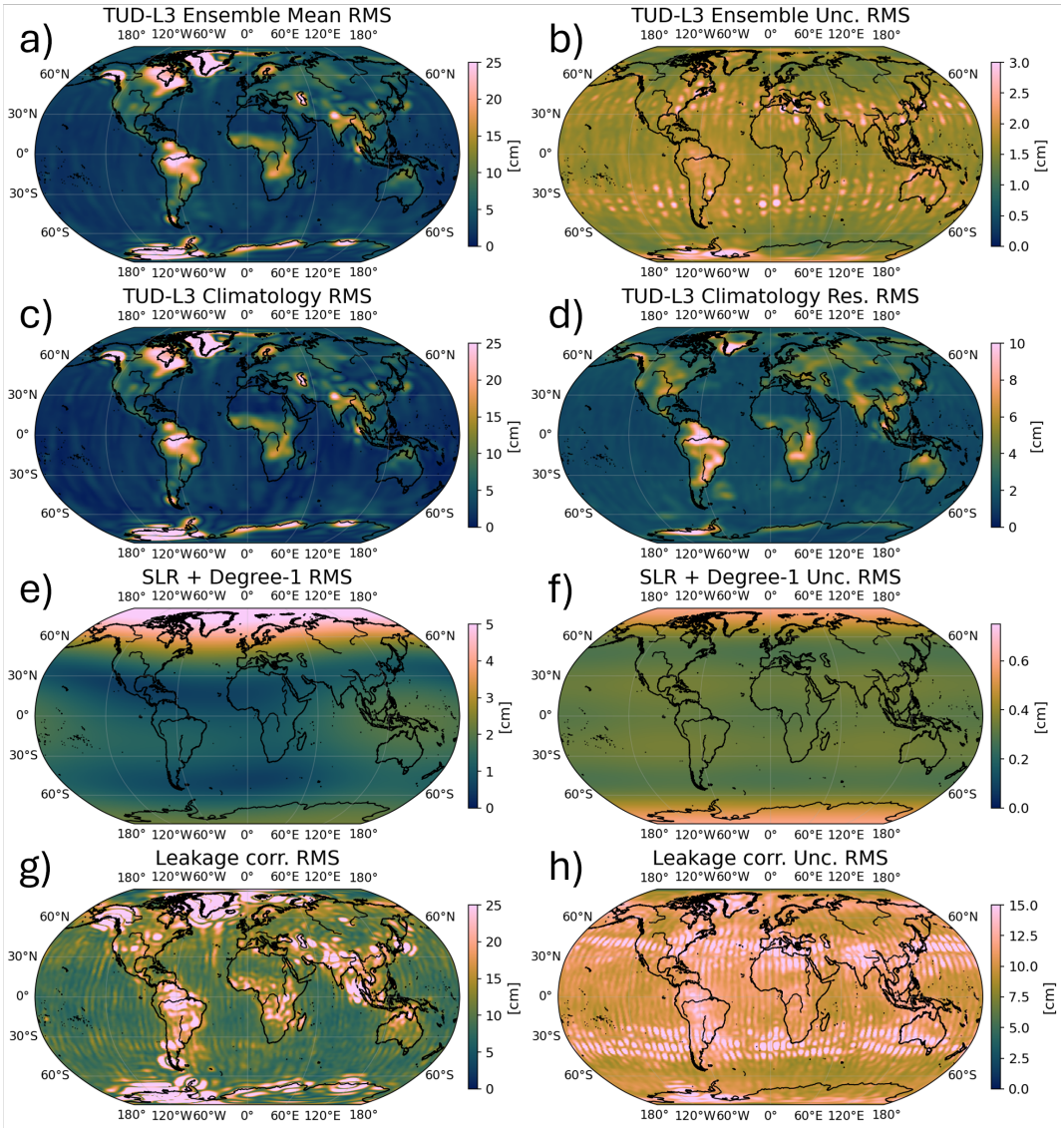


Figure 13. Global distribution of temporal RMS derived from DDK3-filtered Level-2 solutions (degree/order 2–60). Panels show the RMS of (a) the ensemble-mean EWH signal (global mean RMS: 6.36 cm), (b) the ensemble solution uncertainty (1.70 cm), (c) the climatologically reconstructed EWH signal (5.68 cm), (d) the climatological residuals (2.31 cm), (e) the SLR ($\bar{C}_{2,0}$ and $\bar{C}_{3,0}$) and degree-1 contribution (2.04 cm), (f) its associated uncertainty (0.38 cm), (g) the leakage correction (16.25 cm), and (h) its associated uncertainty (11.01 cm). Values in parentheses indicate the global mean RMS for each panel. All values are expressed in centimetres of equivalent water height (cm EWH).

7 Conclusions

In this paper, we present the construction and release of **TUD-L3-EWH_UNC-GRACE**, a globally gridded Level-3 GRACE and GRACE-FO EWH dataset with explicitly quantified uncertainty components. The dataset preserves the original mass anomaly content and provides separate gridded estimates of uncertainty arising from differences between processing centres, background model errors, low-degree coefficient replacement, filtering, and GIA modelling. The ensemble-mean signal and the associated ensemble uncertainty are computed using time-dependent weights based on the inverse squared open-ocean RMS of each solution. This weighting scheme reduces the influence of noisier solutions and minimises the overall noise level in the combined product.

A central feature of the product is the explicit separation of individual uncertainty components, provided in gridded form and for multiple DDK filter levels. This enables users to assess how different error sources contribute to the total uncertainty at basin, regional, or grid scale, and to construct application-specific uncertainty estimates rather than relying on a single aggregated error metric. Notwithstanding, we also provide the aggregate uncertainty and the ensemble mean corrected for $\bar{C}_{2,0}$ and $\bar{C}_{3,0}$ from SLR, geocenter motion, GIA ensemble mean, and ocean tidal aliasing, ready to be used directly. This is particularly relevant for hydrological data assimilation studies, where spatially resolved observation error estimates are required to properly weight GRACE-derived mass anomalies within land surface or groundwater models. The consistency and practical relevance of this framework are demonstrated through representative applications in hydrology, glaciology, and ocean circulation, where the relative importance of the different uncertainty components is evaluated in realistic use cases.

Analysis of the global fields reveals a hierarchy among uncertainty sources. Ensemble variability across processing centres dominates in most regions, particularly where solutions disagree, such as along coasts (reflecting differences in ocean tide models) and in north–south stripes (propagated noise patterns). AOD1B-related uncertainties follow, contributing notably to the global variance, while uncertainties associated with low-degree coefficient replacement and degree-1 geocentre corrections remain generally minor. GIA-related uncertainties, strongest in polar regions, correspond to long-term trends that propagate through the time series and across latitudes, impacting non-polar geophysical signals, including hydrological mass variations, as confirmed in the literature. In high-latitude hydrological basins such as the Mississippi and Mackenzie, GIA uncertainties can substantially influence both trend and variability, in some cases dominating the inferred mass change.

In addition to the main uncertainty product, several ancillary datasets are provided. These include **TUD-L3-EWH_UNC-GRACE_noSLR**, in which low-degree coefficients are not replaced by SLR solutions, as well as climatological products describing fitted signal and leakage components, released as **TUD-L3-EWH_CLIM-GRACE**, **TUD-L3-EWH_CLIM_CORR-GRACE** and **TUD-L3-EWH_CLIM_LEAKAGE-GRACE**. Together, these ancillary products support sensitivity analyses of low-degree replacement using SLR, climatological fitting, and leakage correction.

Rather than prescribing a single error model, **TUD-L3-EWH_UNC-GRACE** is designed to make the transition from Level-2 spherical harmonic solutions to gridded EWH fields explicit in terms of uncertainty. The dataset exposes how individual error sources propagate at the Level-3 stage. In this way, it provides a transparent bridge between monthly spherical harmonic coefficients and geophysical applications that require spatially resolved, traceable uncertainty information.

8 Data availability

The **TUD-L3-EWH_UNC-GRACE** dataset is publicly available at http://doi.org/10.4121/4fc748e8-01c7-4f06-87da-653937b078f7 (Cuadrat-Grzybowski et al., 2026) in CF-compliant NetCDF format, and is also distributed through the TUDelft GRACE-Cube portal (https://grace-cube.lr.tudelft.nl/). A simple Python script is provided in the accompanying README file to facilitate opening the NetCDF files, reconstructing the climatological signal, and optionally removing tidal aliasing components. Lastly, several heatmaps use the Scientific Colour Maps of Crameri et al. (2020).

Disclosure statement

The authors report there are no competing interests to declare.

AI disclosure statement

The authors used Grammarly and ChatGPT (OpenAI) solely for grammar checking and language rephrasing. No AI tools were used for scientific analysis, interpretation of results, or generation of original research content.

Acknowledgements

We thank Jose van den IJssel and Frederik Jacobs (TU Delft) for valuable discussions that helped shape the conceptual and methodological aspects of this work.

Notes on Contributors

Michal Cuadrat-Grzybowski is a PhD researcher in space gravimetry at Delft University of Technology, within the Department of Space Engineering at the Faculty of Aerospace Engineering. His research focuses on high-frequency mass change modelling using GRACE and GRACE-FO satellite gravimetry data. He works on developing and analysing Level-1B and Level-2 based approaches to improve the temporal resolution of terrestrial water storage and mass redistribution signals, with a particular emphasis on uncertainty characterisation and the interpretation of post-fit residuals in gravity field recovery.

Pieter N. A. M. Visser is a Full Professor at Delft University of Technology and Head of the Section Astrodynamics & Space Missions at the Faculty of Aerospace Engineering. His research and teaching focus on celestial mechanics and space geodesy, with particular emphasis on precise orbit determination (POD), thermosphere density retrieval from satellite dynamics, and gravity field recovery from space-borne observations. He has made substantial contributions to satellite geodesy and gravity field determination, with a strong focus on exploiting missions such as GRACE and GRACE-FO to improve understanding of mass transport processes within the Earth system.

João de Teixeira da Encarnação is an Assistant Professor at Delft University of Technology in the Department of Space Engineering, Faculty of Aerospace Engineering. His research focuses on measuring Earth's gravity field variations using satellites. With a background in Aerospace Engineering, he works on space accelerometry, estimation theory, and satellite data processing. His main objective is to develop data processing and modelling strategies that maximise the temporal resolution of gravimetric data collected by low-Earth-orbit satellites, as well as to explore the use of small satellite missions for gravimetric and thermospheric applications.

References

Ablain, M., Meyssignac, B., Zawadzki, L., Jugier, R., Ribes, A., Spada, G., Benveniste, J., Cazenave, A., & Picot, N. (2019). Uncertainty in satellite estimates of global mean sea-level changes, trend and acceleration. *Earth System Science Data*, *11*(3), 1189–1202. https://doi.org/10.5194/essd-11-1189-2019

Bagge, M., Klemann, V., Dill, R., & Dobslaw, H. (2023). *Present-day gravity changes induced by glacial isostatic adjustment from ensemble simulations with 3d earth structures*. GFZ Data Services. https://doi.org/10.5880/GFZ.1.3.2023.002

Bettadpur, S. (2018a). *Gravity Recovery and Climate Experiment Level-2 gravity field product user handbook*. Center for Space Research, The University of Texas at Austin. https://archive.podaac.earthdata.nasa.gov/podaac-ops-cumulus-docs/grace/open/docs/L2-UserHandbook_v4.0.pdf

Bettadpur, S. (2018b). *Gravity Recovery and Climate Experiment: UTCSR Level-2 processing standards document (revision 5.0, April 18, 2018) for Level-2 product release 0006* (Technical Report) (UTCSR Document, Rev 5.0). Center for Space Research, The University of Texas at Austin. https://icgem.gfz-potsdam.de/docs/GRACE_CSR_L2_Processing_Standards_Document_for_RL06.pdf

Bettadpur, S. V. (2018). *GRACE Level-2 processing standards document* [Rev 5.0 Apr 18, 2018, For Level-2 Product Release 0006]. Center for Space Research, The University of Texas at Austin. https://podaac-tools.jpl.nasa.gov/drive/files/allData/grace/docs/L2-CSR006_ProcStd_v5.0.pdf

Blazquez, A., Meyssignac, B., Lemoine, J., Berthier, E., Ribes, A., & Cazenave, A. (2018). Exploring the uncertainty in GRACE estimates of the mass redistributions at the Earth surface: Implications for the global water and sea level budgets. *Geophysical Journal International*, *215*(1), 415–430. https://doi.org/10.1093/gji/ggy293

Boergens, E. (2021). Python package regional tws uncertainty. https://doi.org/10.5880/GFZ.1.3.2021.005

Boergens, E., Kvas, A., Eicker, A., Dobslaw, H., Schawohl, L., Dahle, C., Murböck, M., & Flechtner, F. (2022). Uncertainties of GRACE-based terrestrial water storage anomalies for arbitrary averaging regions. *Journal of Geophysical Research: Solid Earth*, *127*(2), e2021JB022081. https://doi.org/10.1029/2021JB022081

Caron, L., Ivins, E. R., Larour, E., Adhikari, S., Nilsson, J., & Blewitt, G. (2018). GIA model statistics for GRACE hydrology, cryosphere, and ocean science. *Geophysical Research Letters*, *45*(5), 2203–2212. https://doi.org/10.1002/2017GL076644

Carrere, L., Lyard, F., Cancet, M., Allain, D., Dabat, M.-L., Fouchet, E., & Picot, N. (2022). A new barotropic tide model for global ocean: FES2022. https://doi.org/10.24400/527896/a03-2022.3287

Carrère, L., Lyard, F., Cancet, M., Guillot, A., Picot, N., et al. (2016). FES 2014, a new tidal model—validation results and perspectives for improvements. *Proceedings of the ESA Living Planet Symposium*, 9–13.

Case, K., Kruizinga, G., & Wu, S.-C. (2010). GRACE Level 1B Data Product User Handbook. https://podaac-tools.jpl.nasa.gov/drive/files/allData/grace/docs/Handbook_1B_v1.3.pdf

Chen, J., Tapley, B., Tamisiea, M. E., Save, H., Wilson, C., Bettadpur, S., & Seo, K.-W. (2021). Error assessment of GRACE and GRACE Follow-On mass change. *Journal of Geophysical Research: Solid Earth*, *126*(9), e2021JB022124. https://doi.org/10.1029/2021JB022124

Chen, Q., Shen, Z., Sun, Y., Wu, C., & Zhang, X. (2023). Tongji-GRACE2022: New global temporal Earth's gravity field models derived from K-band and LRI inter-satellite range-rate data. *XXVIII General Assembly of the International Union of Geodesy and Geophysics (IUGG)*. https://doi.org/10.57757/IUGG23-0878

Cheng, M., & Ries, J. (2023). C20 and C30 variations from SLR for GRACE/GRACE-FO science applications. *Journal of Geophysical Research: Solid Earth*, *128*(2), e2022JB025459. https://doi.org/10.1029/2022JB025459

Copernicus Climate Change Service. (2026). Terrestrial water storage anomaly data from 2002 to present derived from satellite gravimetry observations. https://doi.org/10.24381/c6f5085a

Crameri, F., Shephard, G. E., & Heron, P. J. (2020). The misuse of colour in science communication. *Nature Communications*, *11*, 5444. https://doi.org/10.1038/s41467-020-19160-7

Cuadrat-Grzybowski, M., Teixeira da Encarnacao, J. G., & Visser, P. N. A. M. (2025). Potential of Ka-band range rate post-fit residuals for high-frequency mass change applications. *Journal of Geophysical Research: Solid Earth*, *130*(12). https://doi.org/10.1029/2025JB031615

Cuadrat-Grzybowski, M., Visser, P., & De Teixeira da Encarnacao, J. (2026). *TUD-L3-EWH_UNC-GRACE: Global 0.5°x0.5° monthly equivalent water height user-friendly dataset with comprehensive uncertainty decomposition (ensemble solution spread, AOD1B uncertainty, DDK leakage error, low-degree coefficient treatment, and GIA ensemble error)* (dataset; Version 6). dataset. 4TU.ResearchData. https://doi.org/10.4121/4fc748e8-01c7-4f06-87da-653937b078f7

Dahle, C., Boergens, E., Sasgen, I., Döhne, T., Reißland, S., Dobslaw, H., Klemann, V., Murböck, M., König, R., Dill, R., Sips, M., Sylla, U., Groh, A., Horwath, M., & Flechtner, F. (2025). GravIS: Mass anomaly products from satellite gravimetry. *Earth System Science Data*, *17*(2), 611–631. https://doi.org/10.5194/essd-17-611-2025

Dahle, C., Murböck, M., Flechtner, F., Dobslaw, H., Michalak, G., Neumayer, K. H., Abrykosov, O., Reinhold, A., König, R., Sulzbach, R., & Förste, C. (2019). The GFZ GRACE RL06 monthly gravity field time series: processing details and quality assessment. *Remote Sensing*, *11*(18). https://doi.org/10.3390/rs11182116

Darbeheshti, N., Lasser, M., Meyer, U., Arnold, D., & Jäggi, A. (2023). *AIUB-G3P GRACE monthly gravity field solutions*. GFZ Data Services. https://doi.org/10.5880/icgem.2023.001

Ditmar, P. (2018). Conversion of time-varying Stokes coefficients into mass anomalies at the Earth's surface considering the Earth's oblateness. *Journal of Geodesy*, *92*, 1401–1412. https://doi.org/10.1007/s00190-018-1128-0

Dobslaw, H., Bergmann-Wolf, I., Dill, R., Poropat, L., Thomas, M., Dahle, C., Esselborn, S., König, R., & Flechtner, F. (2017). A new high-resolution model of non-tidal atmosphere and ocean mass variability for de-aliasing of satellite gravity observations: AOD1B RL06. *Geophysical Journal International*, *211*(1), 263–269. https://doi.org/10.1093/gji/ggx302

Dobslaw, H., Bergmann-Wolf, I., Forootan, E., et al. (2016). Modeling of present-day atmosphere and ocean non-tidal de-aliasing errors for future gravity mission simulations. *Journal of Geodesy*, *90*, 423–436. https://doi.org/10.1007/s00190-015-0884-3

Dobslaw, H., Dill, R., Bagge, M., Klemann, V., Boergens, E., Thomas, M., Dahle, C., & Flechtner, F. (2020). Gravitationally consistent mean barystatic sea level rise from leakage-corrected monthly GRACE data [e2020JB020923 10.1029/2020JB020923]. *Journal of Geophysical Research: Solid Earth*, *125*(11), e2020JB020923. https://doi.org/10.1029/2020JB020923

Dobslaw, H., Dill, R., & Dahle, C. (2018). *GRACE geopotential GAC coefficients GFZ RL06*. GFZ Data Services. https://doi.org/10.5880/GFZ.GRACE_06_GAC

Eicker, A., Schawohl, L., Middendorf, K., Bagge, M., Jensen, L., & Dobslaw, H. (2024). Influence of GIA uncertainty on climate model evaluation with GRACE/GRACE-FO satellite gravimetry data. *Journal of Geophysical Research: Solid Earth*, *129*(5), e2023JB027769. https://doi.org/10.1029/2023JB027769

Gałdyn, F., & Sośnica, K. (2024). Impact of the combination and replacement of SLR-based low-degree gravity field coefficients in GRACE solutions. *Progress in Earth and Planetary Science*, *11*(1), 7. https://doi.org/10.1186/s40645-024-00608-z

Gao, S., Hao, W., Fan, Y., Li, F., & Wang, J. (2023). A multi-source GRACE fusion solution via uncertainty quantification of GRACE-derived terrestrial water storage (TWS) change. *Journal of Geophysical Research: Solid Earth*, *128*(11), e2023JB026908. https://doi.org/10.1029/2023JB026908

Ghobadi-Far, K., Han, S. C., McCullough, C. M., Wiese, D. N., Ray, R. D., Sauber, J., Shihora, L., & Dobslaw, H. (2022). Along-orbit analysis of GRACE Follow-On inter-satellite laser ranging measurements for sub-monthly surface mass variations. *Journal of Geophysical Research: Solid Earth*, *127*. https://doi.org/10.1029/2021JB022983

Groh, A., & Horwath, M. (2021). Antarctic ice mass change products from GRACE/GRACE-FO using tailored sensitivity kernels. *Remote Sensing*, *13*(9). https://doi.org/10.3390/rs13091736

Güntner, A., Sharifi, E., Haas, J., Boergens, E., Dahle, C., Dobslaw, H., Dorigo, W., Dussailant, I., Flechtner, F., Jäggi, A., Kosmale, M., Luojus, K., Mayer-Gürr, T., Meyer, U., Preimesberger, W., Ruz Vargas, C., & Zemp, M. (2024). Global Gravity-based Groundwater Product (G3P) (Version 1.12). https://doi.org/10.5880/G3P.2024.001

Han, S.-C., Ray, R., & Hughes, C. (2014). High-frequency (20–60 days) ocean mass variation over the Argentine Basin observed from GRACE. *Proceedings of the GRACE Science Team Meeting*. https://www.gfz-potsdam.de/en/section/global-geomonitoring-and-gravity-field/projects/gravity-recovery-and-climate-experiment-follow-on-grace-fo-mission/gstm/gstm-2014/

Han, S.-C., Ray, R. D., & Luthcke, S. B. (2010). One centimeter-level observations of diurnal ocean tides from global monthly mean time-variable gravity fields. *Journal of Geodesy*, *84*, 715–729. https://doi.org/10.1007/s00190-010-0405-3

Hart-Davis, M. G., Piccioni, G., Dettmering, D., Schwatke, C., Passaro, M., & Seitz, F. (2021). EOT20: A global ocean tide model from multi-mission satellite altimetry. *Earth System Science Data*, *13*(8), 3869–3884. https://doi.org/10.5194/essd-13-3869-2021

Ince, E. S., Barthelmes, F., Reißland, S., Elger, K., Förste, C., Flechtner, F., & Schuh, H. (2019). ICGEM – 15 years of successful collection and distribution of global gravitational models, associated services, and future plans. *Earth Syst. Sci. Data*, *11*(2), 647–674. https://doi.org/10.5194/essd-11-647-2019

Jäggi, A., Meyer, U., Lasser, M., Jenny, B., Lopez, T., Flechtner, F., Dahle, C., Förste, C., Mayer-Gürr, T., Kvas, A., Lemoine, J.-M., Bourgogne, S., Weigelt, M., & Groh, A. (2022). International Combination Service for Time-Variable Gravity Fields (COST-G). In J. T. Freymueller & L. Sánchez (Eds.), *Beyond 100: The next century in geodesy* (pp. 57–65). Springer International Publishing.

Jean, Y., Meyer, U., & Jäggi, A. (2018). Combination of GRACE monthly gravity field solutions from different processing strategies. *Journal of Geodesy*, *92*(11), 1313–1328. https://doi.org/10.1007/s00190-018-1123-5

Koch, I., Duwe, M., & Flury, J. (2024). Residual and unmodeled ocean tide signal from 20+ years of GRACE and GRACE-FO global gravity field models. *Journal of Geophysical Research: Solid Earth*, *129*(9), e2024JB029345. https://doi.org/10.1029/2024JB029345

Koch, I., Flury, J., Naeimi, M., & Shabanloui, A. (2022). LUH-GRACE2018: A new time series of monthly gravity field solutions from GRACE. In J. T. Freymueller & L. Sánchez (Eds.), *Beyond 100: The next century in geodesy* (pp. 67–75). Springer International Publishing.

Koch, I., Duwe, M., Flury, J., & Shabanloui, A. (2021). Earth's time-variable gravity from GRACE Follow-On K-band range-rates and pseudo-observed orbits. *Remote Sensing*, *13*(9), 1766. https://doi.org/10.3390/rs13091766

König, R., Schreiner, P., & Dahle, C. (2019). Monthly estimates of C(2,0) generated by GFZ from SLR satellites based on GFZ GRACE/GRACE-FO RL06 background models. *GFZ Data Services*. https://doi.org/10.5880/GFZ.GRAVIS_06_C20_SLR

Kusche, J., Schmidt, R., Petrovic, S., & Rietbroek, R. (2009). Decorrelated GRACE time-variable gravity solutions by GFZ, and their validation using a hydrological model. *Journal of Geodesy*, *83*, 903–913. https://doi.org/10.1007/s00190-009-0308-3

Kvas, A., Behzadpour, S., Ellmer, M., Klinger, B., Strasser, S., Zehentner, N., & Mayer-Gürr, T. (2019). ITSG-Grace2018: Overview and evaluation of a new GRACE-only gravity field time series. *Journal of Geophysical Research: Solid Earth*, *124*, 9332–9344. https://doi.org/10.1029/2019JB017415

Kvas, A., & Mayer-Gürr, T. (2019). GRACE gravity field recovery with background model uncertainties. *Journal of Geodesy*, *93*(12), 2543–2552. https://doi.org/10.1007/s00190-019-01314-1

Landerer, F. W., Flechtner, F. M., Save, H., Webb, F. H., Bandikova, T., Bertiger, W. I., Bettadpur, S. V., Byun, S. H., Dahle, C., Dobslaw, H., Fahnestock, E., Harvey, N., Kang, Z., Kruizinga, G. L. H., Loomis, B. D., McCullough, C., Murböck, M., Nagel, P., Paik, M., … Yuan, D.-N. (2020). Extending the global mass change data record: GRACE Follow-On instrument and science data performance. *Geophysical Research Letters*, *47*(12), e2020GL088306. https://doi.org/10.1029/2020GL088306

Lasser, M., Meyer, U., Arnold, D., & Jäggi, A. (2023). *AIUB-GRACE-FO-operational: Operational GRACE Follow-On monthly gravity field solutions - release 02*. GFZ Data Services. https://doi.org/10.5880/icgem.2023.004

Lemoine, J.-M., & Bourgogne, S. RL05 monthly and 10-day gravity field solutions from CNES/GRGS. In: In *Gstm2020-51*. 2020, October. https://doi.org/10.5194/gstm2020-51

Li, Z., Zhang, Z., & Wang, H. (2022). On tide aliasing in GRACE time-variable gravity observations. *Remote Sensing*, *14*(21). https://doi.org/10.3390/rs14215403

Liu, S., Yang, F., & Forootan, E. (2025). SAGEA: A toolbox for comprehensive error assessment of GRACE and GRACE-FO based mass changes. *Computers & Geosciences*, *196*, 105825. https://doi.org/10.1016/j.cageo.2024.105825

Liu, W., & Sneeuw, N. (2021). Aliasing of ocean tides in satellite gravimetry: a two-step mechanism. *Journal of Geodesy*, *95*, 134. https://doi.org/10.1007/s00190-021-01586-6

Loomis, B. D., Luthcke, S. B., & Sabaka, T. J. (2019). Regularization and error characterization of GRACE mascons. *Journal of Geodesy*, *93*, 1381–1398. https://doi.org/10.1007/s00190-019-01252-y

Loomis, B. D., & Rachlin, K. E. (2023). NASA GSFC SLR C20 and C30 solutions (TN-14), Version 3 [SLR-derived C_{20} and C_{30} values for GRACE/GRACE-FO gravity field replacement. Data span 4 Apr 2002–1 Sep 2025.]. https://doi.org/10.1029/2019GL085488

Loomis, B. D., Rachlin, K. E., Wiese, D. N., Landerer, F. W., & Luthcke, S. B. (2020). Replacing GRACE/GRACE-FO C30 with satellite laser ranging: impacts on Antarctic ice sheet mass change. *Geophysical Research Letters*, *47*(3), e2019GL085488. https://doi.org/10.1029/2019GL085488

Lyard, F. H., Allain, D. J., Cancet, M., Carrère, L., & Picot, N. (2021). FES2014 global ocean tide atlas: design and performance. *Ocean Science*, *17*(3), 615–649. https://doi.org/10.5194/os-17-615-2021

Mayer-Gürr, T., Behzadpur, S., Ellmer, M., Kvas, A., Klinger, B., Strasser, S., & Zehentner, N. (2018). ITSG-Grace2018 - monthly, daily and static gravity field solutions from GRACE. *GFZ Data Services*. https://doi.org/10.5880/ICGEM.2018.003

Mei, C., Sun, Y., & Li, Y. (2025). Low-degree spherical harmonic coefficients for GRACE/GRACE-FO gravity field models from the fingerprint approach. *Journal of Geophysical Research: Solid Earth*, *130*(7), e2024JB029792. https://doi.org/10.1029/2024JB029792

Moore, P., & King, M. A. (2008). Antarctic ice mass balance estimates from GRACE: Tidal aliasing effects. *Journal of Geophysical Research: Earth Surface*, *113*, F02017. https://doi.org/10.1029/2007JF000871

Nie, Y., Chen, J., Peng, D., & Li, J. (2025). Inferring long-term geocenter motion from low-degree gravity field [e2024JB030327 2024JB030327]. *Journal of Geophysical Research: Solid Earth*, *130*(8), e2024JB030327. https://doi.org/10.1029/2024JB030327

Peltier, W. R., Argus, D. F., & Drummond, R. (2018). Comment on "an assessment of the ice-6g_c (vm5a) glacial isostatic adjustment model" by purcell et al. *Journal of Geophysical Research: Solid Earth*, *123*, 2019–2018. https://doi.org/10.1002/2016JB013844

Petit, G., & Luzum, B. (Eds.). (2010). *IERS conventions (2010)*. International Earth Rotation; Reference Systems Service (IERS). https://iers-conventions.obspm.fr/content/tn36.pdf

Qian, N., Chang, G., Ditmar, P., Gao, J., & Wei, Z. (2022). Sparse DDK: A data-driven decorrelation filter for GRACE level-2 products. *Remote Sensing*, *14*(12). https://doi.org/10.3390/rs14122810

Ray, R. D. (2013). Precise comparisons of bottom-pressure and altimetric ocean tides. *Journal of Geophysical Research: Oceans*, *118*(9), 4570–4584. https://doi.org/10.1002/jgrc.20336

Ray, R. D., & Luthcke, S. B. (2006). Tide model errors and GRACE gravimetry: towards a more realistic assessment. *Geophysical Journal International*, *167*(3), 1055–1059. https://doi.org/10.1111/j.1365-246X.2006.03229.x

Ray, R. D. (2025). *Documentation for Goddard ocean tide solution GOT5: Global tides from multi-mission satellite altimetry* (Technical Memorandum). NASA Goddard Space Flight Center. https://science.gsfc.nasa.gov/sed/content/uploadFiles/publication_files/GOT5-TechMemo.pdf

Retegui-Schiettekatte, L., Schumacher, M., Madsen, H., & Forootan, E. (2025). Assessing daily GRACE data assimilation during flood events of the Brahmaputra river basin. *Science of The Total Environment*, *975*, 179181. https://doi.org/10.1016/j.scitotenv.2025.179181

Ries, J., Bettadpur, S., Eanes, R., Kang, Z., Ko, U., McCullough, C., Nagel, P., Pie, N., Poole, S., Richter, T., Save, H., & Tapley, B. (2016). The combination global gravity model GGM05C. https://hdl.handle.net/2152/74341

Savcenko, R., & Bosch, W. (2012). *EOT11a-empirical ocean tide model from multi-mission satellite altimetry* (tech. rep.). Deutsches Geodätisches Forschungsinstitut (DGFI). https://epic.awi.de/id/eprint/36001/1/DGFI_Report_89.pdf

Save, H., Bettadpur, S., & Tapley, B. D. (2016). High-resolution CSR GRACE RL05 mascons. *Journal of Geophysical Research: Solid Earth*, *121*(10), 7547–7569. https://doi.org/10.1002/2016JB013007

Seo, K.-W., Wilson, C. R., Han, S.-C., & Waliser, D. E. (2008). Gravity Recovery and Climate Experiment (GRACE) alias error from ocean tides. *Journal of Geophysical Research: Solid Earth*, *113*(B3), B03405. https://doi.org/10.1029/2006JB004747

Shihora, L., Liu, Z., Balidakis, K., et al. (2024). Accounting for residual errors in atmosphere–ocean background models applied in satellite gravimetry. *Journal of Geodesy*, *98*, 27. https://doi.org/10.1007/s00190-024-01832-7

Sun, Y., Riva, R., & Ditmar, P. (2016). Optimizing estimates of annual variations and trends in geocenter motion and J_2 from a combination of GRACE data and geophysical models. *Journal of Geophysical Research: Solid Earth*, *121*. https://doi.org/10.1002/2016JB013073

Swenson, S., Chambers, D., & Wahr, J. (2008). Estimating geocenter variations from a combination of GRACE and ocean model output. *Journal of Geophysical Research*, *113*(B08S10). https://doi.org/10.1029/2007JB005338

Tapley, B. D., Bettadpur, S., Watkins, M., & Reigber, C. (2004). The gravity recovery and climate experiment: Mission overview and early results. *Geophysical Research Letters*, *31*(9). https://doi.org/10.1029/2004GL019920

Tourian, M. J. (2013). *Application of Spaceborne Geodetic Sensors for Hydrology* [Doctoral dissertation, University of Stuttgart]. https://doi.org/10.18419/opus-3929

Tourian, M. J., et al. (2022). HydroSat: geometric quantities of the global water cycle from geodetic satellites. *Earth System Science Data*, *14*, 2463–2486. https://doi.org/10.5194/essd-14-2463-2022

Tourian, M. J., Reager, J. T., & Sneeuw, N. (2018). The total drainable water storage of the amazon river basin: A first estimate using GRACE. *Water Resources Research*, *54*, 3290–3312. https://doi.org/10.1029/2017WR021674

Velicogna, I., Sutterley, T. C., & van den Broeke, M. R. (2014). Regional acceleration in ice mass loss from Greenland and Antarctica using GRACE time-variable gravity data. *Geophysical Research Letters*, *41*(22), 8130–8137. https://doi.org/10.1002/2014GL061052

Volkov, D. L., & Fu, L.-L. (2008). The role of vorticity fluxes in the dynamics of the Zapiola Anticyclone. *Journal of Geophysical Research: Oceans*, *113*(C11). https://doi.org/10.1029/2008JC004841

Werth, S., Güntner, A., Schmidt, R., & Kusche, J. (2009). Evaluation of GRACE filter tools from a hydrological perspective. *Geophysical Journal International*, *179*(3), 1499–1515. https://doi.org/10.1111/j.1365-246X.2009.04355.x

Wiese, D. N., Landerer, F. W., & Watkins, M. M. (2016). Quantifying and reducing leakage errors in the JPL RL05M GRACE mascon solution. *Water Resources Research*, *52*(9), 7490–7502. https://doi.org/10.1002/2016WR019344

Wu, W.-Y., Yang, Z.-L., Zhao, L., & Lin, P. (2022). The impact of multi-sensor land data assimilation on river discharge estimation. *Remote Sensing of Environment*, *279*, 113138. https://doi.org/10.1016/j.rse.2022.113138

Yang, F., Schumacher, M., Retegui-Schiettekatte, L., van Dijk, A. I. J. M., & Forootan, E. (2025). PyGLDA: a fine-scale python-based global land data assimilation system for integrating satellite gravity data into hydrological models. *Geoscientific Model Development*, *18*(18), 6195–6217. https://doi.org/10.5194/gmd-18-6195-2025

You, W., Qian, K., Wan, X., Yu, B., Zhang, J., Pu, L., Shu, J., & Liu, C. (2025). Spatial-domain combination of GRACE monthly time-variable gravity models based on multiple weighting strategies and comparison of models' performance in the Caspian Sea. *Scientific Reports*, *15*(1), 3962. https://doi.org/10.1038/s41598-025-87922-8

Yu, Y., Chao, B. F., García-García, D., & Luo, Z. (2018). Variations of the Argentine Gyre observed in the GRACE time-variable gravity and ocean altimetry measurements. *Journal of Geophysical Research: Oceans*, *123*(8), 5375–5387. https://doi.org/10.1029/2018JC014189

Yuan, D. (2018). *Gravity Recovery and Climate Experiment: JPL Level-2 processing standards document for level-2 product release 06* (Technical Report) (JPL 327-744 (v 6.0)). Jet Propulsion Laboratory, California Institute of Technology. https://icgem.gfz-potsdam.de/docs/GRACE_JPL_L2_Processing_Standards_Document_for_RL06.pdf

Zhang, L., Shen, Y., Ji, K., & Chen, Q. (2024). Covariance matrix reconstruction of GRACE monthly solutions using common factors and individual formal errors. *IEEE Journal of Selected Topics in Applied Earth Observations and Remote Sensing*, *17*, 15567–15582. https://doi.org/10.1109/JSTARS.2024.3405560

Zhou, H., Zheng, L., Li, Y., Guo, X., Zhou, Z., & Luo, Z. (2024). HUST-Grace2024: a new GRACE-only gravity field time series based on more than 20 years of satellite geodesy data and a hybrid processing chain. *Earth System Science Data*, *16*(7), 3261–3281. https://doi.org/10.5194/essd-16-3261-2024

Zhou, H., Zheng, L., Pail, R., Liu, S., Qing, T., Yang, F., Guo, X., & Luo, Z. (2023). The impacts of reducing atmospheric and oceanic de-aliasing model error on temporal gravity field model determination. *Geophysical Journal International*, *234*(1), 210–227. https://doi.org/10.1093/gji/ggad064

Appendix A: Level-2 Spherical Harmonic Harmonisation

A1 Reference constants

Prior to the Level-2 intercomparison, all monthly spherical harmonic solutions are harmonised following the procedure of Jean et al. (2018). This ensures that differences between solutions originate from the gravity field estimates themselves rather than from differing reference conventions.

All solutions are first expressed using the common reference constants adopted by Jean et al. (2018),

$$GM_{\mathrm{ref}} = 3.986004415 \times 10^{14}\ \mathrm{m^3\,s^{-2}}, \tag{A1}$$

and,

$$R_{\mathrm{ref}} = 6\,378\,136.3\ \mathrm{m}. \tag{A2}$$

The fully-normalized spherical harmonic coefficients are rescaled according to

$$f_n = \left(\frac{GM_{\mathrm{original}}}{GM_{\mathrm{ref}}}\right)\left(\frac{R_{\mathrm{original}}}{R_{\mathrm{ref}}}\right)^n, \tag{A3}$$

where n denotes the spherical harmonic degree. Both $\bar{C}_{n,m}$ and $\bar{S}_{n,m}$ are multiplied by f_n.

A2 From zero-tide to tide-free

For products provided in the zero-tide system, the corresponding permanent solid Earth tide correction is applied to $\bar{C}_{2,0}$. Whenever the numerical value of the correction is not explicitly documented but compliance with the IERS 2010 Conventions is stated, a value of $\Delta\bar{C}^{\mathrm{s.t.}}_{2,0} = 4.1736\times10^{-9}$ is adopted, consistent with the IERS 2010 Convention. In addition, the symbol "$^{(*)}$" is used to flag cases where our analysis suggests that the stated tide system (zero-tide or tide-free) of a product is inconsistent with the inferred behaviour of $\bar{C}_{2,0}$, indicating a likely reversal of the declared convention. Table A1 summarises the reference constants and permanent tide conventions adopted by each Level-2 product.

Figure A1 presents the time series of the corrected degree-2 order-0 coefficient ($\bar{C}_{2,0}$) for all Level-2 gravity field solutions over the period 2002–2020. All products have been harmonised to a consistent tide-free reference system, including the application of permanent solid Earth tide corrections where required (Table A1). The figure allows for a direct intercomparison of temporal variability and systematic offsets between processing centres.

Overall, the different solutions exhibit broadly similar but not identical temporal evolutions of $\bar{C}_{2,0}$. While the general amplitude range is comparable across products, clear inter-solution differences are present throughout the record, with variations between solutions often exceeding the temporal variability observed in the SLR series by approximately a factor of 2–4. The SLR series itself shows a comparatively smooth and low-amplitude temporal behaviour, whereas the GRACE- and GRACE-FO-derived solutions display larger fluctuations and more pronounced differences between products.

Notably, the previously identified inconsistency in tide-system labelling is confirmed by the time series behaviour: HUST and APM-SYSU exhibit characteristics consistent with a tide-free and zero-tide configuration, respectively, contrary to their

Table A1. Reference Earth radius and permanent tide conventions of the Level-2 gravity field products used in this study. All products adopt the common reference gravitational parameter $GM_{\mathrm{ref}} = 3.986004415 \times 10^{14}$ m^3 s^{-2}. Only the permanent tide correction applied to $\Delta\bar{C}_{2,0}^{\mathrm{s.t.}}$ for conversion from the zero-tide to the tide-free system is listed. The symbol "$^{(*)}$" indicates cases where our analysis suggests that the stated tide system (zero-tide or tide-free) of the product files is inconsistent with the behaviour of the estimated $\bar{C}_{2,0}$ values, implying a likely reversal of the declared convention (e.g., zero-tide instead of tide-free, or vice versa).

Solution	R [km]	Tide system	$\Delta\bar{C}_{2,0}^{\mathrm{s.t.}}$ [-]	Source
GGM05C	6378.1363	Zero-tide	4.200×10^{-9}	Ries et al. (2016)
CSR RL06(.3)	6378.1363	Zero-tide	4.201×10^{-9}	S. V. Bettadpur (2018)
JPL RL06(.3)	6378.1363	Zero-tide	4.173×10^{-9}	Yuan (2018)
GFZ RL06(.3)	6378.13646	Tide-free	–	Dahle et al. (2019)
COST-G RL02.1	6378.1363	Tide-free	–	Jäggi et al. (2022)
ITSG-Grace2018/_op	6378.1363	Zero-tide	4.1736×10^{-9}	Mayer-Gürr et al. (2018)
Tongji-Grace2022	6378.1363	Zero-tide	4.1736×10^{-9}	Q. Chen et al. (2023)
HUST-Grace2024	6378.1363	Zero-tide$^{(*)}$	$4.1736 \times 10^{-9}(*)$	Zhou et al. (2024)
APM-SYSU	6378.1363	Tide-free$^{(*)}$	$4.1736 \times 10^{-9}(*)$	n.a.
AIUB-G3P/RL02_op	6378.1370	Tide-free	–	Darbeheshti et al. (2023) and Lasser et al. (2023)
CNES-CHOL	6378.13646	Tide-free	–	Lemoine and Bourgogne (2020)
LUH-Grace(-FO)-2020	6378.1363	Tide-free	–	Koch et al. (2022)

documented product specifications. Among the available solutions, AIUB (G3P) shows the most pronounced outliers during several periods, particularly toward the early and late GRACE record (e.g., 2003/05 and 2016/11–06/2017). However, some of these apparent deviations occur during periods with limited availability of other solutions (see 2003/06).

For the GRACE period (2002–2017), we further observe a near-constant offset between most solutions and the COST-G RL02.1 reference of approximately 4.5×10^{-10}, consistent with results obtained in Gałdyn and Sośnica (2024). A smaller but consistent offset of approximately $(1\text{–}2) \times 10^{-10}$ is also present for the Tongji-Grace2022 solution. The origin of these systematic differences cannot be uniquely identified from the present comparison. As COST-G is a combined solution, the observed offsets may partly reflect differences in tide-system definitions or their handling across the contributing analysis-centre solutions, although such effects would be expected to partly cancel during the combination. Contributions from other processing differences cannot be excluded. In contrast, the GRACE-FO period shows a markedly improved convergence between all solutions, with significantly reduced inter-product spread and no persistent offsets relative to COST-G RL02.1.

This inter-solution spread in $\bar{C}_{2,0}$ is expected to be reflected in the corresponding 'noSLR' ancillary data product as a significant source of uncertainty, particularly during the GRACE period. It should be noted, however, that the nearly constant offset of the COST-G combination relative to the SLR-replaced reference is not reflected in the uncertainty estimates, as COST-G is used only to derive the ensemble weights and not in the computation of the weighted standard deviation itself. In contrast, nearly constant offsets present in individual solutions, such as Tongji, do contribute to the 'noSLR' uncertainty estimates. Given the near-constant offsets observed in several individual solutions during the GRACE period, we recommend using the

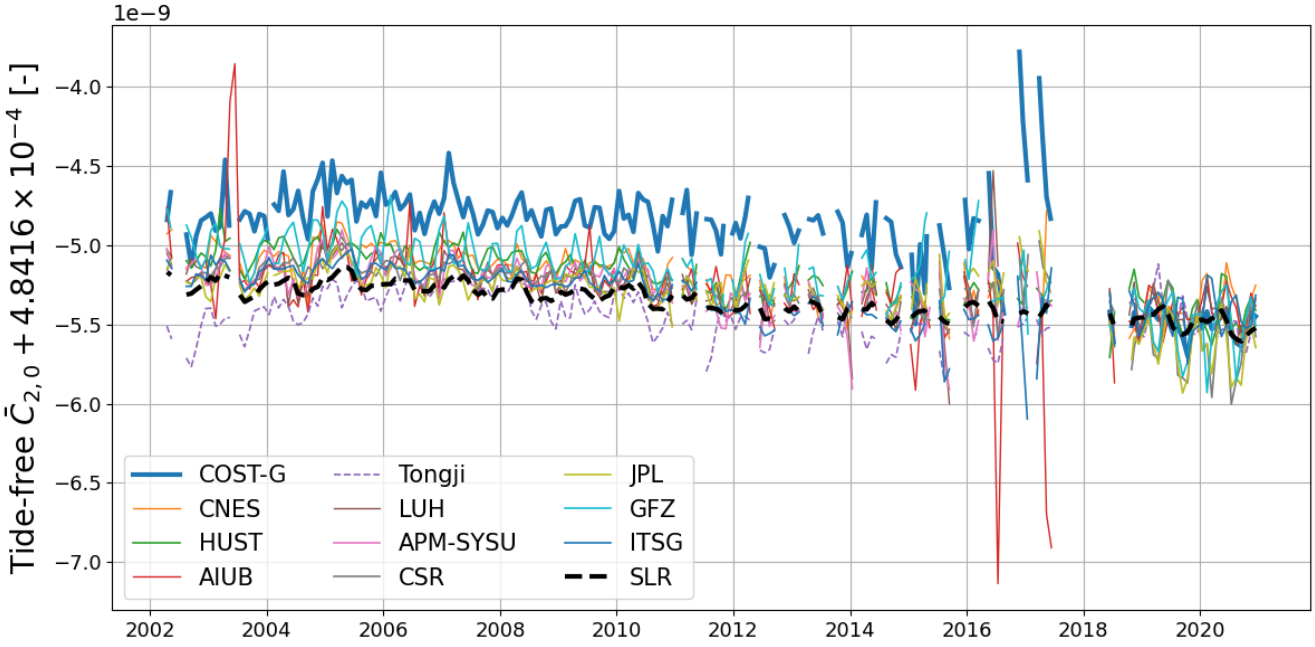


Figure A1. Time series of the tide-free corrected $\bar{C}_{2,0}$ coefficient for all Level-2 gravity field and SLR TN-14.v3 solutions from 2002 to 2020. All solutions have been harmonised following their necessary standards, including consistent reference constants and permanent tide corrections. The symbol $^{(*)}$ next to the product name (see Table A1) indicates products where the stated tide system is inconsistent and was corrected using IERS 2010 Convention.

SLR-replaced product as the primary reference for quantitative analyses. If the SLR-replaced product is not used, we further recommend removing the long-term mean of each time series rather than subtracting a static gravity field, to avoid introducing a fixed bias from any single reference tide system.

A3 Correcting for mean pole tide

The APM-SYSU and Tongji-Grace2022 solutions use the original mean pole model adopted in the IERS Conventions, which combines a cubic model and a linear model for the secular mean pole. The IERS 2010 Conventions (Petit & Luzum, 2010) subsequently adopted a purely linear mean-pole model from 2018 onwards. Consequently, the pole-tide corrections applied to these two solutions are not directly consistent with those of the other GRACE/GRACE-FO solutions considered here. Although the discrepancy between the two mean-pole formulations is small in absolute magnitude, it can become relevant when comparing degree-2 order-1 coefficients between otherwise consistently processed solutions.

To harmonise the degree-2 order-1 coefficients, we compute the difference between the pole-tide corrections obtained with the original and the updated mean-pole models. Specifically, following the solid-Earth and ocean pole-tide formulations given

in Sects. 6.4 and 6.5 of Petit and Luzum (2010), the differences are computed as

$$\delta\Delta\bar{C}_{2,1}^{\mathrm{PT}} = \Delta\bar{C}_{2,1}^{\mathrm{PT,old}} - \Delta\bar{C}_{2,1}^{\mathrm{PT,new}}, \tag{A4}$$

and

$$\delta\Delta\bar{S}_{2,1}^{\mathrm{PT}} = \Delta\bar{S}_{2,1}^{\mathrm{PT,old}} - \Delta\bar{S}_{2,1}^{\mathrm{PT,new}}, \tag{A5}$$

where the superscripts "new" and "old" denote the purely linear and the original cubic/linear mean-pole models, respectively. The resulting time-dependent differences are then added to the corresponding coefficients of APM-SYSU and Tongji-Grace2022,

$$\bar{C}_{2,1}^{\mathrm{harmonised}} = \bar{C}_{2,1}^{\mathrm{original}} + \delta\Delta\bar{C}_{2,1}^{\mathrm{PT}}, \tag{A6}$$

$$\bar{S}_{2,1}^{\mathrm{harmonised}} = \bar{S}_{2,1}^{\mathrm{original}} + \delta\Delta\bar{S}_{2,1}^{\mathrm{PT}}. \tag{A7}$$

Figure A2a and b show the resulting $\bar{C}_{2,1}$ and $\bar{S}_{2,1}$ time series, respectively, for all solutions. The solutions exhibit the same overall temporal variations and trends, with the former convention-dependent discrepancy removed from APM-SYSU and Tongji-Grace2022. A moderate deviation in $\bar{C}_{2,1}$ can be observed in the GFZ RL06 solutions from 2010 onwards, especially visible during the GRACE one-accelerometer phase, consistent with the behaviour previously identified by the authors themselves in Dahle et al. (2019). This deviation is not observed in the corresponding GFZ RL06.3 GRACE-FO solutions.

Appendix B: Gridded EWH residuals distribution

To assess the validity of using the (weighted) standard deviation as an estimator of solution uncertainty, we analyze the distribution of residuals of each gridded solution with respect to the ensemble mean. For each solution, residual values are aggregated over all spatial grid points to form a single empirical distribution, shown in Figure B1. We provide for these distributions in Table B1, three summarising statistics: median, inter-quartile range (IQR), and standard deviation.

Across all solutions, median residuals are of order 10^{-2} cm (Table B1), indicating negligible systematic bias relative to the ensemble mean. The IQR values are comparable among most solutions and closely reflect the distribution widths seen in Figure B1, with ITSG exhibiting the narrowest spread and GFZ and HUST showing slightly broader cores.

APM-SYSU displays a markedly larger standard deviation, despite an IQR comparable to the other solutions. This behaviour is consistent with strong outliers attributed to orbit repeat patterns (see Section 3.3).

Overall, the close correspondence between Figure B1 and the statistics in Table B1 supports the use of the (weighted) standard deviation of residuals as a quantitative measure of the ensemble uncertainty.

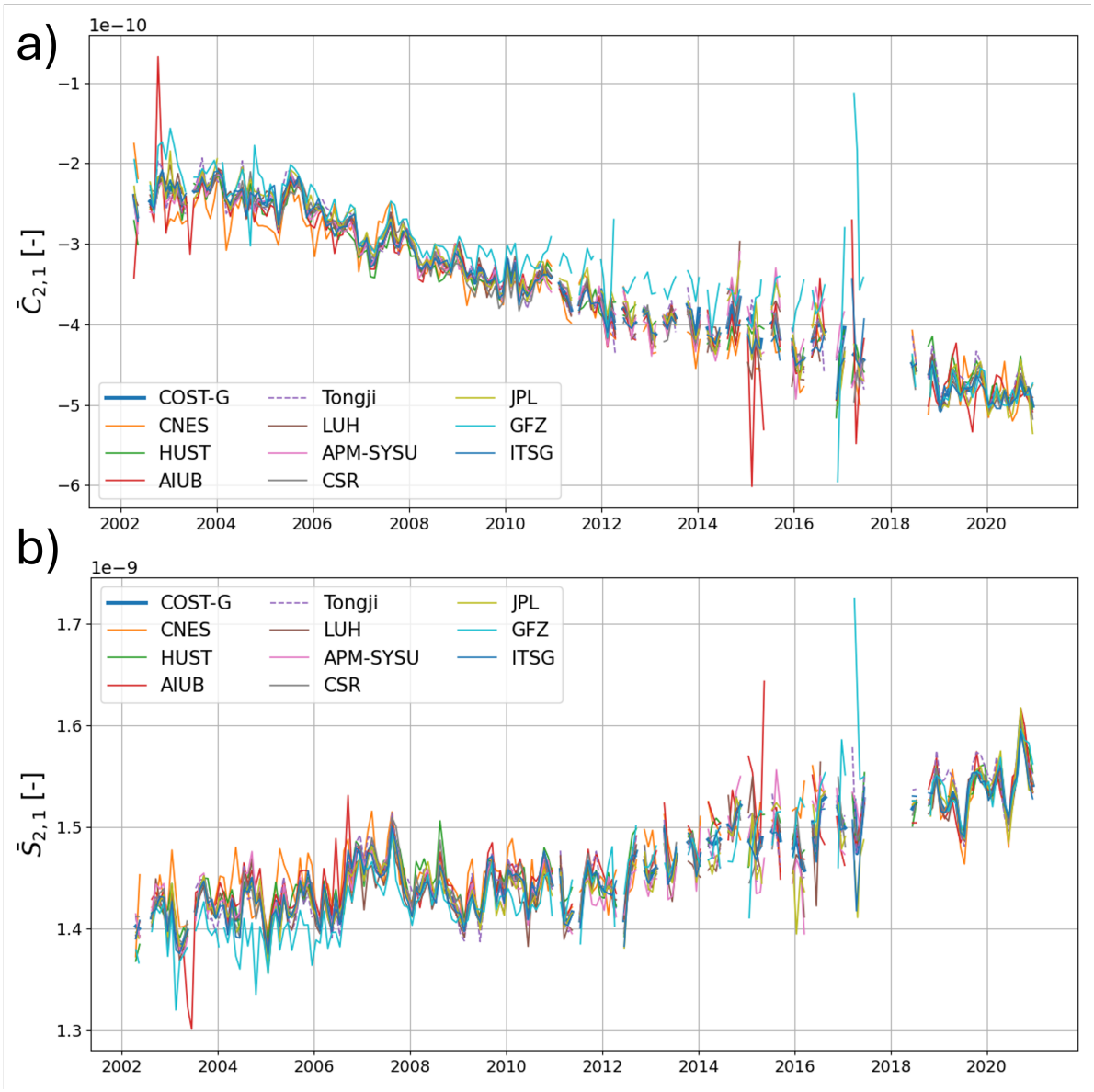


Figure A2. Time series of the harmonised $\bar{C}_{2,1}$ (a) and $\bar{S}_{2,1}$ (b) coefficients for all Level-2 gravity field solutions from 2002 to 2020. APM-SYSU and Tongji-Grace2022 have been corrected from the original cubic/linear mean-pole model to the purely linear mean-pole model adopted from 2018 onwards following the IERS 2010 Conventions. The coefficients shown for all solutions therefore follow a consistent mean-pole convention.

Table B1. Statistical properties (median, inter-quartile range, and standard deviation) of ravelled residual distributions. All values are given in cm (EWH). DDK4 filtering is used and SLR d/o (2,0) and (3, 0) have been replaced.

Solution	Median [cm]	IQR [cm]	Std. dev. [cm]
ITSG	0.013	2.432	2.537
CSR	-0.008	3.066	2.751
JPL	-0.0004	3.127	2.960
HUST	-0.027	3.509	3.157
TONGJI	0.003	3.109	3.120
GFZ	0.011	3.485	3.397
APM-SYSU	0.021	3.174	5.953

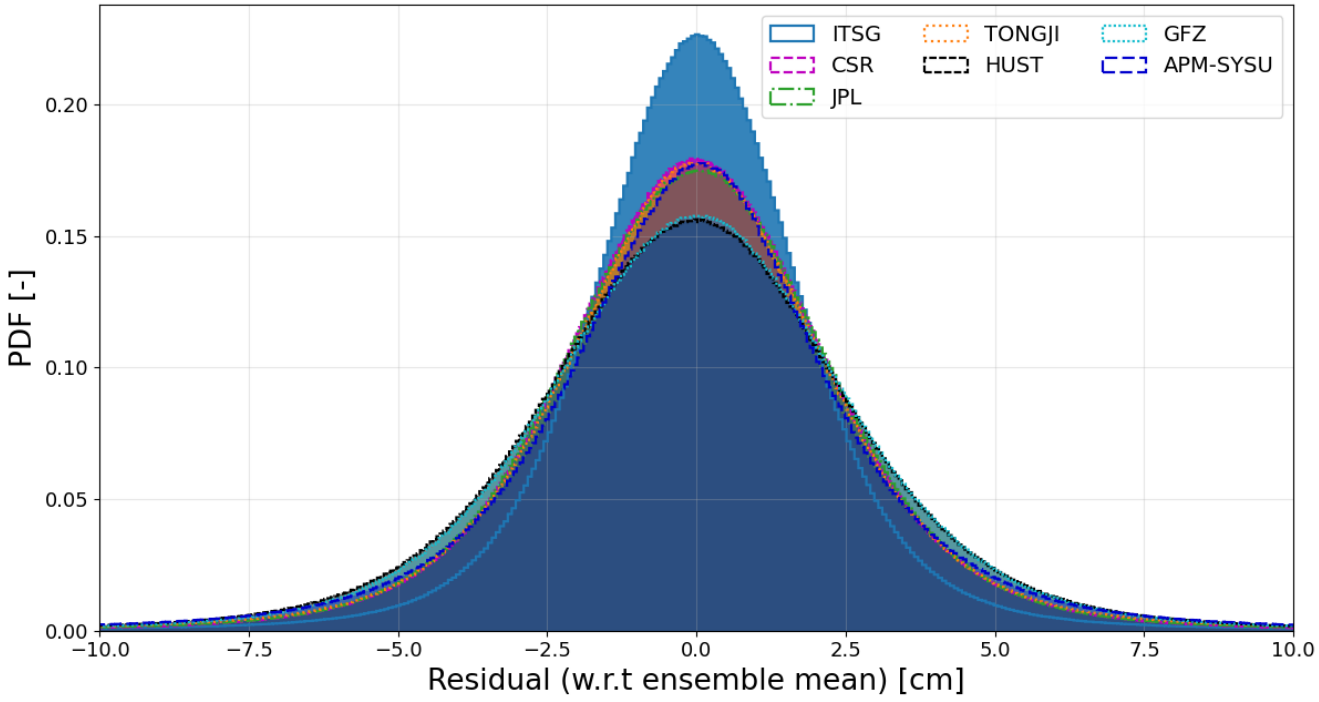


Figure B1. Empirical Probability Density Function (PDF) of EWH residuals (in cm) relative to the ensemble mean for all Level-2 solutions (DDK4 filtered and replaced with SLR d/o (2,0) and (3, 0)).

Appendix C: Aliasing period

We summarise the standard formulation used to compute tidal aliasing periods in the context of GRACE(-FO) observations. The material is included for completeness and to document auxiliary calculations used in this study; it does not introduce any methodological novelty.

The aliasing frequency, f_A, of a tidal constituent with true frequency f is given by

$$f_A = |n_f f_s - f|\,, \tag{C1}$$

where n_f is an integer and f_s denotes the effective GRACE(-FO) sampling frequency. Following Koch et al. (2024), the sampling frequency is defined as

$$f_s = \omega - \dot{\Omega}, \tag{C2}$$

with ω the Earth's sidereal rotation rate, taken as $\omega = 360.9856\ ^\circ\,\mathrm{day}^{-1}$ (IERS 2010 convention), and $\dot{\Omega}$ the nodal precession rate of the satellite orbit.

C1 Nodal precession rate

The nodal precession rate is not strictly constant in time, as it depends on several slowly varying orbital and geophysical parameters. To first order, and assuming a near-circular orbit, it is approximated by

$$\dot{\Omega}(t) \approx -\frac{3}{2}\, J_2(t) \left(\frac{R}{R + h(t)}\right)^2 n(t)\, \cos(i(t))\,, \tag{C3}$$

where J_2 is the Earth's oblateness coefficient, related to the degree-2 zonal Stokes coefficient by $J_2 = -\sqrt{5}\,\bar{C}_{2,0}$. Here, R denotes the mean Earth radius, $h(t)$ the satellite mean altitude, $i(t)$ the orbital inclination, and $n(t)$ the mean motion (the latter three are functions of time).

C2 Time-varying orbital elements

In many GRACE-related studies, $\dot{\Omega}$ is treated as a constant, typically within the range -0.132 to $-0.136\ ^\circ\mathrm{day}^{-1}$ (Koch et al., 2024; Li et al., 2022; W. Liu & Sneeuw, 2021; Ray & Luthcke, 2006). To verify the consistency of this commonly adopted range, we explicitly recomputed $\dot{\Omega}(t)$ by accounting for the temporal variability of $h(t)$, $i(t)$, and $J_2(t)$. Monthly mean values were used for the satellite altitude and inclination, while monthly estimates of J_2 were derived from SLR solutions (Loomis et al., 2020). Although the resulting temporal variations in $\dot{\Omega}$ are small ($\sim 3\%$), they lead to non-negligible differences in aliasing period estimates, ranging from 0.1% up to approximately 5% (e.g. K_1 tide), highlighting the sensitivity of aliasing periods to the assumed nodal precession rate.

The resulting time series of the relevant input parameters are shown in Figure C1. These calculations are included solely to verify the validity of the nodal precession rates commonly assumed in aliasing analyses. The temporal variability of J_2 reflects the well-known SLR-derived $\bar{C}_{2,0}$ variations, which are of order 10^{-10}. Over the mission lifetime, the satellites' mean altitude decreases from approximately 500 km in April 2002 to about 350 km by June 2017, shortly before re-entry. The inclination exhibits only small oscillatory variations, with a peak-to-peak amplitude of approximately 0.18° around an expected mean value of $\sim 89.02^\circ$.

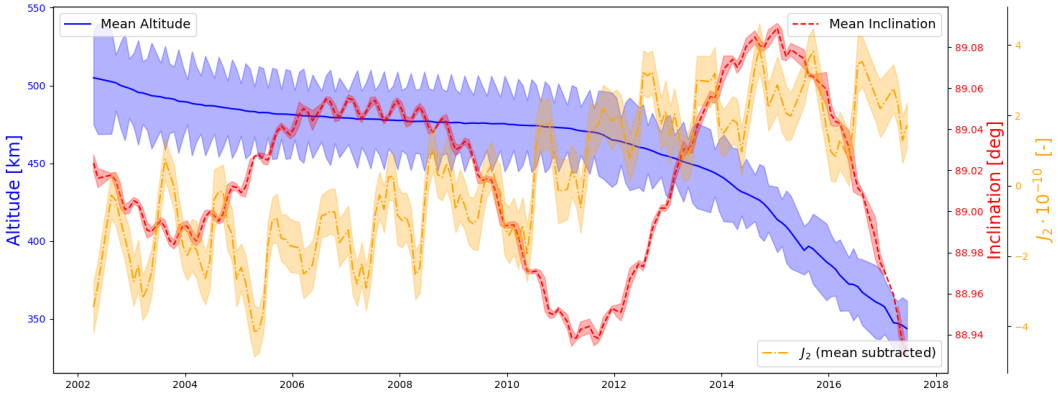


Figure C1. Monthly mean GRACE satellite altitude and inclination from April 2002 to June 2017, together with the corresponding mean-subtracted J_2 estimates derived from SLR (Loomis et al., 2020). Shaded regions indicate the $\pm 1\sigma$ uncertainty bounds: for altitude and inclination, these correspond to the intra-monthly standard deviations, while for J_2 they represent the formal errors of the SLR-derived $\bar{C}_{2,0}$ estimates.

C3 Resulting nodal precession rate variability

Using the time-varying orbital elements and oblateness factors described above, we computed the full time series of the nodal precession rate $\dot{\Omega}(t)$ over the GRACE mission lifetime. The resulting evolution is shown in Figure C2, including $\pm 3\sigma$ uncertainty bounds propagated from the monthly uncertainties in altitude, inclination, and J_2. Note that, unlike the less conservative $\pm 2\sigma$ bounds used throughout the main text, the wider $\pm 3\sigma$ envelope is adopted here to capture even small variations in $\dot{\Omega}(t)$, which, due to the high sensitivity of tidal aliasing periods to the nodal precession rate, can have a disproportionately large influence on the resulting alias frequencies.

The nodal precession rate varies approximately periodically throughout the mission, primarily driven by long-term orbital decay, with secondary contributions from variations in inclination and, to a lesser extent, from changes in J_2. Over the period from April 2002 to June 2017, $\dot{\Omega}$ ranges from approximately $-0.130\,^{\circ}\,\mathrm{day}^{-1}$ in the early mission phase to about $-0.155\,^{\circ}\,\mathrm{day}^{-1}$ toward the end of the mission, as the satellites approached re-entry. The time-averaged nodal precession rate is $-0.134\,^{\circ}\,\mathrm{day}^{-1}$, with a temporal standard deviation of $0.005869\,^{\circ}\,\mathrm{day}^{-1}$.

These results confirm that the commonly adopted constant values of $\dot{\Omega}$ used in GRACE aliasing analyses lie well within the mission-mean range. In light of this consistency, we adopt a representative constant value of $\dot{\Omega} = -0.134\,^{\circ}\mathrm{day}^{-1}$ for the aliasing calculations presented in this study.

C4 Resulting tidal amplitudes

Following the estimation of the nodal precession rate ($\dot{\Omega}$), we analyse the resulting signal amplitudes at the aliasing frequencies. Figure C3 presents the spatial distribution of the resulting low-frequency nuisance and/or geophysical signals at the tidal alias-

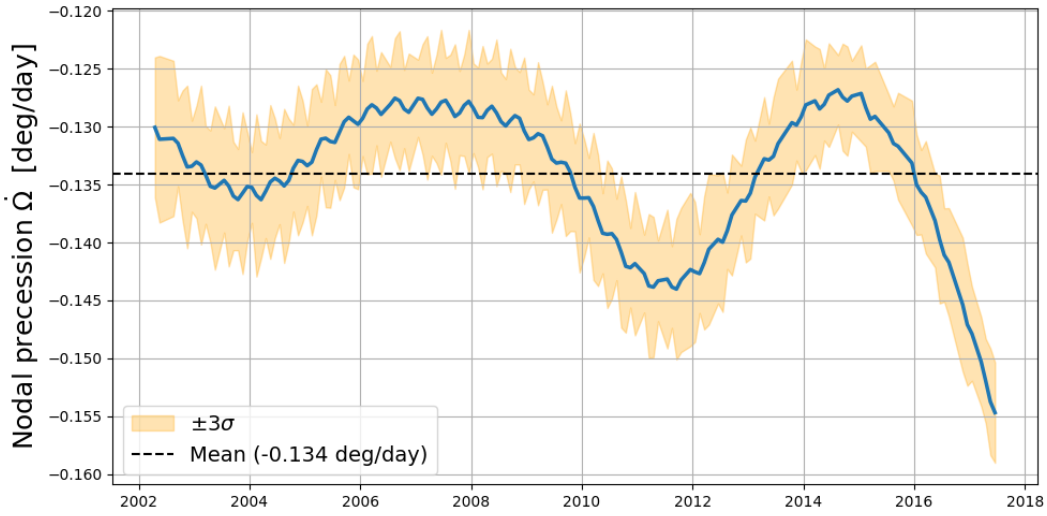


Figure C2. Time series of the GRACE nodal precession rate $\dot{\Omega}$ computed from time-varying altitude, inclination, and J_2, including $\pm 3\sigma$ uncertainty bounds.

ing frequencies, namely the aliased signatures at the frequencies of the main tidal constituents S_2, S_1, P_1, and the unmodelled component R_3 discussed in Section 3.2.

Maximum amplitudes, expressed in cm EWH, reach approximately 2.5 (S_2), 2.0 (P_1), 2.9 (S_1), and 2.0 (R_3) cm. The spatial patterns differ significantly between constituents. The aliased S_2 nuisance signal is predominantly concentrated over oceans and coastal regions, with pronounced amplitudes in the southwest of Greenland, coastal West Antarctica, and semi-enclosed basins such as the Caspian Sea. This matches closely with results obtained from VDK3-filtered COST-G (Dahle et al., 2025). In contrast, the estimated signals at the aliasing periods of S_1 and P_1 exhibit relatively small amplitudes over the oceans but are more strongly expressed over land. Among all estimated grids, S_1 produces the largest land signal, reaching amplitudes of approximately 1.5–3 cm EWH in the Amazon River Basin, consistent with the findings of Li et al. (2022). This exceeds the magnitude of the signal pattern associated with the Zapiola Rise mass anomaly ($\sim$ 1.5-2 cm EWH; (Han et al., 2014; Volkov & Fu, 2008)). Elevated S_1 and P_1 amplitudes are also observed over the Indian subcontinent (India and Bangladesh) and central African river basins. For P_1, the Antarctic signal is primarily confined to West Antarctica, with little expression along the eastern coast.

The estimated amplitude at the aliasing period of the unmodelled R_3 component exhibits a spatial pattern broadly similar to S_1 and P_1, with moderate amplitudes over land and coastal regions. Larger values are observed in West Antarctica, southeastern Greenland, parts of South America (1.0–2 cm), and central Africa, with weaker signatures also present in the Zapiola Rise.

Overall, the aliased S_2 nuisance signal is primarily oceanic and coastal, whereas the aliased S_1 and P_1 signals are characterised by lower-amplitude, land-dominated patterns. All constituents show some degree of relation to the dipolar signal associated with the Zapiola Rise, particularly for S_1, P_1, and R_3. Importantly, these spatial patterns should not be interpreted as

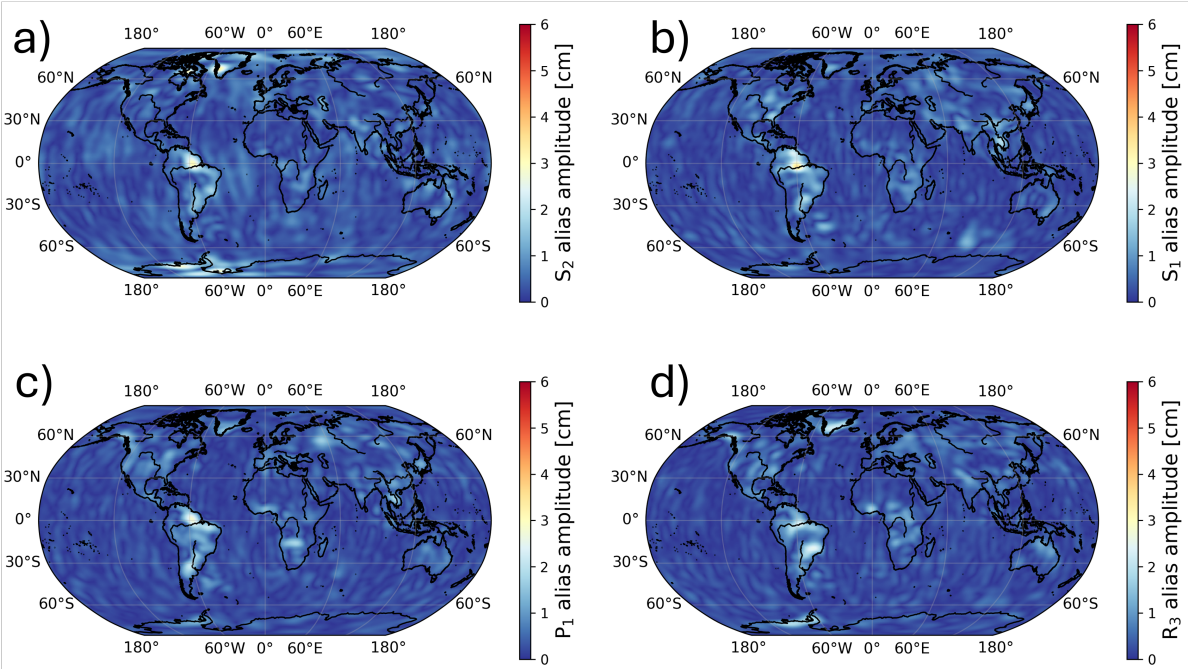


Figure C3. Spatial distribution of tidal aliasing amplitudes derived from a nodal precession rate, $\dot{\Omega} = -0.134\ ^\circ\mathrm{day}^{-1}$, and the DDK3-filtered TUD ensemble mean, for the main constituents: (a) S_2, (b) S_1, (c) P_1, (d) unmodelled R_3. Values are expressed in centimetres equivalent water height (cm EWH).

being entirely caused by residual tidal aliasing. Following the sampling considerations discussed by Han et al. (2010), residual tidal aliasing is more likely to dominate the fitted signals in polar and high-latitude regions, whereas at lower latitudes, particularly in equatorial regions, a larger fraction of the signal may instead reflect genuine geophysical variability. The grids should therefore be interpreted as empirical signals at the respective alias frequencies, and their use as tidal corrections should remain application-dependent.

Appendix D: Overview of datasets and geophysical variable composition

D1 Variable Definitions and Data Product Structure

This appendix summarises the variables, their descriptions, units, and dimensions for each data product type provided within the TUD-L3-EWH-UNC-GRACE data suite. The main product is described in Table D1, the SLR-free ancillary product in Table D2, the climatological products in Tables D3 and D4, and the leakage climatological product in Table D5.

Table D1. Variables included in the TUD-L3-EWH_UNC-GRACEv6.2-DDKi-2002_2020-0.5x0.5 product.

Variable	Long name	Unit	Dimensions
ewh_mean	Ensemble weighted-mean EWH signal	cm	(time, lat, lon)
ewh_mean_corr	GIA-, geocenter-, and tide-corrected EWH signal	cm	(time, lat, lon)
ewh_mean_leakage	Ensemble weighted-mean leakage correction	cm	(time, lat, lon)
ewh_degree1	Degree-1 (geocenter) EWH contribution	cm	(time, lat, lon)
ewh_unc_sols	Ensemble solution uncertainty	cm	(time, lat, lon)
ewh_unc_aod1b	AOD1B uncertainty	cm	(time, lat, lon)
ewh_unc_leakage	Total leakage correction uncertainty	cm	(time, lat, lon)
ewh_unc_degree1	Propagated degree-1 uncertainty	cm	(time, lat, lon)
ewh_unc_degree20	Propagated $\bar{C}_{2,0}$ uncertainty	cm	(time, lat, lon)
ewh_unc_degree30	Propagated $\bar{C}_{3,0}$ uncertainty	cm	(time, lat, lon)
ewh_gia_mean	Ensemble mean GIA trend	cm yr^{-1}	(lat, lon)
ewh_gia_unc	GIA trend uncertainty	cm yr^{-1}	(lat, lon)
weights	Normalised ensemble weights	-	(time, member)

Table D2. Variables included in the TUD-L3-EWH_UNC_noSLR-GRACEv6.2-DDKi-2002_2020-0.5x0.5 product.

Variable	Long name	Unit	Dimensions
ewh_mean	Ensemble weighted-mean EWH signal without SLR replacement	cm	(time, lat, lon)
ewh_unc_sols	Ensemble solution uncertainty without SLR replacement	cm	(time, lat, lon)
weights	Normalised ensemble weights	-	(time, member)

Table D3. Variables included in the TUD-L3-EWH_CLIM-GRACEv6.2-DDKi-2002_2020-0.5x0.5 product.

Variable	Long name	Unit	Dimensions
ewh_mean_bias	Climatological bias	cm	(lat, lon)
ewh_mean_trend	Linear trend	cm yr^{-1}	(lat, lon)
ewh_mean_acc	Climatological acceleration	cm yr^{-2}	(lat, lon)
ewh_mean_annual_cos/sin	Annual harmonic sine/cosine	cm	(lat, lon)
ewh_mean_semiannual_cos/sin	Semiannual harmonic sine/cosine	cm	(lat, lon)
ewh_mean_{tide}_cos/sin	Tidal aliasing harmonics	cm	(lat, lon)
t_clim	Time variable centred at 2008.0	yr	(time)
ewh_mean_clim	Climatological of the EWH signal	cm	(time, lat, lon)
ewh_mean_tides	Tidal aliasing of the EWH signal	cm	(time, lat, lon)
residuals	Post-fit climatological residuals	cm	(time, lat, lon)
ewh_mean_beta	Combined climatological parameters	mixed	(lat, lon, coeff)
ewh_mean_beta_std	Regression parameter standard deviations	mixed	(lat, lon)

Table D4. Variables included in the TUD-L3-EWH_CLIM_CORR-GRACEv6.2-DDKi-2002_2020-0.5x0.5 product.

Variable	Long name	Unit	Dimensions
ewh_mean_corr_bias	Climatological bias of corr. EWH	cm	(lat, lon)
ewh_mean_corr_trend	Linear trend of corr. EWH	cm yr^{-1}	(lat, lon)
ewh_mean_corr_acc	Climatological acceleration of corr. EWH	cm yr^{-2}	(lat, lon)
ewh_mean_corr_annual_cos/sin	Annual harmonic coefficients of corr. EWH	cm	(lat, lon)
ewh_mean_corr_semiannual_cos/sin	Semiannual coefficients of corr. EWH	cm	(lat, lon)
ewh_mean_corr_{tide}_cos/sin	Tidal aliasing coefficients of corr. EWH	cm	(lat, lon)
t_clim	Time variable centred at 2008.0	yr	(time)
ewh_mean_corr_clim	Climatological of corr. EWH signal	cm	(time, lat, lon)
ewh_mean_corr_tides	Tidal aliasing of corr. EWH signal	cm	(time, lat, lon)
residuals	Post-fit climatological residuals	cm	(time, lat, lon)
ewh_mean_corr_beta	Combined climatological parameters	mixed	(lat, lon, coeff)
ewh_mean_corr_beta_std	Regression parameter standard deviations	mixed	(lat, lon, coeff)

Table D5. Variables included in the TUD-L3-EWH_CLIM_LEAKAGE-GRACEv6.2-DDKi-2002_2020-0.5x0.5 product.

Variable	Long name	Unit	Dimensions
ewh_mean_leakage_bias	Leakage fit bias	cm	(lat, lon)
ewh_mean_leakage_trend	Leakage fit trend	cm yr^{-1}	(lat, lon)
ewh_mean_leakage_acc	Leakage fit acceleration	cm yr^{-2}	(lat, lon)
ewh_mean_leakage_annual_cos/sin	Leakage annual harmonics	cm	(lat, lon)
ewh_mean_leakage_semiannual_cos/sin	Leakage semiannual harmonics	cm	(lat, lon)
ewh_mean_leakage_{tide}_cos/sin	Leakage tidal aliasing harmonics	cm	(lat, lon)
t_clim	Time variable centred at 2008.0	yr	(time)
ewh_mean_leakage_clim	Leakage fit reconstruction	cm	(time, lat, lon)
ewh_mean_leakage_tides	Leakage tidal aliasing reconstruction	cm	(time, lat, lon)
residuals	Post-fit leakage climatology residuals	cm	(time, lat, lon)
ewh_mean_leakage_beta	Combined leakage regression parameters	mixed	(lat, lon, coeff)
ewh_mean_leakage_beta_std	Regression parameter standard deviations	mixed	(lat, lon, coeff)

D2 Spherical harmonic signal composition of main variables

Tables D6 and D7 indicate which spherical harmonic components are included in each variable, explicitly distinguishing between degree-1 (geocenter), the low-degree coefficients $\bar{C}_{2,0}$ and $\bar{C}_{3,0}$, and all remaining degrees (2–60).

Table D6. Overview of geophysical components represented in the variables of the TUD-L3-EWH_UNC-GRACEv6.2-DDKi-2002_2020-0.5x0.5 product. Checkmarks indicate that the corresponding contribution is included in the variable. Entries marked "SLR" indicate that the coefficient is replaced by SLR solutions following TN-14.v3. Degree-1 (geocenter) contributions are provided explicitly and are not included by default in other variables. "All other" refers to spherical harmonic degrees 2–60 excluding degree-1, $\bar{C}_{2,0}$, and $\bar{C}_{3,0}$.

Variable	Degree-1	$\bar{C}_{2,0}$	$\bar{C}_{3,0}$	All other
ewh_mean	✗	SLR	SLR	✓
ewh_mean_corr	✓	SLR	SLR	✓
ewh_unc_sols	✗	SLR	SLR	✓
ewh_unc_degree20	✗	✓	✗	✗
ewh_unc_degree30	✗	✗	✓	✗
ewh_unc_aod1b	✗	✓	✓	✓
ewh_degree1	✓	✗	✗	✗
ewh_unc_degree1	✓	✗	✗	✗
ewh_gia_mean	✗	✓	✓	✓
ewh_gia_unc	✗	✓	✓	✓
ewh_mean_leakage	✗	SLR	SLR	✓
ewh_unc_leakage	✗	SLR	SLR	✓

Table D7. Overview of geophysical components represented in the variables of the TUD-L3-EWH_UNC-GRACEnoSLR ancillary product. In this product, low-degree coefficients $\bar{C}_{2,0}$ and $\bar{C}_{3,0}$ are *not* replaced by SLR solutions. Degree-1 (geocenter) contributions are not included. "All other" refers to spherical harmonic degrees 2–60 excluding degree-1, $\bar{C}_{2,0}$ and $\bar{C}_{3,0}$.

Variable	Degree-1	$\bar{C}_{2,0}$	$\bar{C}_{3,0}$	All other
ewh_mean	✗	✓	✓	✓
ewh_unc_sols	✗	✓	✓	✓

Appendix E: Additional uncertainty statistics

E1 Uncertainties in hydrological regions

This appendix provides basin-averaged temporal statistics of uncertainty components affecting GRACE(-FO) EWH time series over major hydrological basins. All statistics are reported as 2σ values and are derived from DDK3-filtered Level-2 solutions (degree and order 2–60).

E1.1 Level-3 uncertainty components

Table E1 summarises the dominant Level-3 uncertainty components for the Amazon, Mississippi–Missouri, and Ganges–Brahmaputra basins. Across all three basins, AOD1B-related uncertainty is approximately 0.7–0.8 cm EWH, with standard

deviations below 0.10 cm, indicating that residual atmosphere–ocean de-aliasing errors are a minor contribution at the basin scale when expressed in terms of the direct gravity field signal. However, it should be noted that AOD1B model errors can excite orbital resonances, which manifest in the low–low satellite-to-satellite tracking (ll-SST) residuals and may contribute to correlated errors (e.g., striping) in the recovered fields. This effect is not directly reflected in the basin-averaged EWH statistics presented here. The ensemble uncertainty is consistently larger, with mean values of about 3.1–3.6 cm and standard deviations of roughly 1.7–2.4 cm, reflecting differences among Level-2 processing strategies and background models.

Uncertainties associated with low-degree coefficients, including degree-1 (geocentre motion), SLR-derived $\bar{C}_{2,0}$ and $\bar{C}_{3,0}$, and their combined contribution, are smaller by one order of magnitude (i.e. from 0.6 to 0.7 cm) compared to ensemble uncertainty and similar in magnitude to the AOD1B uncertainty, but remain non-zero and are therefore retained for completeness. The very large maximum values occasionally observed for the ensemble uncertainty are primarily associated with unfavourable orbit repeat patterns and sampling geometry, rather than representative basin-scale variability.

Table E1. Basin-averaged 2σ uncertainty statistics for major river basins derived from Level-2 GRACE(-FO) solutions (DDK3 filtered, degree/order 2–60). Shown are descriptive statistics of the solution ensemble uncertainty, AOD1B de-aliasing uncertainty, degree-1 (geocentre) uncertainty, SLR-derived low-degree coefficient uncertainties, and their combined uncertainty. All values are given in centimetres equivalent water height.

Basin	Uncertainty source	Mean	Median	Std. dev.	Min	Max
Amazon	Ensemble uncertainty	3.62	3.17	1.74	1.99	13.96
	AOD1B uncertainty	0.83	0.83	0.08	0.62	1.12
	Degree-1 uncertainty	0.58	0.58	0.00	0.58	0.58
	SLR $\bar{C}_{2,0}$ uncertainty	0.28	0.27	0.03	0.22	0.35
	SLR $\bar{C}_{3,0}$ uncertainty	0.11	0.00	0.14	0.00	0.38
	Combined SLR + degree-1	0.66	0.65	0.03	0.62	0.76
Mississippi–Missouri	Ensemble uncertainty	3.13	2.66	1.79	1.57	18.01
	AOD1B uncertainty	0.71	0.71	0.07	0.54	0.86
	Degree-1 uncertainty	0.56	0.56	0.00	0.56	0.56
	SLR $\bar{C}_{2,0}$ uncertainty	0.10	0.10	0.01	0.08	0.13
	SLR $\bar{C}_{3,0}$ uncertainty	0.17	0.00	0.21	0.00	0.57
	Combined SLR + degree-1	0.62	0.57	0.07	0.57	0.81
Ganges–Brahmaputra	Ensemble uncertainty	3.38	2.77	2.43	1.67	27.43
	AOD1B uncertainty	0.71	0.70	0.10	0.50	1.01
	Degree-1 uncertainty	0.58	0.58	0.00	0.58	0.58
	SLR $\bar{C}_{2,0}$ uncertainty	0.12	0.12	0.01	0.10	0.15
	SLR $\bar{C}_{3,0}$ uncertainty	0.24	0.00	0.30	0.00	0.83
	Combined SLR + degree-1	0.69	0.59	0.14	0.58	1.02

E1.2 Leakage correction uncertainty

For completeness, Table E2 reports basin-averaged statistics of the leakage correction uncertainty. Leakage is shown separately from the Level-3 uncertainty components, as it arises from post-processing choices related to spatial filtering and is treated independently in the main analysis. All values represent 2σ temporal statistics of basin-averaged leakage uncertainty.

The leakage uncertainties reported here are one to two orders of magnitude larger than the filtered signal uncertainty components discussed in Section E1.1, reflecting the dominant role of spatial filtering in the overall error budget. The extremely large maximum values are attributed to resonance orbit periods, during which the GRACE ground-track sampling degrades significantly, amplifying leakage errors.

Table E2. Basin-averaged 2σ statistics of leakage correction uncertainty for major river basins (DDK3 filtered, degree/order 1–60). Values are given in centimetres equivalent water height (cm EWH).

Basin	Mean	Median	Std. dev.	Min	Max
Amazon	22.72	19.10	12.13	11.78	109.09
Mississippi–Missouri	19.23	16.22	14.66	9.98	190.36
Ganges–Brahmaputra	22.44	17.62	18.49	10.62	214.69

E2 Uncertainties in glaciological regions

This appendix summarises basin-averaged temporal statistics of uncertainty components affecting GRACE(-FO) EWH time series over Greenland and Antarctica. All statistics are reported as 2σ values and are derived from DDK3-filtered Level-2 solutions (degree and order 2–60). The purpose of this section is to provide additional quantitative context to the uncertainty magnitudes discussed in the main text.

E2.1 Level-3 uncertainty components

Table E3 summarises the dominant Level-3 uncertainty components. The ensemble uncertainty represents the largest contribution for both basins, with mean values of 3.22 cm (Greenland) and 3.04 cm (Antarctica) at the 2σ level. The variability of this component is also comparatively large, reflected in standard deviations of 1.35 cm and 1.72 cm and maximum values reaching 13.36 cm and 17.81 cm for Greenland and Antarctica, respectively.

AOD1B-related uncertainty forms the second largest contribution and is the most important systematic component after the ensemble spread. Mean 2σ values amount to 1.46 cm for Greenland and 2.26 cm for Antarctica. Relative to the ensemble uncertainty, this corresponds to roughly 50% of the ensemble contribution for Greenland and about 77% for Antarctica. The larger influence over Antarctica reflects the stronger sensitivity of this basin-scale signal to atmospheric and oceanic mass variability represented by the AOD1B de-aliasing model. The temporal variability of this component is moderate, with standard deviations of 0.30 cm and 0.51 cm and maxima of 2.22 cm and 3.86 cm for Greenland and Antarctica, respectively.

Uncertainties associated with low-degree coefficients are substantially smaller. The degree-1 (geocentre) contribution is constant in time at approximately 0.5 cm for both basins. SLR-derived low-degree coefficients contribute mean uncertainties of about 0.52–0.56 cm for $\bar{C}_{2,0}$ and 0.44–0.48 cm for $\bar{C}_{3,0}$, although the latter exhibits strong skewness with medians close to zero and occasional maxima exceeding 1.4–1.6 cm. When combined with the degree-1 contribution, the resulting mean uncertainty amounts to approximately 0.98 cm for Greenland and 1.04 cm for Antarctica.

Overall, the uncertainty budget is therefore dominated by the ensemble spread and AOD1B de-aliasing errors, which together exceed the combined contribution of low-degree coefficient uncertainties by a factor of roughly two to three on average. The low-degree terms nevertheless contribute a persistent background uncertainty of order $\sim$1 cm (2σ) and are retained in the total uncertainty estimate.

Table E3. Basin-averaged 2σ uncertainty statistics for Greenland and Antarctica derived from Level-2 GRACE(-FO) solutions (DDK3 filtered, degree/order 1–60). Shown are descriptive statistics of ensemble uncertainty, AOD1B de-aliasing uncertainty, degree-1 (geocentre), SLR-derived low-degree coefficients, and their combined uncertainty. All values are given in centimetres equivalent water height (cm EWH).

Region	Uncertainty source	Mean	Median	Std. dev.	Min	Max
Greenland	Ensemble uncertainty	3.22	2.93	1.35	1.78	13.36
	AOD1B uncertainty	1.46	1.42	0.30	0.94	2.22
	Degree-1 uncertainty	0.53	0.53	0.00	0.53	0.53
	SLR $\bar{C}_{2,0}$ uncertainty	0.51	0.51	0.05	0.41	0.64
	SLR $\bar{C}_{3,0}$ uncertainty	0.41	0.00	0.52	0.00	1.42
	Combined SLR + degree-1	0.95	0.77	0.28	0.67	1.63
Antarctica	Ensemble uncertainty	3.04	2.58	1.72	1.88	17.81
	AOD1B uncertainty	2.26	2.20	0.51	1.36	3.86
	Degree-1 uncertainty	0.53	0.53	0.00	0.53	0.53
	SLR $\bar{C}_{2,0}$ uncertainty	0.54	0.53	0.05	0.44	0.68
	SLR $\bar{C}_{3,0}$ uncertainty	0.46	0.00	0.57	0.00	1.56
	Combined SLR + degree-1	1.00	0.79	0.32	0.68	1.76

E2.2 Leakage uncertainty

For completeness, Table E4 reports basin-averaged statistics of the leakage correction uncertainty. Leakage is shown separately from the Level-3 uncertainty components, as it arises from post-processing choices related to spatial filtering and is treated independently in the main analysis. All values represent 2σ temporal statistics of basin-averaged leakage uncertainty.

The leakage uncertainties reported here are substantially larger than the filtered Level-3 uncertainty components discussed in Section E2.1. Mean values reach approximately 25 cm EWH for Greenland and 20 cm EWH for Antarctica, with temporal standard deviations of about 9.3 cm and 9.9 cm, respectively. These values reflect the strong influence of spatial filtering and signal attenuation near coastlines and ice–ocean boundaries, which enhance leakage effects when basin averages are

computed. The extremely large maximum values are attributed to resonance orbit periods, during which the GRACE ground-track sampling degrades significantly and filtering-induced leakage errors become temporarily amplified.

Table E4. Basin-averaged 2σ statistics of leakage correction uncertainty for Greenland and Antarctica (DDK3 filtered, degree/order 1–60). Values are given in centimetres equivalent water height (cm EWH).

Region	Mean	Median	Std. dev.	Min	Max
Greenland	25.34	22.74	9.34	13.78	99.16
Antarctica	19.86	17.14	9.93	12.72	101.87